

Computing the complex

**Dusty plasmas in the presence of magnetic fields
and UV radiation**

Victor Land

Computing the complex
Dusty plasmas in the presence of magnetic fields and UV radiation

© Copyright 2007 by Victor Land

Proefschrift – ISBN 978-90-393-4695-2

Printed by PrintPartners Ipskamp

Subject headings: dusty plasma, magnetic field, UV radiation, simulation

Cover figure: Greyscale picture of spiral galaxy NGC 3370, taken by the Hubble Space Telescope. Numerous, more distant galaxies are visible in the background. It serves to illustrate the abundance of plasma and dust in the universe.

Credits: NASA, The Hubble Heritage Team, and A. Riess (STScI)

The work described in this thesis was carried out at the ‘FOM-Instituut voor Plasmafysica Rijnhuizen’ in Nieuwegein, the Netherlands, and at the Plasma Sciences Laboratory of Auburn University, in Auburn, the United States of America.

Computing the complex

Dusty plasmas in the presence of magnetic fields and UV radiation

Berekenen van het complex(e)
Stoffige plasma's in de aanwezigheid van magnetische velden en
ultraviolette straling

(met een samenvatting in het Nederlands)

PROEFSCHRIFT

ter verkrijging van de graad van doctor aan de Universiteit Utrecht, op
gezag van de rector magnificus, prof. dr. J.C. Stoof, ingevolge het
besluit van het college voor promoties in het openbaar te verdedigen op
dinsdag 11 december 2007 des ochtends te 10.30 uur

door

Victor Land

geboren op 25 december 1979, te Zijpe

Promotoren: Prof. Dr. W. J. Goedheer
Prof. Dr. N. J. Lopes Cardozo

The work described in this thesis was performed as part of the research programme of the ‘Stichting voor Fundamenteel Onderzoek der Materie’ (FOM) with financial support of the ‘Nederlandse Organisatie voor Wetenschappelijk Onderzoek’ (NWO), and Euratom, and with financial support from the CPS research school.

*Not only is the universe stranger than we imagine,
it is stranger than we can imagine.*

Sir Arthur Stanley Eddington, 1882-1944

*I believe that a scientist looking at nonscientific problems
is just as dumb as the next guy.*

Richard Phillips Feynman, 1918-1988

List of natural constants, used symbols and acronyms

Symbol	Name	Value	[]
Natural constants			
ϵ_0	Permittivity of vacuum	$8.85419 \cdot 10^{-12}$	F m ⁻¹
κ_T	Thermal conductivity coefficient	$1.772 \cdot 10^{-2}$ (Ar)	W K ⁻¹ m ⁻¹
c	Speed of light in vacuum	299 792 458	m s ⁻¹
e	Natural number	2.71828	–
e	Electron charge	$1.60219 \cdot 10^{-19}$	C
h	Planck constant	$6.62618 \cdot 10^{-34}$	J s
k_B	Boltzmann constant	$1.38066 \cdot 10^{-23}$	J K ⁻¹
m_e	Electron mass	$9.10953 \cdot 10^{-31}$	kg
m_p	Proton mass	$1.67265 \cdot 10^{-27}$	kg
m_+	Argon-18 ion mass	$6.633645 \cdot 10^{-26}$	kg
Fields and potentials			
B	Magnetic induction	–	T
E	Electric field	$-\nabla\phi(r)$	V m ⁻¹
$\bar{\mathbf{E}}$	Time averaged electric field	–	V m ⁻¹
\mathbf{E}_{eff}	Effective electric field	–	V m ⁻¹
$E_{k+\frac{1}{2}}$	Electric field at midpoint (PIC)	$\frac{V_k - V_{k+1}}{\Delta z}$	V m ⁻¹
F	General force	–	N
F_E	Electrostatic force	–	N
F_g	Force of gravity	–	N
F_{ion}	Ion drag force	–	N
F_{nd}	Neutral drag force	–	N
F_{th}	Thermophoretic force	–	N
g	Gravitational acceleration	$-9.81 \hat{z}$	m s ⁻²
L	Angular momentum	$m\mathbf{r} \times \mathbf{v}$	kg m ² s ⁻¹
$\phi(r)$	Potential	–	V
ϕ_D	Dust particle surface potential	$Q_D/4\pi\epsilon_0 R$	V
Ψ	Effective potential	$e\phi(r)/T_e$ (eV)	–
Ψ_D	Effective dust particle potential	$e\phi_D/T_e$ (eV)	–
V_a	Anode potential	–	V
V_c	Cathode potential	–	V
V_f	Measured floating potential	–	V
V_k	Potential on grid point k (PIC)	–	V
V_p	Measured plasma potential	–	V

Symbol	Name	Value	[]
--------	------	-------	-----

Length scales and cross sections

Δ	Average inter-particle distance	$n^{-1/3}$	m
λ_D	Linearized Debye length	$(1/\lambda_e^2 + 1/\lambda_+^2)^{-1/2}$	m
λ_e	Electron Debye length	$(\epsilon_0 k_B T_e / e^2 n_e)^{1/2}$	m
λ_+	Ion Debye length	$(\epsilon_0 k_B T_+ / e^2 n_+)^{1/2}$	m
ρ_0	Coulomb radius	$R(e\phi_D / 2E_s)$	m
σ	General collision cross section	–	m ²
σ_{abs}	Light absorption cross section	–	m ²
σ_c	OML collection cross section	πb_c^2	m ²
σ_{ext}	Light extinction cross section	–	m ²
σ_s	Ion momentum scattering cross section	$4\pi\rho_0^2\Lambda$	m ²
σ_{sca}	Light scattering cross section	–	m ²
A_S	Sheath surface area	–	m ²
L_{NN}	Distance between nearest neighbors	–	m
R	Dust particle radius	–	m
b_c	OML collection radius	$R(1 - e\phi_D / E_s)^{1/2}$	m
h	Impact parameter	–	m
l_{mfp}	Mean free path	$(n\sigma)^{-1}$	m
r_c	Cyclotron radius	v_{\perp} / ω_c	m

Time scales, rates, frequencies, currents

Γ_j	Flux of particle species j	–	m ⁻² s ⁻¹
Γ_{w_e}	Flux of electron energy density	–	J m ⁻² s ⁻¹
ν	General collision frequency	–	s ⁻¹
ν_{RF}	RF frequency	$13.56 \cdot 10^6$	s ⁻¹
ν_+	Ion momentum transfer frequency	$e / m_+ \mu_+$	s ⁻¹
$\langle \sigma v \rangle$	Ionization rate	–	m ³ s ⁻¹
τ_{ch}	Charging time	$\frac{\epsilon_0 (2m_+ E_s)^{1/2}}{e^2 R n_+}$	s
τ_{it}	Ion transit time	$(eV_c / k_B T_e)^{3/4} \omega_{p,+}^{-1}$	s
$\tau_{p,D}$	Dust acoustic wave period	$2\pi / \omega_{p,D}$	s
τ_{RF}	RF period	$1 / \nu_{RF}$	s
$\omega_{c,j}$	Cyclotron frequency for species j	$q_j \mathbf{B} / m_j$	rad s ⁻¹
$\omega_{p,j}$	Plasma frequency for species j	$(n_j Z_j e^2 / m_j \epsilon_0)^{1/2}$	rad s ⁻¹
\mathcal{F}	Flux	–	m ⁻² s ⁻¹
\mathcal{I}	Intensity of light source	–	W m ⁻²
I_j, J_j	Current (density) of species j	–	C s ⁻¹ (m ⁻²)
I_{is}, J_{is}	Ion saturation current (density)	–	C s ⁻¹ (m ⁻²)
S_j, S_{w_e}	Sinks or source term for particles/energy	–	(J) m ³ s ⁻¹
k_{rec}	Volume recombination rate	–	m ³ s ⁻¹

Symbol	Name	Value	[]
Dusty plasma parameters			
Γ	Coupling parameter	$\frac{Q_D^2 \exp(-\Delta/\lambda_D)}{4\pi\epsilon_0\Delta k_B T_D}$	–
Λ	Coulomb logarithm	$\ln\left(\frac{1+\beta}{\beta+R/\lambda_D}\right)$	–
α	Mass ratio	m_+/m_e	–
β	Non-linearity parameter	ρ_0/λ_D	–
μ_j	Mobility for charged species j	$Z_j e/m_j \nu_{m,j}$	$\text{m}^2 (\text{Vs})^{-1}$
ρ	Charge density	$\Sigma_j (n_j Z_j e)$	C m^{-3}
σ_p	Particle surface charge density	$Q_D/4\pi R^2$	C m^{-2}
\mathcal{K}	Collisional operator in ion drag	–	–
\mathcal{P}	Havnes parameter	$n_D Z_D/n_e$	–
D_a	Ambipolar diffusion coefficient	$\frac{\mu_+ D_e + \mu_e D_+}{\mu_e + \mu_+}$	$\text{m}^2 \text{s}^{-1}$
D_j	Diffusion coefficient for species j	$\mu_j k_B T_j / Z_j e$	$\text{m}^2 \text{s}^{-1}$
H_j	Hall parameter for species j	$\omega_{c,j} / 2\pi \nu_{m,j}$	–
N_j	Particle number of species j	$n_j \times \text{Volume}$	–
N_{NN}	Number of nearest neighbors	–	–
P_j	Partial pressure of species j	$n_j k_B T_j$	Pa
Q_D	Dust charge	$Z_D e$	C
T_j	Temperature of species j	–	K
Z_j	Charge number for species j	–	–
n_j	Number density of species j	–	m^{-3}
x_j	Fractional ionization of species j	$n_j / (n_N + n_j)$	–
z	Energy ratio	$k_B T_e / E_s$	–
Particle velocities and energies			
ϵ	Average electron temperature	$3k_B T_e / 2$	J
E_F	Fermi energy in electron gas	$\frac{\hbar^2}{2m} (3\pi^2 n)^{2/3}$	J
E_s	Mean ion energy	$E_+ + E_T = m_+ v_+^2 / 2$	J
E_T	Thermal ion energy	$m_+ v_T^2 / 2$	J
E_{UV}	UV photon energy	$E_{UV} = h\nu_{UV} = hc/\lambda_{UV}$	J
E_+	Kinetic ion energy	$m u_+^2 / 2$	J
M_T	Thermal ion Mach number	u_+ / v_T	–
\mathbf{u}_+	Ion drift velocity	$\mu_+ \mathbf{E}_{eff}$	m s^{-1}
u_B	Bohm velocity	$(k_B T_e / m_+)^{1/2}$	m s^{-1}
\mathbf{v}_{dr}	General drift velocity	$\mathbf{F} \times \mathbf{B} / q_j B^2$	m s^{-1}
\mathbf{v}_E	$\mathbf{E} \times \mathbf{B}$ drift velocity	$\mathbf{E} \times \mathbf{B} / B^2$	m s^{-1}
\mathbf{v}_P	Pressure gradient drift velocity	$\nabla P \times \mathbf{B} / en B^2$	m s^{-1}
v_{ph}	Phase velocity of dust acoustic wave	$(k_B T_+ n_D Z_D^2 / m_D n_+)^{1/2}$	m s^{-1}
v_+	Mean ion velocity	–	m s^{-1}

Short**Full**

Acronyms

AC	Alternating Current
CCD	Charge-Coupled Device
DC	Direct Current
DPX	Dusty Plasma eXperiment
ITER	the International Thermonuclear Experimental Reactor
Nd-YAG	Neodymium doped Yttrium Aluminium Garnet
OML	Orbital Motion Limited theory
Op-Amp	Operational Amplifier
PIC/MC	Particle-In-Cell plus Monte Carlo
PIV	Particle Image Velocimetry
PKE	Plasma Kristall Experiment
RF	Radio Frequency
YSO	Young Stellar Object

Acknowledgments

Even though 'scientists' are believed to be solitary, pale people, with funny hair, working in barely lit rooms¹, the fact is, that this work could never have been finished without the help and guidance of many people, who I want to thank from the bottom of my heart.

I'd like to thank my supervisor, Wim Goedheer, for his patience and wisdom. During four years, you kept on explaining me physics, never giving up. It must be like driving your car against a brick wall a thousand times, and then getting out of the car, smiling (and hopefully on the other side of the wall). Thank you for the freedom I was given during this process.

I also thank Niek Lopes Cardozo for his help in presenting my results, so that they were understandable . . . and also understandable to a much broader audience than just the science specialist. You were inspiring.

I owe Rony Keppens, Gerrit Kroesen, Henrik Rudolph and Edward Thomas, Jr. my gratitude for reading my manuscript and for their many useful comments, which greatly improved this thesis.

I'm thankful also for the help Edward gave me in Auburn, in the United States of America. I've learnt a great deal about America, myself, and science. I also thank Jeremiah, John, Ashley and all the other people I've met. I thank Bill Amatucci for introducing me to them in the first place, and for not having me killed at the gates of his lab.

I thank the many people in the 'dusty plasma community'.

Many 'Rijnhuizenaren' contributed to these four great years. Hugo is thanked for sharing his knowledge and his bluff. I really appreciated the discussions about life in general with Gerard. Amy, Dagmar, Dick, Emiel, Erik, Jan-Willem, Jeroen, Rob, Wouter and Zakaria are thanked for their enthusiasm. I also thank the 'voetballers', for keeping me physically fit and mentally relaxed (and vice versa). There are many more important people. I can not name you all here, but I thank you!

My family (mams, Ief) and 'almost-family' is of enormous importance. Thank you for giving me a time and place just to be me, even though I must often have been very absent-minded.

I thank my friends for the things we did and the many beers, wines, discussion and laughter we shared. Jetse, Ruben, Jasper, Peter, Wytske, everybody, I hope we keep it up in the future.

Then, there is just you, Anne, to thank. I thank you for being my light, my love, my life.

Victor Land, September 2007

¹For the fact that the latter is not so, I wholeheartedly thank Frits Hekkenberg.

Contents

1	Introduction	1
1.1	Plasma	1
1.2	Dusty plasma	4
1.3	Previous work, Contribution of this thesis	7
1.4	Outline thesis	8
1.5	Publications related to this thesis	9
2	Theory of dusty plasma	15
2.1	Creating a plasma	15
2.1.1	DC discharge	17
2.1.2	Capacitively coupled RF discharge	18
2.2	Properties of dusty plasma	20
2.2.1	Quasi-neutrality	20
2.2.2	Quasi-neutrality with dust	22
2.2.3	Screening	22
2.2.4	Particle charging	25
2.3	Forces acting on dust particles	33
2.3.1	Electrostatic force	33
2.3.2	Gravity	34
2.3.3	Ion drag force	34
2.3.4	Neutral drag force	38
2.3.5	Thermophoretic force	39
2.3.6	Mutual Coulomb interaction	40
2.3.7	Summary	41
2.3.8	Void formation	41
2.4	Simulation models	41
2.4.1	Fluid model	41
2.4.2	Particle-in-Cell plus Monte Carlo	44

3	Modelling of dust transport in dusty plasma in the presence of a magnetic field	51
3.1	Motivation	53
3.2	The experiment and the model	54
3.3	Dusty plasmas without magnetic field, and with $B=0.25$ Tesla . . .	55
3.4	Dust transport with an applied magnetic field	59
3.5	Ion transport and ambipolar diffusion	63
3.5.1	Effect of magnetic field on charging	66
3.6	Comparison with planet formation region	67
3.7	Conclusions	69
4	Experiments on dusty DC discharge with applied magnetic field	73
4.1	Motivation	75
4.2	Device	77
4.3	Diagnostics	80
4.3.1	Langmuir probe	81
4.3.2	Emissive probe	83
4.3.3	Camera and PIV system	85
4.4	Plasma and particle response	86
4.4.1	Setup 1 – Plasma response	86
4.4.2	Setup 1 – Particle response	87
4.4.3	Setup 2 – Plasma and particle response	88
4.5	Measurements on dust cloud at equilibrium position	90
4.6	Conclusions	92
5	Large-angle scattering, ion flow speed, ion-neutral collisions and the ion drag force	95
5.1	Motivation	97
5.2	Results for different models	98
5.2.1	Small angle scattering and large angle scattering	98
5.2.2	Ion flow speed	101
5.2.3	Collisions	104
5.3	Comparison with experiments	106
5.3.1	Particles falling through RF discharge	106
5.3.2	Void formation around probe	109
5.4	Conclusions	111
6	The plasma inside a dust free void: Hotter, denser, or both?	115
6.1	Motivation	117
6.2	Plasma response to dust: Global model	118
6.3	Modelled geometry	120

6.4	Results	121
6.5	Comparison with Particle-In-Cell/Monte Carlo calculations	128
6.6	Conclusions	130
7	Manipulating dust charge using UV light in a complex plasma	133
7.1	Motivation	135
7.2	Photo-detachment in the model	135
7.3	Results	137
	7.3.1 Low dust density results	138
	7.3.2 High dust density results	140
7.4	Response to a short pulse of UV light	142
	7.4.1 Dust charge response	142
	7.4.2 Plasma response	143
	7.4.3 Time scales and plasma shut-down	147
7.5	Conclusions	149
	Summary	153
	Samenvatting	156
	Curriculum Vitæ	159

1. Introduction

1.1 Plasma

On Earth, we are most often confronted with solids, fluids and gases. As an example, at atmospheric pressure and at room temperature, water is in what is called the liquid state. Cooling it below the freezing point turns it into a solid, while it turns into a gas when heated above the boiling point. It is clear that the temperature of the water (or the amount of energy that is put into it) determines the state it is in.

Heating the water increases the average amount of kinetic energy per molecule. Therefore, the molecules move faster and faster. When the gas is hot enough, collisions between molecules make them fall apart into separate atoms, or groups of atoms. Heating the gas even more results in collisions between atoms in which electrons, bound to the core of the atom, gain so much energy that they overcome this bond and escape, leaving a positively charged ion behind. This results in a mixture of negatively charged electrons, the positively charged ions, and of course neutral atoms which have not yet experienced such a violent collision.

We call this soup of particles *plasma*, which is sometimes referred to as the fourth state of matter (after the three aforementioned states), even though there is no sudden transition from the gas into the plasma state. It now also becomes clear why we are so unfamiliar with the concept of plasma in our every day life; electrons are tightly bound to atoms and it takes a lot of energy to release them. Therefore, high temperatures are involved in the creation of a plasma at atmospheric pressures, temperatures we fortunately do not often experience.

In space, plasmas occur much more frequently. In fact, it is estimated that more than 90% of the (visible) universe is in the plasma state. This means that *plasma is the most common state of matter in the (visible) universe* [1]. Stars (and planets) are continuously born from huge, but very cold plasmas called *molecular clouds*. These, in a way, are enormous recycling factories in which the remnants of stars which have since long ceased to exist, are again used to form new stars.

Stars (like the Sun) are made of very hot plasma. In this plasma environment the internal engine of the stars burns through the process of fusion. In this process two ions are accelerated to energies high enough to overcome the repelling electrostatic force between them, allowing them to come so close together that the nuclear force binds them together to form a heavier element. Due to the binding energy, the separate ions are heavier than the new element formed by the ions fused together. This mass-deficit corresponds to a gain in energy, which is released in the form of energetic γ -photons. After more than 10^5 years of being

absorbed and re-emitted, do these photons finally escape the Sun at a wavelength roughly between the UV and the infrared [2]. Hot particles near the surface are also able to escape away from the star, resulting in a constant stream of energetic particles pouring into space, called the *stellar wind*. This stellar wind fills the interstellar space, resulting in yet another, albeit a very tenuous, plasma.

The interaction of emitted photons and the stellar wind with objects orbiting stars results in even more plasmas. The bright *tails of comets* close to the Sun consist of gas evaporating from the surface of the cometary core, ionized by the intense solar radiation, see the example in figure 1.1. The glow of the *polar lights* is emitted by plasma, formed by highly energetic particles originating from the solar wind interacting with molecules in the Earth's atmosphere. These solar wind particles are guided there by the helio- and geomagnetic fields, together forming the magnetosphere.



Figure 1.1: The Hale-Bopp comet close to the Sun. Two tails are visible: the tenuous plasma tail on the left, glowing blue in this picture, and the bright white dust tail on the right. The difference in angle is due to the light pressure induced by photons emitted by the Sun. The heavy dust particles are not influenced much by this light pressure and therefore the dust tail is directed along the orbital path of the comet. The plasma tail always points directly away from the Sun.
Courtesy of Wei-Hao Wang, IFA

The upper part of the atmosphere is called the *ionosphere* and is the result

of ionization of oxygen (O_2), nitrogen (N_2) and nitric oxide (NO) by ultraviolet (UV) and soft Röntgen (X-ray) radiation from the Sun (during daytime) and by ionization through interactions between cosmic ray particles and the air [3, 4]. The free electrons present in the ionospheric plasma reflect electromagnetic waves, a property well known for its use in long-range radio communication.

In the atmosphere, charging of water vapor inside clouds can lead to electric fields strong enough to guide electric currents to run through the insulating air. Even though there are several types of these discharges, the most common one, usually visible between the clouds, or between the clouds and the ground, is called *lightning*. The light emitted by the lightning is due to the heating of the air by the current, resulting in a hot, but very short-lived plasma.

Ever since techniques both to pump gases in a confined volume to low pressures, as well as to apply large electric potentials to metallic surfaces were invented, plasmas are widely present in laboratories and in industry, introducing plasma to more human scales. Currently, one of the biggest efforts in plasma physics is to harness the power of fusion in order to find a new way to produce energy in large amounts. A promising concept uses a hot plasma confined by strong magnetic fields in a device called a Tokamak. In this device, a plasma is heated to 150 million degrees Celsius. The magnetic fields are used to keep the hot plasma away from the walls, which ensures that the plasma remains hot enough for hydrogen to fuse into helium. The field of fusion research, or high temperature plasma physics, has shown such a strong progress that in 2015 the world's first burning plasma experiment, ITER, will become operational. This device is being constructed in Cadarache, in the south of France, and will produce more energy than is needed to sustain the fusion process, during pulses of several minutes. ITER allows fusion science to progress towards a commercially viable fusion device within the next 50 years, or so. Therefore, fusion is a promising source of energy, which could help solve the energy problem.

Many everyday appliances involve plasmas at more moderate temperatures¹. These include gas discharge lighting, such as neon lighting used for commercial purposes, and fluorescent lighting, such as compact fluorescence light sources (CFL's), which have a higher efficiency than the traditional incandescent light sources. Modern display techniques include plasma screens, in which small plasma discharges are used to excite a phosphor layer, which then emits light. Organic light-emitting diodes (or OLEDs) can be used as light sources or as display panels, and are partly produced with the help of plasma assisted chemical vapor deposition [5].

¹Many of the plasmas discussed in this thesis are at temperatures of a few electronvolts (eV). One electronvolt corresponds to a temperature of $e/k_B = 11604.5$ K, or roughly twice the temperature of the visible surface of the Sun.

In modern microchip industry small structures are build with the help of plasma [6]. Next generation microchips require bright sources of extreme ultraviolet (EUV) photons. The idea is to use plasmas to create these photons [7]. Solar cells are build using plasma deposition techniques and surfaces can be treated with plasmas, for instance to change the wettability or the surface roughness of artificial limbs or dental implants [8]. Plasma sources are even used for direct sterilization of contaminated surfaces or for the treatment of cancer cells [9].

In many of the above processes, chemically active gases are used to make plasmas or are introduced into plasma. Through chemical nucleation, small particles, consisting of several hundreds of atoms, form in these plasmas. Coagulation between these particles results in larger particles with a size up to 100 nm. Finally, attachment of radicals on their surface leads to micron sized particles [10]. In fusion plasmas, violent plasma-wall interactions can lead to the introduction of very large particles in the plasma volume, up to several millimeters in size, which are often redeposited at different locations, as shown in figure 1.2 taken from [11]. Plasma containing dust particles is usually referred to as dusty plasma, but is also known as 'colloidal' or 'complex' plasma.

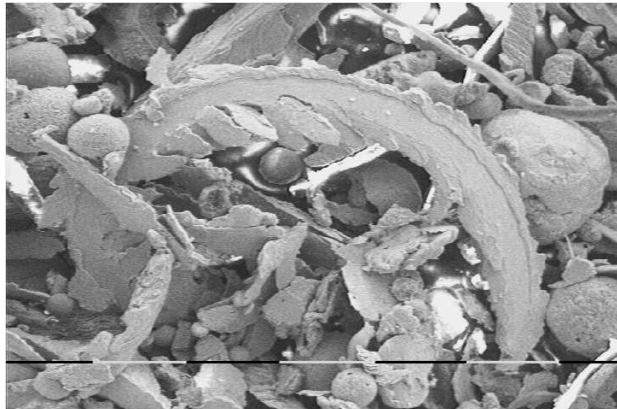


Figure 1.2: Dust found in the divertor region of the TEXTOR fusion experiment. The black and white line indicates intervals of 0.1 mm. Figure adapted from [11].

1.2 Dusty plasma

The formation and presence of dust in plasma discharges has been widely investigated both experimentally, e.g. [12], as well as numerically [13, 14]. In some cases, it was found that the presence of dust particles had a positive influence on

the efficiency of solar cells [15, 16], whereas small "killer particles" can destroy microchips during their plasma enhanced fabrication [17].

In any case, dust particles collect electrons and ions from the plasma, which means they become electrically charged. In laboratory plasmas, the higher mobility of the electrons as compared to the ions leads to a negative dust charge. A micrometer sized dust particle can have a negative charge of several thousands of electron charges. This means that in laboratory plasmas, dust is confined inside plasma discharges by the electric field, since the outer parts of discharges also become negatively charged with respect to the bulk of the plasma.

Another important force acting on the dust particles results from the positive ions being collected and deflected by the negatively charged dust particles. Furthermore, dust particles will interact with each other through the mutual Coulomb interaction, which can result in the formation of several types of dust structures.

Since dust collects plasma, the presence of dust strongly influences the plasma properties, such as the plasma densities, potential, and the energy distribution functions of the plasma particles. This means that ways to control the formation of the dust, or ways to control the dust once it is formed, are desirable for an efficient use of plasmas in industry. Furthermore, magnetic fields are often used, as in magnetron sputtering devices or fusion devices. The role of magnetic fields must therefore be taken into account for many relevant dusty plasmas.

Dusty plasmas are also interesting from a more fundamental point of view. To understand the behavior of cometary tails, the rings around Saturn, or noctilucent clouds, one has to understand the charging properties of dust particles. The formation of stars, such as the Sun, also involves dusty plasma.

Stars are born from large atomic and molecular clouds, which fill up interstellar space. When these clouds are locally perturbed, for instance by a passing shock wave originating from a nearby supernova explosion, a small part of the cloud starts to collapse under the influence of gravity. During this collapse, the gas heats up due to internal friction, which increases the pressure that counters the collapse under the force of gravity. Unless there is an efficient heat-removal mechanism, the clouds will then stop collapsing.

Dust particles in the plasma are efficient radiators and will, at intermediate dust densities, remove the excess heat, allowing the molecular clouds to collapse further. During the later stages of star formation, the heat produced during collapse is actually needed to ignite the young star at the center of the cloud. Dust at higher densities can no longer emit the energy outwards, but actually keeps the heat inside the system. The pressure and temperature in the core of the collapsing molecular cloud keep building up, until ignition occurs. From then on, the fusion processes dictate the energy balance of the system, and a star is born [18, 19].

Once the star is ignited, the light pressure will remove most of what remains of the molecular cloud, until only a rotating disk of plasma and dust remains, an

example of which is shown in figure 1.3. It is believed that from the micron-sized dust particles in these disks, planets form through the coagulation of these particles to larger and larger objects [20, 21]. Indeed, recent experiments seem to support that idea [22, 23], while recent observations around young stellar objects prove the presence of both amorphous as well as crystalline dust around young stars [24, 25].

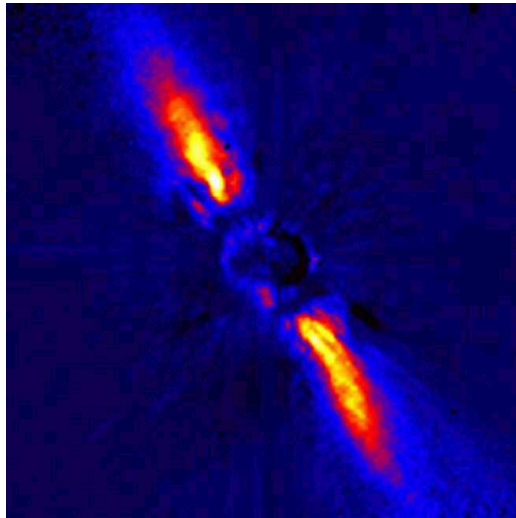


Figure 1.3: A coronagraphic picture of the dust disk around a nearby young star, β -Pictoris. The bright light from the young star has been blocked, using a coronagraph. The bright, yellow regions correspond to the disk of dust and gas orbiting the young star. *Courtesy of J. L. Beuzit et al., Grenoble Observatory, ESO*

How these dust particles coagulate on the short timescales required by cosmological theories, is still an unanswered question, especially since they should become negatively charged in the plasma around the young star. Jets and matter outflows observed in such objects are indications of the presence of strong magnetic fields, which might play an important role in the star and planet formation processes [26]. Energetic particles from space, as well as strong UV radiation from the central young star might interact with the dust, removing electrons from the dust. This might increase the probability of dust coagulation.

It is clear from the above that a good understanding of dusty plasmas is required to optimize many industrial applications of plasma, but also to fully comprehend the process of star and planet formation. This better understanding includes an understanding of the role of magnetic fields in dusty plasma, the interaction between the plasma and the dust, the forces acting on the dust, and of

course the effect of dust on the plasma parameters, as well as an understanding of the charging of dust particles through different charging processes.

The behavior of dusty plasmas, especially in the presence of magnetic fields and UV radiation, has been investigated with different numerical models, but also in an experimental study of magnetized dusty plasma discharges. By presenting the results of these studies, this thesis intends to bring a better insight into this behavior, both from a fundamental, as well as a practical point of view.

1.3 Previous work, Contribution of this thesis

In the past, numerical codes for the simulation of RF discharges were developed. A fluid model was used to simulate the deposition of silicon for the fabrication of solar cells in silane discharges [27, 28]. This model was then expanded to include the dust component coupled to the plasma solutions and was used to simulate results from microgravity experiments [29].

This model includes the dust charging problem, recombination of plasma particles on the dust particles and the corresponding heating of the dust. From the interaction between the plasma and the dust, the forces acting on the dust particles are calculated and from these forces the dust transport through the plasma, where the problem of the huge difference in transport time of the plasma particles (as short as nanoseconds for electrons) and the dust particles (as long as seconds for micrometer sized dust particles) is dealt with.

We have extended this code with a more sophisticated form for the interaction between ions and dust particles, including analytical forms for calculating this force in the presence of significant ion flow speeds and ion-neutral collisions, and we added the effect of charge exchange collisions on the charging of dust particles. We also computed the effect of a homogeneous magnetic field on the transport of plasma particles perpendicular to this field, and the corresponding effect on the dust transport through the plasma. Finally, we modelled the effect of a homogeneous flux of UV ions on the charging of dust particles and investigated the effect on dust transport and the void formation.

In fluid codes, time and space averaged plasma properties are calculated by solving the balance equations for the plasma particle densities and the energy density, often by using the so called *drift-diffusion approximation*. Another technique, called Particle-In-Cell plus Monte Carlo (PIC/MC), follows a large collection of super particles in real time and solves the equation of motion for every super particle. The electric field, which moves the particles, is found by solving the Poisson equation, which gives the electrostatic potential calculated from the charge density, which is interpolated from the positions of the super particles. Collisions between plasma particles and background neutrals are included in the

Monte Carlo scheme. They do not collide with or among each other however, see e.g. [30].

The latter type of models allows to examine the physics of plasmas on very short time scales and very small length scales. Such a model in one dimension was previously developed, including collisions between the plasma particles and a static dust distribution, where the dust charging was solved [31]. We have extended this model with an intense UV flux and the effect of this flux on the dust charge as well as the ionization of the background gas by this UV flux, including the effect of optical depth.

1.4 Outline thesis

The focus of this thesis is on the interaction between plasma and dust particles immersed in this plasma, and on the effect of magnetic fields and UV radiation on dusty plasmas.

Chapter 2 deals with the general theory of dusty plasma, together with a short description of the fluid code and Particle-In-Cell/Monte Carlo code used to obtain the results of this thesis.

Chapter 3 presents modelling results for the fluid code extended with an axial magnetic field, especially focussing on the effect of the magnetic field on the transport of the dust through the experiment and the formation of the so called *void* structure.

Chapter 4 deals with experimental measurements on the response of complex plasmas in a DC discharge with an applied magnetic field. It explains the different experimental techniques used to characterize the dusty plasma, as well as the secondary effect of applying a magnetic field when an electric field is present, namely $\mathbf{E} \times \mathbf{B}$ drifts of plasma particles and induced dust drift.

Chapter 5 presents results of the fluid code on the interaction between ions and dust particles. It describes the specific problem of non-linear scattering of ions in the potential around dust particles, together with the effect of ion flow speed and ion-neutral collisions on the transfer of momentum on the dust, as well as on the dust charging, and how these effects have been implemented in the fluid code.

Chapter 6 shows the effect of the dust on the plasma parameters, especially looking at the effect on the electron density and temperature. Special attention is given to where the energy required for the ionization inside the dust free void originates from and what role the electrons play in the process of void formation.

Chapter 7 shows results from the PIC/MC code on the effect of UV radiation on the dusty plasmas modelled. The chapter focuses on the reduction of dust charge by the effect of photo-detachment, while at the same time looking at the ef-

fect of the photo-detached electrons on the discharge. It also shows computations on the dynamic response of dusty plasma to a short pulse of UV light.

A general overview and the conclusions of this thesis are then presented, as well as recommendations for future research.

1.5 Publications related to this thesis

Refereed journal articles related to chapters of this thesis

- V. Land, W. J. Goedheer, and M. R. Akdim, *Dust transport in a magnetized radio-frequency discharge under microgravity conditions*, Physical Review E, Vol **72**, 046403, (2005) Chapter 3
- V. Land, and W. J. Goedheer, *Effect of large-angle scattering, ion flow speed and ion-neutral collisions on dust transport under microgravity conditions*, New Journal of Physics, Vol **8**, 8 (2006) Chapter 5
- V. Land, and W. J. Goedheer, *The plasma inside a dust free void: Hotter, denser, or both?*, New Journal of Physics, Vol **9**, 246 (2007) Chapter 6
- V. Land, and W. J. Goedheer, *Manipulating dust charge using ultraviolet light in complex plasma*, IEEE Trans. Plasma Sci., Vol **35**, Issue 2, Part 2, 280-285 (2007) Chapter 7

Articles not related to this thesis

- W. J. Goedheer, M. R. Akdim, and V. Land, *Transport of dust in low-pressure RF discharges*, High Temperature Material Processes, Vol. **8**, P. 139-148 (2004)
- W. J. Goedheer, and V. Land, *Shrinking voids and Yukawa-balls in RF-discharges under micro-gravity*, Submitted to Physical Review Letters, 2007
- V. Land, and W. J. Goedheer, *The role of self-organization in dusty plasmas under micro-gravity*, in preparation

Oral contributions to various international workshops and conferences

The contributions below marked with * were accompanied by a 4-paper conference proceeding.

1. * V. Land, W. J. Goedheer, and M. R. Akdim, *Transport of dust in plasmas with magnetic field and UV-radiation*, 31st European Physical Society Conference on Plasma Physics, London, United Kingdom, June 28 - July 2 (2004)
2. V. Land and W. J. Goedheer, *Dust transport and azimuthal flow in dusty magnetized RF discharge*, 7th Workshop on the Exploration of Low Temperature Plasma Physics, Kerkrade, The Netherlands, November 25-26 (2004)
3. V. Land, W. J. Goedheer, *Dusty plasmas in the presence of ultra-violet light*, 18th NNV/CPS Symposium on Plasma Physics and Radiation Technology, Lunteren, the Netherlands, March 22-23 (2006)
4. V. Land, W. J. Goedheer, *Manipulating dust in plasma with UV, Particle-In-Cell plus Monte Carlo simulations*, 11th Workshop on the Physics of Dusty Plasmas, Williamsburg, VA, United States of America, June 28 - July 2 (2006)
5. V. Land, W. J. Goedheer, *Can we Use UV light to control dust charging? An investigation using Particle-In-Cell/Monte Carlo simulations*, Diagnostics and Simulation of Dusty Plasmas, Kiel, Germany, September 13 - 15 (2006)
6. W. J. Goedheer, V. Land, M. R. Akdim, *Simulation of dust voids*, Diagnostics and Simulation of Dusty Plasmas, Kiel, Germany, September 13 - 15 (2006)
7. * V. Land, W. J. Goedheer, *Electrons in a dust free void: "Hotter or denser?"*, 34th European Physical Society Conference on Plasma Physics, Warsaw, Poland, July 2-6 (2007)

Poster contributions to various international workshops and conferences

1. V. Land, W. J. Goedheer, and M. R. Akdim, *Toward the understanding of Astronomical Dusty Plasmas: Modelling of asymmetric and magnetized plasmas*, 16th NNV/CPS Symposium on Plasma Physics and Radiation Technology, Lunteren, the Netherlands, March 16-17 (2004)
2. * V. Land, and W. J. Goedheer, *Charged dust particles in a RF and UV-driven plasma*, 4th International Conference on the Physics of Dusty Plasmas, Orléans, France, June 13 - 17 (2005)
3. * V. Land, E. Thomas, Jr., and Jeremaiah Williams, *Dust transport and force equilibria in magnetized dusty DC discharges*, 4th International Conference on the Physics of Dusty Plasmas, Orléans, France, June 13 - 17 (2005)

4. * V. Land, E. Thomas, Jr., and Jeremaiah Williams, *Dust transport and force equilibria in magnetized dusty DC discharges*, 47th Annual Meeting of the Division of Plasma Physics, Denver, CO, United States of America, October 24 - 28 (2005)
5. * W. J. Goedheer, M. R. Akdim, and V. Land, *Void formation and dust cloud structure in (a)symmetric RF discharge*, 4th International Conference on the Physics of Dusty Plasmas, Orléans, France, June 13 - 17 (2005)
6. V. Land, W. J. Goedheer, *MC-PIC modelling of multiple dust species in plasma with UV radiation*, 8th Workshop on the Exploration of Low Temperature Plasma Physics, Kerkrade, The Netherlands, November 24-25 (2005)
7. V. Land, W. J. Goedheer, *Ion-dust interactions in dusty plasmas*, 18th NNV/CPS Symposium on Plasma Physics and Radiation Technology, Lunteren, the Netherlands, March 21-22 (2006)
8. V. Land, W. J. Goedheer, *Dynamic response of dusty plasma to UV radiation*, 9th Workshop on the Exploration of Low Temperature Plasma Physics, Kerkrade, The Netherlands, November 23-24 (2006)
9. * V. Land, W. J. Goedheer, *Dynamic response of dusty plasma*, 34th European Physical Society Conference on Plasma Physics, Warsaw, Poland, July 2-6 (2007)

Seminars

- *Ion drift in magnetized dusty discharge and induced dust flow*, Auburn University, Auburn, AL, United States of America, March 17 (2005)
- *Computing the complex, simulations of dusty plasmas*, Ruhr University Bochum, Bochum, Germany, November 16 (2006)
- *Creation and closing of dust free voids in dusty plasma*, University of Antwerp, Antwerp, Belgium, June 4 (2007)

References

- [1] J. P. Goedbloed, and S. Poedts, *Principles of Magnetohydrodynamics with applications to laboratory and astrophysical plasmas*, Cambridge University Press, Cambridge, (2004)
- [2] R. Mitalas, and K. R. Sills, *Astrophysical Journal* **401**, 759 (1992)
- [3] E. O. Hulburt, *Physical Review*, **53**, 344-351 (1938)
- [4] P. Meyer, E. N. Parker, and J. A. Simpson, *Physical Review* **104**, 3, 768-783 (1956)
- [5] H.-K. Kim, M. S. Kim, J.-W. Kang, J.-J. Kim, M.-S. Yi, *Appl. Phys. Lett.* **90**, 013502 (2007)
- [6] S. Tachi, *J. Vac. Sci. Technol. A* **21**, S131 (2003)
- [7] A. P. Shevelko, L. A. Shmaenok, S. S. Churilov, R. K. F. J. Bastiaansen, and F. Bijkerk, *Phys. Scr.* **57**, 276-282 (1998)
- [8] M. A. M. Silva, A. E. Martinelli, C. Alves Jr., R. M. Nascimento, M. P. Távora, and C. D. Vilar, *Surface & Coatings Technol.* **200**, 2618-2626 (2006)
- [9] E. Stoffels, A. J. Flikweert, W. W. Stoffels, and G. M. W. Kroesen, *Plasma Sources Sci. Technol.* **11**, 383-388 (2002)
- [10] K. De Bleecker, A. Bogaerts, and W. Goedheer, *New J. Phys.* **8**, 178 (2006)
- [11] J. Winter, *Plasma Phys. Control. Fusion*, **40**, 1201 (1998).
- [12] W. W. Stoffels and E. Stoffels, *Trends Vac. Sci. Technol.* **4**, 1 (2001)
- [13] K. De Bleecker, A. Bogaerts, R. Gijbels, and W. Goedheer, *Phys. Rev. E* **69**, 056409 (2004)
- [14] K. De Bleecker, A. Bogaerts, and W. Goedheer, *Phys. Rev. E* **70**, 056407 (2004)

-
- [15] C. Longeaud, J. P. Kleider, P. Roca i Cabarrocas, S. Hamma, R. Meaudre, and M. Meaudre, *J. Non-Cryst. Solids* **227-230**, 96 (1998)
- [16] M. Meaudre, R. Meaudre, R. Butté, and S. Vignoli, *J. Appl. Phys.* **86**, 946 (1999)
- [17] G. S. Selwyn, J. Singh, and R. S. Bennett, *J. Vac. Sci. Technol. A* **7**, 2758 (1989)
- [18] F. H. Shu, In: *The Milky Way Galaxy*, Proceedings of the 106th Symposium Groningen, The Netherlands, P. 561-566 (1985)
- [19] R. Chini, E. Krügel, and E. Kreysa, *A&A* **167**, 315-324 (1986)
- [20] S. J. Weidenschilling, and J. N. Cuzzi, *Protostars and Planets III*, 1031, 1993
- [21] S. V. W. Beckwith, T. Henning, and Y. Nakagawa, *Protostars and Planets IV*, 533 (2000)
- [22] T. Poppe, J. Blum, and T. Henning, *Astr. J.* **533**, 454-471, (2000)
- [23] T. Poppe, J. Blum, and T. Henning, *Astr. J.* **533**, 472-480, (2000)
- [24] Y. K. Okamoto *et al.*, *Nature (London)*, **431**, 660 (2004)
- [25] C. M. Telesco *et al.*, *Nature (London)*, **433**, 133 (2005)
- [26] G. T. Birk, *Astron. Astrophys.* **330**, 1070 (1998)
- [27] J. D. P. Passchier, *Numerical fluid models for RF discharges*, Ph.D. Thesis, University Utrecht, The Netherlands, 1994
- [28] G. J. Nienhuis, *Plasma models for silicon deposition*, Ph.D. Thesis, University Utrecht, The Netherlands, 1998
- [29] M. R. Akdim, *Modelling of Complex Plasmas*, Ph.D. Thesis, University Utrecht, The Netherlands, 2003
- [30] C. K. Birdsall, *IEEE Trans. Plasma Sci.*, **19** (1991), 65-85
- [31] W. J. Goedheer, Y. I. Chutov, *IEEE Trans. Plasma Sci.*, **32** (2004) 551-554

2. Theory of dusty plasma

As was already mentioned in the introduction, plasma is a very common state of matter in the universe. In our everyday life, we are not often confronted with it though. This needs some more explanation about how plasmas actually form and which techniques are used in laboratories all over the world to make plasmas.

In order to appreciate statements about dusty plasmas, a basic understanding of several plasma properties needs to be provided. These properties include so called quasi-neutrality, the screening of charges by plasma, a knowledge about how dust particles charge up in a plasma, and which forces will then act upon them.

This chapter tries to do all that, explains the phenomenon of void formation in dusty plasmas under micro-gravity, and gives an overview of the numerical methods with which the results presented in this thesis are obtained.

2.1 Creating a plasma

A plasma consists of a mixture of charged particles, electrons and ions, and neutrals. The ratio of ions (for instance Ar^+) over the total particle density, $x = n_+/(n_N + n_+)$ (in this example then $x_{\text{Ar}^+} = \text{Ar}^+ / (\text{Ar} + \text{Ar}^+)$) is called the *ionization fraction* and differs for different types of plasmas. In a fusion experiment it will be much higher than in a gas discharge light source. For a plasma where locally the volume production balances the volume losses, for instance electron impact ionization and three-particle recombination, the ionization fraction can be described by the Saha equation [1]. Assuming that all the components of the plasma have the same temperature ($T_N = T_+ = T_e \equiv T$), i.e. assuming that the plasma is in *thermal equilibrium*, this equation becomes

$$\left(\frac{x}{1-x}\right) n_e = \frac{2U_{r+1}}{U_r} \left(\frac{2\pi m_e k_B T}{h^2}\right)^{3/2} e^{-\chi_r/k_B T}, \quad (2.1)$$

where $U_y \equiv \sum_s g_{y,s} e^{-\chi_{y,s}/k_B T}$ is the partition function of the ionized state y which has s degenerate states with statistical weight g_s , χ_r is the ionization energy needed to go from state $r - 1$ to r , typically an energy of several eV, and the term $(\dots)^{3/2}$ is the cube of the reciprocal of the de Broglie wavelength.

For gases where only one ionization level is important, such as atomic hydrogen, the electron density can be expressed in terms of the total pressure, $n_e k_B T = n_{tot} k_B T (x/(x+1)) = P_{tot} (x/(x+1))$, where $n_{tot} = n_e + n_+ + n_N$. This leads to the following expression for the ionization fraction, x ,

$$\left(\frac{x^2}{1-x^2}\right) = \frac{2U_{r+1}}{U_r} \left(\frac{2\pi m_e k_B T}{h^2}\right)^{3/2} \frac{k_B T}{P_{tot}} e^{-\chi_r/k_B T}. \quad (2.2)$$

We can see that for increasing pressure, a higher temperature is needed to achieve the same ionization fraction. This is due to the increasing chance of recombination at higher pressures. We also see that at fixed pressure, the ionization degree increases for increasing temperature, which is due to the fact that on average the collisions become more and more energetic. Filling in the numbers and using $U_r = 2$ and $U_{r+1} = 1$, we find for partly ionized gases ($n_+ < n_N$) [2],

$$x \sim \frac{n_+}{n_N} \approx 2.4 \times 10^{21} \frac{T^{3/2}}{n_+} e^{-\chi_r/k_B T}. \quad (2.3)$$

From the above equation it is clear that very high equilibrium temperatures are needed to get even a modest ionization fraction, because of the exponential term. This is also the reason why we are not used to the plasma state on Earth; both the gas temperatures are too low, and the neutral gas pressures are too high.

In experiments, such as described in this thesis, the ionization fraction is very low ($x \leq 10^{-6}$), so that the energy transfer from the electrons to the ions and neutrals is insufficient to reach local equilibrium. On the contrary, electron impact ionization is balanced by (Bohm) losses to the walls, or, in the presence of dust, in combination with recombination of plasma on the dust particles. Both the ionization as well as the (Bohm) loss terms are described by the electron temperature, T_e , but of course, the ionization is an exponential function of the temperature, whereas the losses are proportional to the square root of the temperature. The recombination of the dust is somewhat more complicated, but can also be described by the electron temperature.

So, in low pressure experiments, the balance is not given by the Saha equation, but by a non-local balance between production and losses. This balance is dominated by the electron temperature. Due to the high electron mobility, electrons can be efficiently heated to several electronvolts by the use of electric fields, whereas the heavy particle temperature can be close to room temperature.

There are many different types of plasma devices, one of which is the so called *direct current glow discharge* (DC discharge). Such a device was used to obtain the results presented in chapter 4. It will also be described below. In such a device, one of the electrodes is biased negatively (called the cathode), whereas the other is grounded or biased positively, resulting in a stationary electric field, which accelerates the charged species.

Another type of discharge, discussed in chapters 3, 5, 6 and 7, is the *radio frequency discharge* (RF discharge). In this case, one or both of the electrodes is powered with a sinusoidal signal, usually at 13.56 MHz. In this thesis, all the RF

discharges are modelled with a RF frequency of 13.56 MHz. This frequency is too high for the heavy ions to respond to, so that only the electrons are effectively heated by the electric field providing the energy for electron impact ionization. For most of these experiments we have $x \leq 10^{-6}$. This also means that the dominant class of collisions is between charged plasma particles and neutrals, and not collisions between charged plasma particles.

2.1.1 DC discharge

The oldest form of plasma discharges consists of a straight closed cylinder pumped to low pressures. A gas is introduced in the cylinder, which has two conducting electrodes at both ends. A constant negative potential is then applied to one of the electrodes (the *cathode*). The other electrode (*anode*) can be positively biased, but here we restrict ourselves to a grounded anode.

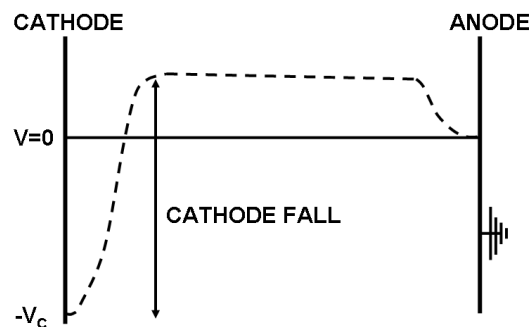


Figure 2.1: Schematic drawing of a simple DC discharge, with the dashed line showing the plasma potential. Sheaths build up, connecting the electrode potential to the bulk plasma potential. In these sheaths the electric field is large, accelerating electrons away from the electrodes. In the bulk, the electric field is very small. In the cathodic region, the largest potential difference occurs, called the "cathode fall". The true electric field in a DC discharge is much more complicated than shown here.

Due to random processes, like radiation from natural radio-active sources or energetic particles originating from cosmic rays, either atoms in the volume are ionized, or electrons are emitted from one of the electrodes. The electrons are

then accelerated in the electric field, away from the cathode, and gain energy. In inelastic processes they excite and ionize the background gas, resulting in more charged particles. The positive ions are accelerated towards the cathode and emit electrons on colliding with the cathode through the process of secondary electron emission. These electrons are again accelerated away from the cathode and a self-sustaining discharge is born.

At constant applied potential, a constant current will run, therefore such a discharge is called *direct current glow discharge*, or DC discharge. The main source of ionization in these discharges is due to the secondary electrons emitted from the cathode by ion-impact. This is called γ -ionization. A schematic picture of the most simple type of DC discharge is shown in figure 2.1.

2.1.2 Capacitively coupled RF discharge

When plasma is used to deposit layers, the electrode on which they are deposited is often rapidly covered with layers of insulating material, such as carbon containing compounds. In a DC discharge this electrode would therefore charge up until the discharge would extinguish. In order to overcome this problem, one can apply an alternating potential instead of a constant potential difference between the electrodes, so that both electrodes would become the anode and cathode alternately. This would allow the charge build up during half the cycle to be neutralized during the second half of the cycle. This is the principle behind *alternating current*, or AC discharges.

A special type of AC discharge is the *radio-frequency*, or RF discharge, which is powered by an alternating potential with a driving frequency in the radio-frequency range. One frequency often used (simply because it has been reserved for science research by international rules on radio-communication) is 13.56 MHz. This high frequency means that electrons can follow it instantaneously, but not the ions, since $\omega_{p,+} \lesssim \omega_{RF} \ll \omega_{p,e}$ for argon gas and plasma densities in the range of $n_e = n_+ \sim 10^{15} \text{ m}^{-3}$, with the plasma frequencies given by

$$\omega_{p,j} = \sqrt{\frac{n_j e^2}{m_j \epsilon_0}}. \quad (2.4)$$

This means that ions only see the (moderate) effective electric field, see equation 2.65, whereas electrons are accelerated in the (much stronger) instantaneous field. This also means that secondary electron emission is in general of minor importance for sustaining the discharge and that most of the excitation and ionization is due to fast electrons moving in the bulk of the discharge. This is called α -ionization.

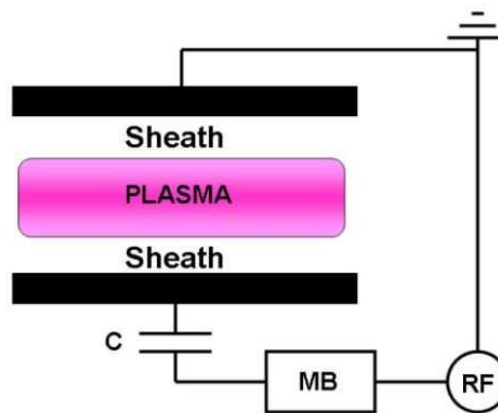


Figure 2.2: Schematic view of a typical RF discharge. The radio-frequency potential (RF) is coupled to the lower electrode through a matching box (MB), which allows the impedance to match the complex impedance of the plasma-sheath system (which could be represented by two capacitors in series with a resistor), and a blocking capacitor (C), which allows the build-up of a self-bias on the powered electrode.

Under certain circumstances (for instance when the size of both the electrodes is not equal), a self-bias can occur. During one half of the RF cycle, the amount of negative charge collected is then not neutralized during the second half of the cycle. This results in a negative charge on the electrode. This will continue until the extra negative charge repels enough of the extra electrons to the electrode so that the total electron and ion flux during one cycle becomes equal again. In this case, the negative bias can result in significant ion impact and then secondary electron emission can again become important, which can result in a significant γ contribution to the discharge. This process is referred to as the $\alpha - \gamma$ transition. In this thesis we will model symmetric *capacitively coupled* RF discharges, with negligible self-bias.

The term *capacitively coupled* refers to how the power is coupled to the plasma. In this case, the electrodes together with the sheaths act as a capacitor, as indicated in figure 2.2. It is also possible to couple the power by applying a time-varying magnetic field, which induces an electric field in the plasma. These discharges are called *inductively coupled* RF discharges. These are beyond the scope of this thesis. A broad overview of plasma discharges can be found in [3], whereas a numerical comparison between DC and RF discharges can be found in [4].

2.2 Properties of dusty plasma

Plasma has some very specific properties, but the presence of dust particles in the plasma alters these properties slightly. Looking from "far away" to an isolated plasma, one would not see any net charge of the plasma, since for every ionic charge created, a corresponding electron is created. This is called *quasi-neutrality*. This quasi-neutrality still holds when dust particles are introduced, even though these particles act like 'sponges', collecting electrons and ions, and *become charged*.

Micrometer sized particles can carry a considerable amount of charge on their surface. The fact that these large charges are not seen from far away means that the plasma organizes itself in such a way as to *screen* these charges from the surrounding plasma. Beyond a certain distance from the charge, which is called the *screening*, or *Debye length*, usually indicated by the symbol λ_D , the potential of the charged particle is no longer experienced by another charge¹, which also determines what "far away" means.

We now continue to define these notions mathematically, using simple physical considerations. We start with showing why a plasma is quasi-neutral except within the small length-scale of the Debye length.

2.2.1 Quasi-neutrality

To derive the condition for quasi-neutrality, we start with a neutral plasma with a homogeneous electron and ion background density, $n_{e0} = n_{+0} \equiv n_0$, at constant finite temperature throughout the volume of the plasma, i.e. $\nabla T_e = \nabla T_+ \equiv 0$.

When the ion density is disturbed locally, see figure 2.3, so that $n_+ \rightarrow n_0 + n_{+1}$, the induced net space charge accelerates the electrons towards the region of increased ion density. However, with this acceleration, an electron gradient builds up, which results in a pressure gradient acting in the opposite direction. Due to this restoring force, a net space charge remains within a small volume of the plasma.

The exact spatial extent of this charge separation can be derived from the force balance of the electrons after the perturbation,

$$\mathbf{F}_e = -en_e\mathbf{E} - \nabla P_e = 0. \quad (2.5)$$

Here, the electric field is due to the induced charge separation,

$$\nabla \cdot \mathbf{E} = \frac{\rho}{\epsilon_0} = \frac{e(n_{+1} - n_{e1})}{\epsilon_0}. \quad (2.6)$$

¹In fact, the Debye length is defined as the length where the strength of the potential around a charge is $1/e \approx 0.37$ times the potential at the position of the charge. So another charge would still experience some potential, but it will in principle be a small fraction of the particle potential.

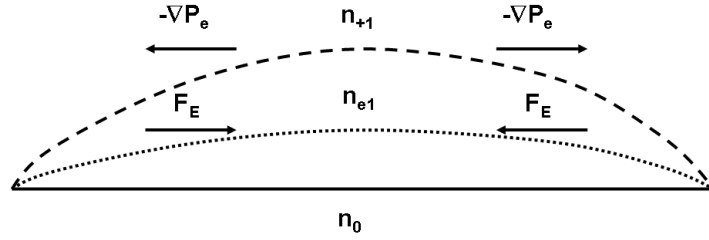


Figure 2.3: Illustration of a perturbation to a homogeneous plasma with initial plasma density n_0 . The ions are perturbed. The electrons respond to the positive space charge. This results in an electron pressure gradient which acts against the electric force. A net charge separation is the result.

Taking the divergence of equation 2.5, assuming the ideal gas law for the electrons, $P_e = n_e k_B T_e$, and assuming constant electron temperature during the perturbation, $T_{e1} = 0$, we find

$$-e(n_0 + n_{e1})(\nabla \cdot \mathbf{E}) - e\mathbf{E} \cdot \nabla(n_0 + n_{e1}) - k_B T_e \nabla^2(n_0 + n_{e1}) = 0. \quad (2.7)$$

Remembering that the initial plasma was homogeneous, and that \mathbf{E} only depends on perturbed quantities, we use equation 2.6 and linearize to get

$$\frac{-e^2 n_0}{k_B T_e \epsilon_0} (n_{+1} - n_{e1}) - \nabla^2 n_{e1} = 0. \quad (2.8)$$

Assuming that the perturbation of the background densities is periodic in space, $n_{e1} \propto \sin(x/L)$, with L the characteristic length of the perturbation, so that $\nabla^2 n_{e1} = -n_{e1}/L^2$, we end up with

$$-\frac{(n_{+1} - n_{e1})}{\lambda^2} + \frac{n_{e1}}{L^2} = 0. \quad (2.9)$$

Here $\lambda = (\epsilon_0 k_B T_e / e^2 n_0)^{1/2}$ is the (electron) Debye length. We find this way,

$$n_{e1} \left(\frac{\lambda^2}{L^2} + 1 \right) = n_{+1}. \quad (2.10)$$

We see that $n_{e1} \approx n_{+1}$ if $L \gg \lambda$, so that the plasma is always neutral over distances larger than the Debye length, as long as the amplitude of the perturbation is small so that the problem can be linearized. Therefore, the quasi-neutrality condition in the absence of dust, for a plasma with only singly charged positive ions and electrons, can be written as:

$$n_+ - n_e = 0. \quad (2.11)$$

2.2.2 Quasi-neutrality with dust

Particles in a plasma collect ions and electrons and become charged. Due to the high electron mobility, this charge will in general be negative, as will be explained in section 2.2.4. Therefore, the dust charge must be taken into account when rewriting equation 2.11 for the case where dust is present. It therefore reads

$$n_+ - n_e - n_D \frac{Q_D}{e} = 0, \quad (2.12)$$

with $Q_D = eZ_D$ the dust charge.

Since in a dusty plasma the ions are no longer the heaviest species, the screening of charged dust particles will be some combination of screening by the mobile electrons and the less mobile positive ions in the plasma. We will derive the appropriate screening length in the next section.

2.2.3 Screening

We consider the response of plasma to a dust particle with surface charge $Q_D = eZ_D$, which is assumed to be known. To obtain this response we need to solve Poisson's equation,

$$\nabla \cdot \mathbf{E} = -\nabla^2 \phi(r) = \frac{\rho}{\epsilon_0} = -\frac{e}{\epsilon_0} (n_e - n_+). \quad (2.13)$$

We now make three approximations:

1. The energy distribution function of the ions and electrons are described by a Maxwellian distribution.
2. The dust charge is negative, so that the potential is repulsive for electrons and attractive for ions.
3. The disturbance caused by the charged particle is small, so that the potential energy of the ions and electrons is much smaller than their thermal energy.

The first approximation allows us to write the (collisionless) solution for the density of the electrons and ions around the dust particle, found from the Vlasov equation, by the Boltzmann distribution, $n_j \sim \exp(-E_{pot}/k_B T_j)$. The second approximation determines the sign in front of the exponential terms in this distribution, while the third allows us to linearize these exponential terms.

The potential energy for the electrons and ions respectively is $-e\phi(r)$ and $e\phi(r)$, so that we can write the densities as,

$$\begin{aligned} n_e(r) &= n_\infty \exp\left(\frac{e\phi(r)}{k_B T_e}\right), \\ n_+(r) &= n_\infty \exp\left(\frac{-e\phi(r)}{E_s}\right). \end{aligned} \quad (2.14)$$

Here, n_∞ is the density of charged plasma particles far away from the test charge in the potential $\phi(r)$ around the charged particle.

For the ions we use the mean energy rather than $k_B T_+$ since ions can have drifts close to the sheaths in front of the electrodes. The mean energy is given by [5] $E_s = m_+ v_+^2 / 2 = m_+ (u_+^2 + 8k_B T_+ / \pi m_+) / 2$. $u_+ = \mu_+ E_{eff}$ is the ion (with mobility μ_+) drift velocity in the effective electric field E_{eff} . We can rewrite this in terms of the thermal ion Mach number, $M_T = u_+ / v_T = u_+ / \sqrt{8k_B T_+ / \pi m_+}$, as $E_s = m_+ v_T^2 (1 + M_T^2) / 2$.

Linearizing equations 2.14, and using them in equation 2.13, we end up with,

$$\nabla^2 \phi(r) = \phi(r) \frac{e^2 n_\infty}{\epsilon_0} \left[\frac{1}{k_B T_e} + \frac{\pi}{4k_B T_+ (1 + M_T^2)} \right], \quad (2.15)$$

which becomes:

$$\nabla^2 \phi(r) = \frac{1}{\lambda_D^2} \phi(r). \quad (2.16)$$

In this equation $\lambda_D^{-2} = \frac{e^2 n_\infty}{\epsilon_0} \left[\frac{1}{k_B T_e} + \frac{\pi}{4k_B T_+ (1 + M_T^2)} \right] = \left[\lambda_e^{-2} + \frac{\pi}{4(1 + M_T^2)} \lambda_+^{-2} \right]$. λ_D is called the *linearized Debye length*.

The solution to the above equation in spherical coordinates is given by the Debye-Hückel potential:

$$\phi(r) = \frac{Q_D}{4\pi\epsilon_0 r} \exp\left(\frac{-r}{\lambda_D}\right). \quad (2.17)$$

Close to the test charge, the $1/r$ term dominates and we see that the potential is simply the Coulomb potential around the test charge. Further away, the $\exp(-r/\lambda_D)$ term dominates and the potential falls off more rapidly, due to the screening of the test charge by the plasma.

One approximation often made is to write the above solution as:

$$\begin{aligned} \phi(r) &= \frac{Q_D}{4\pi\epsilon_0 r}, \quad \forall r \leq \lambda_D, \\ &= 0, \quad \forall r > \lambda_D. \end{aligned} \quad (2.18)$$

This is also the reason why sometimes it is said that; "charged particles do not 'feel' each other, when they are farther apart than the Debye length", but technically speaking this is not so.

An important assumption in this derivation is that the perturbation of quasi-neutrality by the test charge is small. This is not so when $e\phi(r)/k_B T_{e,+} \gtrsim 1$. In this case the linearization of the exponent is no longer valid. Making the assumption that this happens close to the test charge, we then have $\phi(r) = Q_D/4\pi\epsilon_0 r$. So the radius for which this deviation from linearity happens, is then given by:

$$r_{max} \equiv 2\rho_{0,e,+} = \frac{eQ_D}{4\pi\epsilon_0 k_B T_{e,+}}. \quad (2.19)$$

Since $T_e \gg T_+$, the largest radius applies to the ions. The above radius, ρ_0 , is referred to as the "Coulomb radius" and it defines the radius within which screening is a non-linear problem. Writing the ion Coulomb radius, using the ion Debye length, we find:

$$\rho_{0,+} = \frac{Z_D}{8\pi n_\infty \lambda_+^2}. \quad (2.20)$$

Making an estimate of the different sizes in a typical dust free plasma with $Z_D = q_+ \sim 1$ at room temperature and with a density of $n_\infty = 10^{15} \text{ m}^{-3}$, we find;

$$\rho_0 \propto \frac{\Delta^3}{\lambda_+^2} < \Delta < \lambda_+, \quad (2.21)$$

where we have written $n_\infty \propto \Delta^{-3}$, with Δ the inter-particle distance. For such a dust free plasma, screening of an ion by the surrounding plasma is always a linear problem.

For a dust particle immersed in a plasma, $Z_D \gg 1$. This means that the Coulomb-radius can be much bigger than the average distance between the ions, so that there are always some ions inside the volume where the screening is non-linear. This happens when

$$\rho_0 > \Delta \leftrightarrow |Z_D| > \frac{\lambda_+^2}{\Delta^2}. \quad (2.22)$$

It is of course also possible that the region of non-linearity extends *beyond the Debye length*. In that case, the screening by *all* the ions will be non-linear. This happens when

$$\rho_0 > \lambda_+ \leftrightarrow |Z_D| > \frac{\lambda_+^3}{\Delta^3}. \quad (2.23)$$

Equation (2.22) is fulfilled for $|Z_D| \gtrsim 75$, whereas equation (2.23) is fulfilled for $|Z_D| \gtrsim 620$ for the plasma parameters mentioned. Figure 2.4 illustrates this.

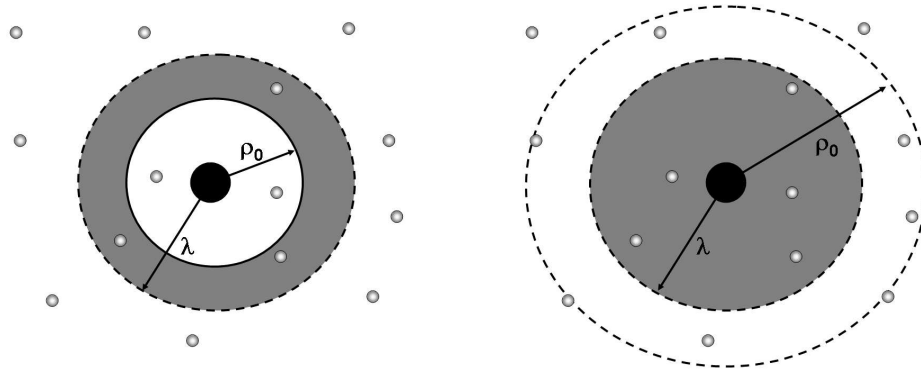


Figure 2.4: **Left:** The Coulomb radius is smaller than the screening length, but is bigger than the average distance between ions, so that some of the ions screening the dust particle are in the non-linear regime.

Right: The Coulomb radius is bigger than both the average distance between the ions, *as well as* the screening length. This means that all the ions that are screening the dust particle are in the non-linear regime, resulting in a larger scattering cross section.

Micrometer sized dust particles can carry several thousands of electron charges. This means that the screening of these particles by ions at room temperature (which is important in the bulk of the discharge, away from the sheaths), is a strongly non-linear problem. A description of this problem in fluid calculations of a dusty plasma is presented in chapter 5 in which a central role will be played by the ratio of the Coulomb radius over the Debye length,

$$\beta(v) = \frac{\rho_0(v)}{\lambda_D(v)}. \quad (2.24)$$

2.2.4 Particle charging

In the above discussion of the screening of dust particles, the surface charge was assumed to be known. In typical laboratory dusty plasmas, collection of charged plasma particles by the dust particles is the dominant charging process. Because of the low mass of the electrons with respect to the ions, the dust surface charge becomes negative, unless there are other important charging processes. The basic classical charging theory follows the trajectories of particles in the potential around the dust particle. This theory is called *Orbital Motion Limited* theory.

Orbital Motion Limited theory (OML)

The ion-collection cross section of a negatively charged dust particle will be bigger than the geometrical surface, since the ions are attracted by the particle. Consider an ion which passes at the dust particle surface with zero radial velocity, as shown in figure 2.5 (it either "just passes", or is "exactly captured").

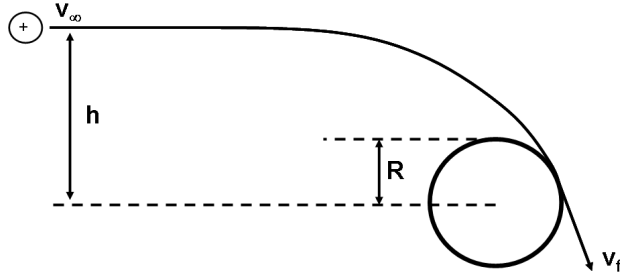


Figure 2.5: An ion comes with velocity v_∞ from the plasma with impact parameter h and is attracted by a negatively charged dust particle with radius R . When it passes the dust particle exactly at the surface, it has velocity v_f , which is tangential to this surface.

Assuming that the potential energy of the particle far away is zero, energy conservation says,

$$E = \frac{1}{2}m_+v_\infty^2 = \frac{1}{2}m_+v_f^2 + e\phi_D, \quad (2.25)$$

where ϕ_D is the dust particle surface potential. At the same time, conservation of angular momentum results in,

$$L_\infty = m_+v_\infty h = L_f = m_+v_f R. \quad (2.26)$$

Solving for v_f from equation 2.26, and substituting in equation 2.25, gives the impact parameter h ,

$$h = R\sqrt{1 - \frac{e\phi_D}{E}}, \quad (2.27)$$

This corresponds to an initial angular momentum of

$$L_\infty = L_{max} = m_+v_\infty h = m_+v_\infty R\sqrt{1 - \frac{e\phi_D}{E}}, \quad (2.28)$$

where we have labelled it as L_{max} , since we assume that any ion approaching with more angular momentum will miss the dust particle, whereas any ion with less or equal angular momentum will be collected.

This way, the ion current contribution is given by [6]:

$$dI = -ef(v)u(r)d^3v \quad L \leq L_{max}. \quad (2.29)$$

Integrating over the sphere and over velocity space, gives for the total collected ion current,

$$I_+ = 4\pi r^2 \int_{L \leq L_{max}} ef(v)u(r)d^3v. \quad (2.30)$$

$f(v)$ is the ion velocity distribution function, and $u(r)$ is the radial velocity at position $r > R$, positive being radially outwards. Assuming that the ion distribution is a Maxwellian², but using the mean energy, rather than the thermal energy, and using equation 2.25, and 2.26 to find

$u(r) = \sqrt{2(E - eV(r))/m_+ - L^2(r)/m_+^2}r^2$, and changing variables, we find for the ion collection current:

$$I_+ = 4\pi R^2 en_\infty \sqrt{\frac{E_s}{2m_+}} \left(1 - \frac{e\phi_D}{E_s}\right) \approx 4\pi R^2 en_\infty \sqrt{\frac{E_s}{2m_+}} \frac{e|\phi_D|}{E_s}, \quad (2.31)$$

where n_∞ is the ion density far away from the dust particle.

The derivation for the electron current is much more straight-forward [7]. Simply assuming that the density of electrons in the repelling potential around the dust particle is given by the Boltzmann distribution, and integrating over velocity space, we find for the electron current, assuming quasi-neutrality far away from the dust particle,

$$I_e = -4\pi R^2 en_\infty \exp\left(\frac{-e|\phi_D|}{k_B T_e}\right) \sqrt{\frac{k_B T_e}{2\pi m_e}}. \quad (2.32)$$

In case of a positively charged particle, the role of the ions and electrons is reversed, in the sense that in that case the ion current has the Boltzmann factor, and the electron current the linear term, with opposite sign.

In equilibrium, the electron and ion current to the dust particle will be equal. This means that the dust particle surface potential can be found from

$$-\exp\left(\frac{e\phi_D}{k_B T_e}\right) \sqrt{\frac{k_B T_e}{2\pi m_e}} + \sqrt{\frac{E_s}{2m_+}} \left(1 - \frac{e\phi_D}{E_s}\right) = 0. \quad (2.33)$$

Defining the effective dust particle potential $\Psi_D = -e\phi_D/k_B T_e$ and $z = k_B T_e/E_s$, $\alpha = m_+/m_e$, we can rewrite the above as

$$^2 f(\mathbf{v})d^3v = n_+ \left(\frac{m_+}{2\pi k_B T_+}\right)^{3/2} \exp\left(\frac{-m_+ \mathbf{v}^2}{2k_B T_+}\right) d^3v$$

$$\exp(\Psi_D) - \sqrt{\frac{\pi}{z\alpha}}(1 - z\Psi_D) = 0, \quad (2.34)$$

which can be solved numerically for different values of z and m_+ . For argon ions at room temperature, probe theory gives an approximate value for the effective floating potential with respect to the plasma potential of $\Psi_D = \Psi_f \approx -5$ [8].

The charge carried by the dust particle $Q_D = 4\pi R^2\sigma$, with σ the surface charge density, which is given by $\sigma = -\epsilon_0\nabla(V)_{r=R}$, is then found by filling in the screened Coulomb potential of equation 2.17, which gives

$$Q_D = 4\pi\epsilon_0 R \left(1 + \frac{R}{\lambda_D}\right) \Psi_D \frac{k_B T_e}{e}. \quad (2.35)$$

Usually, the linearized Debye length is much larger than the particle radius (which is a requirement for the validity of the derived OML currents). Thus, the above becomes for a dust particle in argon plasma,

$$Q_D = 4\pi\epsilon_0 R \Psi_D \frac{k_B T_e}{e} \approx -\frac{20\pi\epsilon_0 k_B T_e}{e} R. \quad (2.36)$$

Therefore, at given electron temperature, the dust charge is a linear function of the particle radius only.

Ion-neutral collisions

The above OML derivation of the dust charge does not include ion-neutral collisions, in which energy and angular momentum might be lost by the ion, i.e. charge-exchange collisions. Suppose now that an ion, which originally has too much angular momentum to be captured, collides with a neutral atom and loses angular momentum. It is then possible that the ion *does* enter the solid angle for capture by the dust particle. This means that charge-exchange collisions can increase the ion collection current. This is true as long as the ions can not gain energy and angular momentum in collisions with neutrals. We assume here that the ions thermalize rapidly in these collisions, so that they are in thermal equilibrium with the neutrals, ruling out hot neutral populations.

In [9], an approximation was derived for the extra ion flux due to these collisions. It was stated that any ion having a charge-exchange collision closer to the particle than the radius for which its thermal energy equals the potential at that radius, dubbed r_T , will eventually be captured by the dust particle. For small β (equation 2.24), r_T exactly equals the Coulomb-radius, ρ_0 , whereas for intermediate values, $\beta \sim 1$, it is equal to λ_D . The probability that such a collision will happen scales approximately as the ratio of r_T over the average mean-free path of

the ions, l_{mfp} . The extra flux of ions to the dust particle due to the collisions is then given by,

$$F_{coll} = \left(\frac{r_T}{R}\right)^2 \frac{r_T}{l_{mfp}} F_{th}, \quad (2.37)$$

where F_{th} is the thermal flux of ions in the ambient plasma. In [10] an expression was derived for the total ion current for $0.1 \lesssim \beta \lesssim 10$, (which are values important for the discharges modelled, as shown both in our simulations in chapter 5 as well as in experiments [11]) which is written as

$$I_{+,tot} = -4\pi R^2 e n_+ \sqrt{\frac{E_s}{2m_+}} z \Psi_D \left(1 - 0.1 z \Psi_D \frac{\lambda_D}{l_{mfp}}\right). \quad (2.38)$$

It is important that even though λ_D/l_{mfp} might not be very large, $z\Psi_D$ can be, so that the charge-exchange collisions are still important for the dust particle charging.

Electron depletion and the Havnes parameter

Another important effect not yet considered is strong electron depletion by the dust. When the dust density is high, many electrons are lost from the plasma volume. This can lead to a situation where the dust charge becomes much less negative than predicted by the OML currents. We can show this by starting at equation 2.33, but in stead of assuming simple quasi-neutrality, we use the complete form of the quasi neutrality equation, $n_e - n_+ + Z_D n_D = 0$ to substitute for n_+ . Defining the *Havnes parameter* [12], $P = n_D Z_D / n_e$, this leads to,

$$\exp(\Psi_D) - \sqrt{\frac{\pi}{z\alpha}} (1 + P) (1 - z\Psi_D) = 0. \quad (2.39)$$

We see that for increasing P , which means for increasing depletion of free electrons from the plasma, the positive contribution to the charging becomes larger, leading to a reduction of the number of electrons carried by the dust. Figure 2.6 also shows this. In chapter 7 this also plays a role.

Charging time

When a dust particle is introduced to the plasma, the electrons will be able to reach the dust particle first, due to their high mobility. After some time, the dust particle becomes negatively charged, repels electrons and attract ions. This means that the final dust equilibrium is determined by the *ions* and not the electrons. An estimate for the final charging time can then be found from

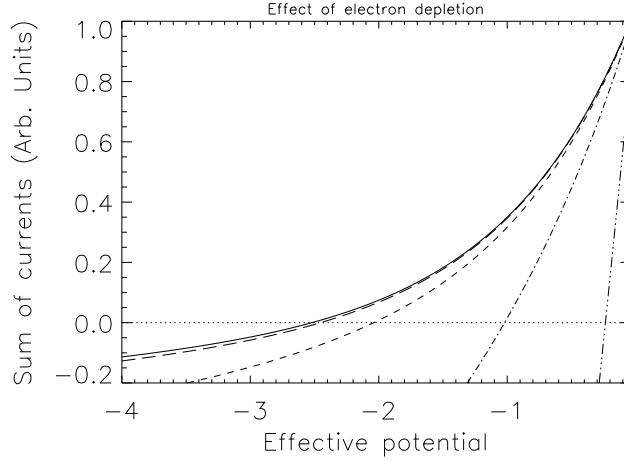


Figure 2.6: The sum of the currents of equation 2.39, for argon with $z = 120$. When it equals 0, the effective dust particle potential, Ψ_D , equals the floating potential. The different lines correspond to, solid line: $P = 0$ (no electron depletion), dashed line: $P = 0.1$, short dashed line: $P = 1$ (just above typical electron depletion), dot-dash line: $P = 10$ (very high electron depletion), dot-dot-dot-dash line: $P = 100$. We see that the dust charge without depletion (solid black line) is closer to $\Psi_D \sim -3$ (-2.6) than $\Psi_D \sim -5$.

$$\frac{dQ_D}{dt} = 4\pi R^2 n_+ e \sqrt{\frac{E_s}{2m_+}} \left(1 - \frac{e\phi_D}{E_s} \right), \quad (2.40)$$

Inserting a solution of the form $Q_D(t) = C_1 \exp(-t/\tau_{ch}) + C_2$, representing a charging curve of a capacitor, with τ_{ch} the "RC-time", which is the time needed to charge a capacitor through a resistor in a RC-circuit, we find,

$$-\frac{1}{\tau_{ch}} C_1 \exp\left(\frac{-t}{\tau_{ch}}\right) = 4\pi R^2 n_+ e \sqrt{\frac{E_s}{2m_+}} \left(1 - \frac{e(C_1 \exp(\frac{-t}{\tau_{ch}}) + C_2)}{4\pi\epsilon_0 R E_s} \right). \quad (2.41)$$

For the limit $t \rightarrow \infty$, we must have $C_2 = 4\pi\epsilon_0 R E_s / e$. Filling this in, results in the solution for the charging time τ_{ch} ;

$$\tau_{ch} = \frac{\epsilon_0 E_s}{e^2 R n_+ \sqrt{\frac{E_s}{2m_+}}}. \quad (2.42)$$

For an one micron radius dust particle in an argon plasma at room temperature with negligible ion drift and typical densities of $n_+ \sim 10^{15} \text{ m}^{-3}$, charging times

are in the order of $10^{-6} \text{ s} < \tau_{ch} < 10^{-5} \text{ s}$. This means that for our simulations $\tau_{RF} = 1/\nu_{RF} < \tau_{ch} < \tau_D$, with τ_D a typical dust time scale, which can be the inverse dust plasma frequency, $\tau_D = 2\pi/\omega_{p,D} = 2\pi(\sqrt{n_D Q_D^2/m_D \epsilon_0})^{-1}$. In the quasi-neutral bulk, the dust charge can be assumed to be constant during a RF-cycle, whereas for the movement of the dust, we can assume it is adjusted instantaneously. In the sheaths however, during part of the RF-cycle, the electrons are swept away by the time varying electric field. This means that ions temporarily are able to reduce the negative charge. This is further shown in [13].

Charging mechanisms

Up to now, only charging by collection of plasma has been considered. Of course, different mechanisms of (de-)charging are possible. We will discuss the different charging mechanisms in dusty plasma and show whether or not they are of importance for this thesis. An extended discussion of the different charging mechanisms in (astrophysical) dusty plasma can be found in [14]. The different charging mechanisms include:

- **Field emission.** Charged particles can be emitted from a surface when the local electric field is high enough. Assume we have a spherical particle with radius R and a surface charge density σ (C m^{-2}). The electric field at the surface is then given by $E = \sigma/\epsilon_0$, and the electrostatic pressure on the surface charges is given by $P = \epsilon_0 E^2/2$, which acts outwards, against the forces binding the charges onto the surface.

Suppose we now want to lift this charged surface away from the particle. The work required to do so is $\Delta U = P \cdot \Delta V$, with ΔV the change in volume. This is roughly given by $4\pi R^2 \cdot \Delta r$. Typical binding energies of band electrons in metals, or electrons on carbon nanotubes is in the range of (1-6) eV. If we then lift the charged surface over roughly an inter-atomic distance ($\Delta r \sim 10^{-10} \text{ m}$), and require that the work done by the electrostatic pressure has to exceed typical binding energies, we can solve for the required electric field; $P \cdot 4\pi R^2 \Delta r > (1 - 6) \text{ eV}$; $\epsilon_0 E^2 2\pi R^2 \Delta r > (1 - 6) \text{ eV}$; $E > 5.4\sqrt{(1 - 6)} R^{-1} \text{ V m}^{-1}$. For a $1 \mu\text{m}$ particle, we then find a required electric field at the surface of $E \approx 9 \text{ V } \mu\text{m}^{-1}$. Surprisingly, this corresponds to only 6500 electron charges.

Of course, no quantum mechanical effects were taken into account, and the above derivation underestimates the observed electric fields. In multiwall carbon nanotube field emitters used in novel field emission displays, the electric field at the surface is roughly $20 \text{ V } \mu\text{m}^{-1}$ [15]. For metal tip field emitters, such as used in field emission microscopes, it can be as large as $1\text{-}10 \text{ V nm}^{-1}$ [16].

Such strong fields then require sharp points or edges, which locally enhance the macroscopic field. However, in this thesis we only present results of particles which are assumed to be perfectly spherical, so that field emission plays no role. In many experiments, specially fabricated dust particles are used, which are spherical, or have other pre-defined shapes, but are typically very smooth. In-situ grown particles can have a different shape, for instance fractal-like. In that case, field emission might play an important role, also for smaller particles. It results in a reduction of the number of electrons carried by the dust.

- **Photo-detachment.** When photons with energies above the work function interact with the dust, electrons can be removed through the effect of photo-detachment. Many plasmas in space are exposed to intense ultraviolet radiation, for instance plasmas around young stars, as discussed in chapter 1 and also the dusty plasma in the ionosphere. In fusion reactors there can also be significant UV fluxes [17]. Plasma itself can also emit UV radiation, even though the intensity is relatively weak, however, commercially available UV sources are abundant, which could provide an interesting tool to control dust charge in laboratory dusty plasmas. This is investigated in chapter 7.
- **Radio-active emission.** When dust particles consist of radio-active material, electrons (via β -decay) or α particles can be emitted. Depending on the material, this can result in either more positive dust, or more negative dust. In this thesis we do not consider radio-active dust, but in fusion plasmas, carbon dust can absorb tritium from the plasma, which is radio-active and decays emitting an electron. In space, radio-activity might also play an important role.
- **Thermionic emission.** When dust particles are heated, for instance by recombination of the collected charged plasma particles, the electrons and ions collected on the surface gain thermal energy. When this energy becomes larger than the binding energy, the collected particles can be emitted into the plasma [18, 19]. For negatively charged particles this is most likely for the electrons, due to the repelling potential. In [20] it was shown that the particle heating in typical experiments modelled in this thesis is very small. Therefore, we do not include it here.
- **Tribo-electric emission.** When two particles come in contact, surface friction can transport electrons from one to the other. In this thesis, dust particles carry a significant amount of charge. Due the repulsive force between

them, they are always well separated. Nanometer sized particles carry only few charges, which means they are more likely to come in contact.

- **Secondary electron emission by electrons or ions.** When electrons and ions are accelerated to large energies, they might release electrons from the surface when they collide with the dust. For secondary electron emission to become effective, high impact energies are required ($\gtrsim 50eV$), which are not present in large quantities, as calculations in chapter 7 will show. Therefore, we do not include this effect here.

2.3 Forces acting on dust particles

Charged particles in plasma experience several forces and settle in equilibrium positions according to the way these forces act. The first and most obvious force is that of gravity. Dust particles in the micrometer range are in general massive enough to experience a significant gravitational force.

Since electric fields are present in plasma, charged objects are accelerated in these fields. Furthermore, they capture and deflect charged plasma particles. Especially ions are heavy enough to transfer a significant amount of momentum to the dust, which results in the so called ion drag force. This force depends on the dust charge, but also on charge-exchange collisions, the non-linearity of the screening of the dust by the plasma, and on the ion flow speed.

Due to the low ionization degree, dust-neutral collisions are abundant. This means that dust particles moving through a discharge experience a neutral drag force. Since the neutral atoms can be heated by collisions with ions, there is a difference in the amount of momentum transferred to the dust on the side of the dust particle facing a hotter neutral gas volume, than on the side facing a colder volume. This results in a net force called the thermophoretic force.

Finally, the screened charged particles interact with each other through the screened Coulomb potential, once they get close enough to each other. This interaction is an important source of internal pressure and plays a role in the diffusion of charged dust.

We will give the mathematical forms of these forces and illustrate their importance by calculating their magnitudes for dust particles with a radius of 2 micrometer and a mass density of 2000 kg m^{-3} in typical plasma parameters.

2.3.1 Electrostatic force

The highly charged dust particles interact with electric fields due to space charges, or due to externally applied electric fields. They will be accelerated in the time-

averaged electric field $\bar{\mathbf{E}}$, and the corresponding force is given by [21]

$$\mathbf{F}_{\bar{E}} = Q_D \bar{\mathbf{E}} \left(1 + \frac{(R/\lambda_D)^2}{3(1 + (R/\lambda_D))} \right). \quad (2.43)$$

The term between brackets is due to the polarization of the dust charge by the plasma around the dust particle, which causes a dipole term to arise. (Higher order terms are neglected.) For $R \ll \lambda_D$, the usual form for the electrostatic acceleration is found, which is used from here on,

$$\mathbf{F}_{\bar{E}} = Q_D \bar{\mathbf{E}}. \quad (2.44)$$

Since $Q_D \propto R$, we see that this force scales linearly with R . For a particle with a 2 micrometer radius, the typical charge in the quasi-neutral bulk of the discharges modelled in this thesis is approximately $Z_D \leq 10^4 e$, whereas the electric field in the bulk is approximately $\bar{E} \sim 10^2 \text{ V m}^{-1}$. This gives an electrostatic force of $F_{\bar{E}} \sim 1.6 \cdot 10^{-13} \text{ N}$. In the sheath region in front of the electrodes the dust charge is smaller, $Z_D \sim 10^3 e$, but the electric field is much higher, $\bar{E} \sim 10^4 \text{ V m}^{-1}$. This gives a force of $F_{\bar{E}} \sim 1.6 \cdot 10^{-12} \text{ N}$.

2.3.2 Gravity

On Earth, particles are accelerated by the force of gravity, which has an average value of $\mathbf{g} = -g \hat{\mathbf{z}} = -9,81 \text{ m s}^{-2} \hat{\mathbf{z}}$. For a dust particle with mass density ρ , this force is given by

$$\mathbf{F}_g = \frac{4\pi\rho R^3}{3} \mathbf{g}. \quad (2.45)$$

This force scales with the volume of the particle, $F_g \propto R^3$. For nanometer sized particles in typical laboratory discharges it is therefore an unimportant force, while for micrometer sized particles it is an important force, playing a dominant role in the spatial ordering and equilibrium positions of the particles in the plasma.

For our test particle we find a gravitational force of $F_g = 6.6 \cdot 10^{-13} \text{ N}$. We see that the force of gravity can not be balanced by the electric field in the bulk of the discharge, but only in the sheath regions in front of the electrodes. In order to study the full three dimensional structure and dynamics of dusty plasma of micrometer sized particles, micro-gravity experiments are required.

2.3.3 Ion drag force

The ion drag comes from the interaction between ions and charged dust particles. Ions are both collected and scattered, and transfer momentum to the dust. In

general form it can be described as [22],

$$\mathbf{F}_{ion} = m_+ \int \mathbf{v} v f_+(\mathbf{v}) [\sigma_c(v) + \sigma_s(v)] d\mathbf{v}. \quad (2.46)$$

with \mathbf{v} the ion velocity, $v = |\mathbf{v}|$, $f_+(\mathbf{v})$ the ion velocity distribution function, $\sigma_c(v)$ and $\sigma_s(v)$ the ion collection momentum transfer and ion scattering momentum transfer cross-section. The collection cross section was already derived in the section on dust particle charging, so that we simply have from equation 2.27, $\sigma_c = \pi b_c^2 = \pi R^2 (1 - e\phi_D/E_s)$.

The derivation of the scattering cross section is as yet an unsolved problem for all possible values of the ion flow speed. Furthermore, the non-linear screening of dust particles in plasma is important for ion-dust interaction, as well as the presence of ion-neutral collisions, similar to the problem of dust charging. The original approach [5] assumes only linear scattering of ions very close to the dust particle, which is called *small angle scattering*³.

Small angle scattering

The general form of the scattering cross section for ions approaching very close to the dust particle, so that they move through the unscreened Coulomb potential, is given by [22],

$$\sigma_s(v) = 4\pi \int_{\rho_{min}}^{\rho_{max}} \frac{\rho d\rho}{1 + (\rho/\rho_0(v))^2}, \quad (2.47)$$

where the integration is over all the scattering impact parameters ρ between the minimum impact parameter for capture, $\rho_{min} = b_c$, as given above, and the maximum scattering impact parameter ρ_{max} , which is yet to be determined. $\rho_0(v)$ is the Coulomb radius for arbitrary ion velocity v , so that $\lim_{v \downarrow v_T} \rho_0(v)$ is ρ_0 as defined in equation 2.19. The solution to the above equation is given by $\sigma_s(v) = 4\pi\rho_0^2(v)\Lambda(v)$, with $\Lambda(v)$ the Coulomb logarithm,

$$\Lambda(v) = \ln \left[\frac{\rho_0^2(v) + \rho_{max}^2(v)}{\rho_0^2(v) + b_c^2(v)} \right]^{1/2}. \quad (2.48)$$

In the small angle solution, it is then assumed that the maximum scattering impact parameter is given by the Debye length, $\rho_{max} = \lambda_D$, so that the scattering cross-section becomes,

³In a way this is an interesting name, since usually *small angle scattering* refers to scattering of projectiles in orbits far away from the scattering target, over tiny deflection angles, like in X-ray scattering. Here it means that ion scattering takes place well outside the radius where $eV_D/k_B T_+ > 1$, but not necessarily over "small angles".

$$\sigma_s(v) = 4\pi\rho_0^2(v) \ln \left[\frac{\rho_0^2(v) + \lambda_D^2}{\rho_0^2(v) + b_c^2(v)} \right]^{1/2}. \quad (2.49)$$

This can be rewritten, using $\beta(v) = \rho_0(v)/\lambda_D$, to

$$\sigma_s(v) = 2\pi\rho_0^2(v) \ln \left[\frac{1 + \beta^2(v)}{\beta^2(v) + b_c^2(v)/\lambda_D^2} \right]. \quad (2.50)$$

This form implies that the ions scattered with impact parameters larger than the Debye length do not transfer a significant amount of momentum to the dust, which is only true for very small values of $\beta(v)$. This is typically not so for dust grains in a plasma, as was shown in section 2.2.3. Therefore, the effect of scattering over large angles needs to be taken into account.

Large angle scattering

Taking interactions beyond the Debye length into account, one needs to redefine the maximum impact parameter ρ_{max} . The cut-off condition in terms of the distance of closest approach for an ion, r_0 , becomes $r_0(\rho_{max}(v)) = \lambda_D$. By analogy, in [13], the maximum impact parameter corresponds to an ion grazing an imaginary sphere with radius λ_D . Similar to the OML collection radius, we then find $\rho_{max}(v)$ as,

$$\rho_{max}(v) = \lambda_D \sqrt{1 - \frac{e\phi(r = \lambda_D)}{E_s}} = \lambda_D \sqrt{1 + 2\beta(v)}. \quad (2.51)$$

Any ion approaching the dust with energy $E_s = mv_+^2/2$ with an impact parameter less than or equal to $\rho_{max}(v)$ then contributes to the scattering momentum transfer. Using this in equation 2.48, we have

$$\Lambda(v) = \frac{1}{2} \ln \left[\frac{\rho_0^2(v) + \lambda_D^2 + 2\lambda_D\rho_0(v)}{\rho_0^2(v) + R^2 + 2R\rho_0(v)} \right] = \ln \left[\frac{1 + \beta(v)}{\beta(v) + R/\lambda_D} \right]. \quad (2.52)$$

This then is used to calculate the scattering cross-section taking non-linear scattering of ions beyond the Debye length into account, but still by assuming an unscreened Coulomb potential. The above form is valid for $\beta(v) \lesssim 5$, and therefore only covers moderate non-linearity. For the case of collection and moderate non-linear scattering of ions, we thus find an ion drag equal to,

$$\mathbf{F}_{ion} = m_+\pi R^2 \int \mathbf{v} v f_+(\mathbf{v}) \left[\left(1 + 2\frac{\rho_0}{R}\right) + \frac{4\rho_0^2}{R^2} \ln \left(\frac{1 + \beta}{\beta + R/\lambda_D} \right) \right] d\mathbf{v} \quad (2.53)$$

where ρ_0 , λ_D , and β depend on v .

A typical form used for the ion distribution function, $f_+(\mathbf{v})$, is a so called shifted Maxwellian distribution. After integrating the above with this distribution, a simple analytical form of the scattering ion drag force is obtained in the limit $u_+ < v_T$. To allow for a larger range of drift velocities, the mean velocity, v_+ is used, as defined in section 2.2.3. The differences in the results with the complete solution to the integral [23] are small for the discharges under consideration, as is also mentioned in chapter 3. Since our approach is computationally more robust and straightforward, we use the analytical form. This way, we find for the ion drag force,

$$\mathbf{F}_{ion} = n_+ m_+ v \mathbf{u}_+ \left[\pi R^2 \left(1 + \frac{2\rho_0}{R} \right) + 4\pi\rho_0^2 \ln \left(\frac{1 + \beta(v)}{\beta(v) + R/\lambda_D} \right) \right], \quad (2.54)$$

for moderate non-linear scattering. Depending on the mean free path, as well as on the particle potential, ion-neutral collisions can play an important role in the momentum transfer, similar to the way these collisions change the dust charging.

Ion-Neutral collisions

In [24, 25], the appropriate form of the collision operator was derived for sub-thermal ion flow, with $x = \lambda_D/l_{mfp}$ as,

$$\mathcal{K}(x) = x \arctan(x) + (\sqrt{\pi/2} - 1)(x^2/(1+x^2)) - \sqrt{\pi/2} \ln(1+x^2),$$

so that the ion drag including ion-neutral collisions, and moderate non-linearity, is given by

$$\mathbf{F}_{ion} = n_+ m_+ v \mathbf{u}_+ \times \left(\pi R^2 \left(1 + \frac{2\rho_0}{R} \right) + \pi\rho_0^2 \left[4 \ln \left(\frac{1 + \beta(v)}{\beta(v) + R/\lambda_D} \right) + \mathcal{K} \left(\frac{\lambda_D}{l_{mfp}} \right) \right] \right). \quad (2.55)$$

Ion flow

In order to take the screening anisotropy caused by ion flow into account, an analytical approach has been derived in a recent Particle-In-Cell approach [26]. The mean ion energy as used in the calculation of the Coulomb logarithm, has to be changed according to,

$$\begin{aligned}
\frac{1}{2}m_+v_+^2 &= \frac{4k_B T_+}{\pi} + \frac{1}{2}m_+u_+^2 \\
&\quad \updownarrow \\
\frac{1}{2}m_+\tilde{v}_+^2 &= \frac{4k_B T_+}{\pi} + \frac{1}{2}m_+u_+^2 \left[1 + \left(\frac{u_+}{u_B} / (0.5 + 0.05 \ln \left(\frac{m_+}{Z_+} \right) + \sqrt{\frac{T_+}{T_e}}) \right)^3 \right].
\end{aligned} \tag{2.56}$$

$u_B = \sqrt{k_B T_e / m_+}$ is the Bohm velocity, and $m_+ / Z_+ = 40$ for argon. It was shown [26], that this form becomes significant when $u_+ \geq 0.55u_B$. This way, the final form of the ion drag, including ion-neutral collisions, moderate non-linearity, and significant ion flow becomes,

$$\begin{aligned}
\mathbf{F}_{ion} &= n_+ m_+ v \mathbf{u}_+ \times \\
&\quad \left(\pi R^2 \left(1 + \frac{2\rho_0}{R} \right) + \pi \rho_0^2 \left[4 \ln \left(\frac{1 + \beta(\tilde{v})}{\beta(\tilde{v}) + R / \lambda_D(\tilde{v})} \right) + \mathcal{K} \left(\frac{\lambda_D}{l_{mfp}} \right) \right] \right).
\end{aligned} \tag{2.57}$$

For supersonic ion flow, $\beta(\tilde{v}) \downarrow 0$, so that the small angle scattering approach is valid, but with the electron Debye length as the screening length, which follows automatically from the definition of the linearized Debye length, for $M_T \gg 1$.

According to [23] the effect of finite grain size is important when $\beta(v) \lesssim R / \lambda_D \ll 1$, which happens when $M_T \gtrsim \sqrt{z\chi}$. Here $\chi = e |\Psi_D|$, the dimensionless grain charge, and $z = T_e / T_i$. Since $z\chi \gtrsim 100$, we have the effect of finite grain size for $M_T \gtrsim 10$, in which case the Coulomb logarithm becomes $\Lambda \approx \ln(\lambda_D / R)$. The collection force becomes more important than the scattering force for large ion flow in the sheaths. This happens when $M_T \gtrsim \sqrt{z\chi} / 8 \ln(\lambda_e / R)$, which is about $M_T \gtrsim 20$. In typical discharges modelled here, most of the bulk of the discharges is sub-thermal and shows moderate non-linearity. Near the sheaths, the ion flow quickly rises up to the point where collection dominates. Therefore, the above form used for the ion drag force is suitable for our calculations.

Taking ions streaming with $M_T = 1$, temperature $T_+ = 293K$, and assuming that the density of interacting ions is the same as the ions in the unperturbed plasma $n_+ \approx n_{+, \infty}$, the magnitude of the ion drag force for $\beta \sim 5$ is $F_{ion} \sim 800\sqrt{2} \ln(1.2) m_+ v_T^2 \epsilon_0 k_B T_+ / e^2 \sim 1.7 \cdot 10^{-12}$ N. We see that $F_{ion} \approx F_{\bar{E}}$.

2.3.4 Neutral drag force

The ionization fraction in typical experiments is very low. Therefore, the most important constituent of the plasmas in such experiments will simply be the neutral gas. Dust particles moving through the background gas will experience many

collisions with neutral particles, resulting in a friction force. This friction force is called the neutral drag force. The original derivation of the force acting on spheres moving through a flowing background is given in [27].

For a dust particle velocity relative to the background, \mathbf{V} , spherical particles with radius R , moving through the background of density n_n , mass m_n , with an average velocity $v_T = \sqrt{8k_B T_{gas}/\pi m_n}$, the neutral drag force is given by:

$$\mathbf{F}_{nd} = -\frac{4}{3}\pi R^2 n_n m_n v_T \mathbf{V}. \quad (2.58)$$

This equation is correct for specular reflection of neutral particles colliding with the dust. This force is proportional to the square of R .

For argon plasma ($m_{ar} = 40 m_p$) at room temperature $T = 293K$, at typical pressures between 100 and 300 mTorr (13 and 40 Pa), we find a neutral drag force $1.42 \cdot 10^{-12} V \leq F_{nd} \leq 4.35 \cdot 10^{-12} V$ N. Typical relative dust flow speeds will turn out to be in the range of cm s^{-1} , or even mm s^{-1} . This gives a neutral drag force in the range of $F_{nd} \sim 10^{-15} - 10^{-14}$ N. This force is small compared to gravity and the electrostatic force. It plays an important role in the time needed for dust to reach equilibrium positions when introduced into the plasma, but also damps waves moving through a dust cloud, or oscillations of dust particles. For a completely dynamic calculation of the dust transport one would therefore have to include the $\partial_t + \mathbf{v} \cdot \nabla \mathbf{v}$ term in the dust transport, but this is beyond the aim of this thesis, where the calculations are based on the equilibrium solution.

2.3.5 Thermophoretic force

Ions collide with neutral atoms and locally heat the neutral background gas. This leads to temperature gradients. A further source of gas heating could be heating by the walls. When neutral atoms are scattered off the walls, which are at a higher temperature, they could come off the wall with a higher temperature themselves. Ions and electrons recombining, can also result in hot neutral atoms [28].

These neutral atoms impinge on dust particles, during which they transfer momentum to the dust. More neutral atoms will hit the side facing the hot part of the gas per second, than on the side facing the colder part of the background gas. Furthermore, hotter atoms will on average transfer more momentum per collision than cold atoms. Therefore, the dust particles will experience a net force against the temperature gradient. This force is called thermophoresis, and can be calculated as,

$$\mathbf{F}_{th} = -\frac{32 R^2}{15 v_T} \kappa_T \nabla T_n, \quad (2.59)$$

where κ_T is the thermal conductivity coefficient for Argon gas, which at 300 K has a value of $0.01772 \text{ W K}^{-1} \text{ m}^{-1}$. This force is again proportional to the square of R .

In [20] it was found that typical temperature gradients in the PKE (Plasma Kristall Experiment) chamber are in the range of 100 K m^{-1} . This results in a thermophoretic force of $F_{th} \sim 9.6 \cdot 10^{-15} \text{ N}$. Like the neutral drag force, thermophoresis plays only a minor role for micrometer sized dust particles in the discharges modelled in this thesis. Sometimes heated electrodes are used to create a temperature gradient in discharges, large enough to balance the force of gravity. This allows the study of three-dimensional dust structures, without the need for micro-gravity environments [29], but requires large experimental efforts to reduce inhomogeneities in the temperature profile.

2.3.6 Mutual Coulomb interaction

One can imagine that a dust cloud consisting of highly charged particles at large densities is much harder to compress or deform than a cloud consisting of particles with a low charge at low densities. A measure for this is given by the *coupling parameter*, $\Gamma = E_{Coul}/E_{th} = (Q_D^2 \exp(-\Delta/\lambda_D)/4\pi\epsilon_0\Delta)/(k_B T_D)$, where we have defined the thermal energy as $E_{th} = k_B T_D$ and $\Delta \approx n_D^{-1/3}$ is the average inter-particle distance.

When $\Gamma \gg 1$, the coupling between the dust particles is very strong and the dust forms an incompressible crystal. The dust pressure for such a crystal was derived in [30] as,

$$P_{c,D} = \frac{1 + \alpha\kappa}{3} N_{nn} \tilde{\Gamma} P_{D,g}, \quad (2.60)$$

with α a geometrical factor, which depends on the type of crystal ordering of the particles. $\alpha = 1.12$ for face centered cubic (fcc) and hexagonal closed packing (hcp) crystals, which both have a number of nearest neighbors, $N_{nn} = 12$. $\tilde{\Gamma}$ is then a "geometrically corrected" coupling parameter, with $\Delta \rightarrow \alpha\Delta$. $P_{D,g} = n_D k_B T_D$ is the simple dust "gas-phase" pressure for $\Gamma \ll 1$, and $\kappa = \Delta/\lambda_D$.

In between $\Gamma \ll 1$ and $\Gamma \gg 1$, we are not aware of any analytical solutions. In [30] a linear interpolation is used, such that $P_D = P_{D,g}(1 - x) + P_{D,c} x$, where $x = (\Gamma - 1)/(\Gamma_c - 1)$, and $\Gamma_c = 106 \exp \kappa/(1 + \kappa + \kappa^2/2)$ is the value of Γ beyond which the dust is assumed to be in a crystalline state.

Using the above pressure equation, we can define the dust diffusion coefficient as,

$$D_D = \frac{dP_D}{dn} \frac{1}{m_D \nu_{m,D}}, \quad (2.61)$$

with $\nu_{m,D} = 4\pi R^2 n_n v_T (m_n/m_D)/3$ the dust-neutral momentum transfer frequency, which has a value in the order of 10^2 s^{-1} , and $v_T = \sqrt{8k_B T_n/\pi m_n}$ the neutral atom thermal velocity [11]. The role of this diffusion is to smoothen out the dust density and act against the compressing action of the ion drag and electrostatic force.

2.3.7 Summary

We have seen that for the transport of micrometer sized particles, the electrostatic force, gravity, and the ion drag are the dominant forces. Thermophoresis is not important for most discharges modelled in this thesis. For smaller particles thermophoresis can be important. Neutral drag mainly determines the time-scale on which an equilibrium position is reached and damps small scale dust dynamics. Finally, the mutual Coulomb interaction sets the diffusion of the dust particles.

2.3.8 Void formation

In experiments in sounding rockets, or on board of the International Space Station [31], gravity no longer plays its dominant role. Therefore, ion drag and the electrostatic force are the most dominant forces. Ionization in the center of the discharge results in ions diffusing outwards in the time averaged electric field, which form a dust free void region. Figure 2.7 shows the difference between a ground-based experiment and an experiment under micro-gravity conditions.

The Coulomb interaction between the charged particles determines the thickness of dust layers, but also the compressibility and diffusion of dust clouds. For the appearance of a dust cloud in the final equilibrium, the ion drag, electrostatic force, and the mutual Coulomb interaction are then the most important forces.

2.4 Simulation models

Except for the results presented in chapter 4, the chapters of this thesis are based on different simulation models. This section describes what our models solve and how they do so. First, we will describe a *fluid model*, which solves time-averaged quantities in two dimensions. Second, we explain how our *Particle-In-Cell model* follows many particles in a one-dimensional dusty argon plasma.

2.4.1 Fluid model

The fluid model [32, 33, 34] solves the particle balance for both the electrons and the ions in two dimensions in a cylindrical geometry. The particle balance for

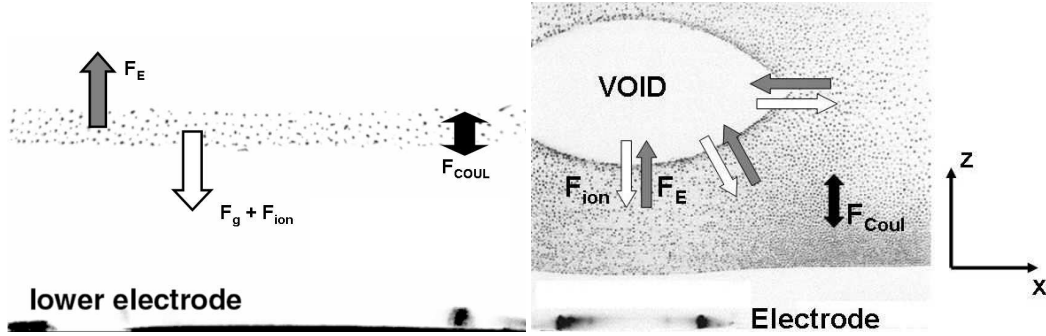


Figure 2.7: **Left:** Side view of a typical dusty plasma experiment in a ground-based laboratory. Gravity dominates and only allows a thin two-dimensional layer in which the sheath electric field acts as the balancing force. The mutual repulsion determines the thickness of the layer.

Right: Without the force of gravity a three-dimensional dust crystal forms. Due to the plasma production in the center, ions diffuse outwards and cause a strong radial ion-drag force, which acts against the electrostatic force. This results in a dust-free void region. The mutual Coulomb repulsion determines the compressibility of the crystal.

species j is written as,

$$\frac{\partial n_j}{\partial t} = -\nabla \cdot \Gamma_j + S_j, \quad (2.62)$$

which is a mathematical translation of the statement that the change in time of the particle density n_j equals the net flux Γ_j of the particles over the boundary of the volume, plus the creation and destruction of the quantity inside the volume, with source terms S_j . As was explained before, only collisions between charged plasma particles and neutrals are considered, due to the low ionization degree.

Assuming a distribution function which is isotropic in the direction perpendicular to the flux [32], the particle flux can be expressed using the so called *drift-diffusion approximation*,

$$\Gamma_j = \mu_j n_j \mathbf{E} - D_j \nabla n_j, \quad (2.63)$$

with μ_j , and D_j the mobility and diffusion coefficients respectively. The electric field is found by solving the Poisson equation, including the dust charge calculated at every grid point using the OML currents, equation 2.31, 2.32, with the calculated plasma quantities as input;

$$\nabla^2 V = \frac{e}{\epsilon_0} (n_e - n_+ + n_D Z_D), \quad (2.64)$$

$$\mathbf{E} = -\nabla V.$$

For the electrons this instantaneous field is used, however, the ions are too heavy to follow the RF field, therefore, an effective field $\mathbf{E}_{eff,+}$ is calculated using the ion-neutral momentum transfer frequency, $\nu_{m,+} = e/\mu_+m_+$,

$$\frac{d\mathbf{E}_{eff,+}}{dt} = \nu_{m,+} (\mathbf{E} - \mathbf{E}_{eff,+}). \quad (2.65)$$

The energy balance is also solved, however, only for the electrons. The ions are assumed to deposit their thermal energy locally in charge-exchange collisions [35]. For the electron energy density w_e , a similar drift-diffusion approximation is used to solve the second moment of the Boltzmann equation,

$$\begin{aligned} \frac{\partial w_e}{\partial t} &= -\nabla \cdot \Gamma_{w_e} + \mathbf{J}_e \cdot \mathbf{E} + S_{w_e}, \\ \Gamma_{w_e} &= -\frac{5}{3}\mu_e w_e \mathbf{E} - \frac{5}{3}D_e \nabla w_e, \end{aligned} \quad (2.66)$$

where the term $\mathbf{J}_e \cdot \mathbf{E}$ is Ohmic heating of the electrons in the electric field. The source terms for energy and particles include electron-impact excitation, ionization, charge-exchange, but of course also recombination of plasma on the dust particles. So both for the electric field, as well as for the source-terms, are the plasma equations coupled to the dust equations.

For the transport of the dust, the electrostatic, ion drag, and thermophoretic force are assumed to be in balance with the neutral drag at every time step of the simulation. This way, we can solve for the dust flux, using a drift-diffusion type of equation,

$$\Gamma_D = \frac{n_D \mathbf{F}_{\bar{E}}}{m_D \nu_{m,D}} - D_D \nabla n_D + \frac{n_D \mathbf{F}_{th}}{m_D \nu_{m,D}} + \frac{n_D \mathbf{F}_{ion}}{m_D \nu_{m,D}}. \quad (2.67)$$

These equations form a closed set. Initially, no dust is introduced and the code is run until a periodic solution for the plasma quantities is found, so that the set of solutions, $U(t)$, obeys $U(t) = U(t + \tau_{RF})$. When this is achieved (the code is said to "converge"), source terms for the dust are added, corresponding to approximately $7.5 \cdot 10^5$ particles per second. The dust transport is then solved using a much larger time step, which is necessary because of the much larger dust mass. This transport creates space charge regions leading to instabilities. To adjust for this, the ion density profile is adapted to maintain quasi-neutrality. When too large a discrepancy between the new and the old solution occurs, the dust is frozen and the plasma equations are solved on the small sub-RF timescale to adapt to the new situation. This is repeated until final equilibrium is reached [34].

Magnetic field

In chapter 3, the above code is used to include the effect of a homogeneous axial magnetic field on the plasma transport, and investigate the effect of this on the formation of a void.

Charged particles gyrate around magnetic field lines, which reduces their mobility and diffusion coefficient perpendicular to the field. The degree to which the charged particles are prevented from crossing the magnetic field lines, is indicated by the Hall parameter; $H_j = \omega_j/\nu_{m,j} (= \mu_j B)$ [36], where $\omega_j = q_j B/m_j$ is the cyclotron frequency and $\nu_{m,j}$ is the momentum transfer frequency. The diffusion across magnetic field lines is strongly reduced (a particle species is magnetized) when $H_j > 1$.

For the ions we find in our argon discharge at 40 Pa background pressure $H_+ = \mu_+(40Pa)B = (133/40) \times 0.145 \times B = 0.48 B$. For the electrons, we find this way $H_e = \mu_e(40Pa)B \sim 100 B$ [32]. For the magnetic fields used in our simulations ($0.01 \leq B \leq 0.5 T$), we see that the ions are never magnetized, whereas the electrons always are. Therefore, we rewrite the mobility and diffusion coefficient for the electrons perpendicular to the magnetic field (thus in the radial direction) as:

$$\mu_{e,\perp} (D_{e,\perp}) \rightarrow \left[1 + \left(\frac{\omega_e}{\nu_{m,e}} \right)^2 \right]^{-1} \times \mu_{e,\perp} (D_{e,\perp}). \quad (2.68)$$

In the center of the discharge, quasi-neutrality and the particle balances result in *ambipolar* conditions that couple the ion flux to the electron flux via the average electric field that is generated. This means that the ion transport is also changed by a change in the electron transport.

2.4.2 Particle-in-Cell plus Monte Carlo

Using a fluid code as described above is useful for finding time and space averaged quantities. Such a code typically requires transport coefficients, while a certain energy distribution function for the electrons is assumed. If one wants to solve plasma at small length- or time-scales, or if one wants to find the energy distribution function (or does not want to assume one), a kinetic approach is necessary, such as the *Particle-In-Cell plus Monte Carlo* approach.

In this kind of modelling, one solves the motion of particles on a grid, solving their trajectories from the electrostatic force, which comes from the charge density the particles form on the grid. It is impossible to compute the motion of the huge amount of particles present in even the smallest plasmas. Therefore, *super-particles* are followed, which represent many real particles. The movement

of these particles is solved in the Particle-In-Cell module, whereas the collisions between charged plasma particles and the background gas, as well as the interaction between charged plasma particles and the dust, is solved in the Monte Carlo module.

In our model of a dusty RF discharge, we assume that the electrodes are parallel and infinite, which allows us to only consider the position of the particles on the central symmetry-axis, z , and the three velocity components v_x, v_y, v_z . Two dust clouds are fixed in position at two grid-point intervals within the discharge, but the dust charge density will vary, due to the collection of plasma by these dust clouds. The general approach is as follows [37]:

1. The charge q_j of every super-particle at position z_j is interpolated to the two nearest grid points.
2. The charge density on the grid ρ_k is calculated. The dust charge density on the grid $\rho_{k,D}$ is added, to find the total charge density on the grid $\rho_{k,tot} = \rho_k + \rho_{k,D}$.
3. The Poisson equation $\nabla_z^2 V_k = -\rho_{k,D}/\epsilon_0$ is solved to find the potential on the grid. The electric field in between the grid points is then found from $E_{k+\frac{1}{2}} = -\frac{V_{k+1}-V_k}{\Delta z}$.
4. The electric field found is then linearly interpolated to the nearest particles, to find the force acting on particle j ; F_j . Using a leapfrog scheme, the new velocity and position $v_{z,j}, z_j$ can then be found. Return to 1.

The above scheme enables us to follow the particles in space and time, but does not model a dusty plasma, since this requires collisions between plasma and neutrals, and between plasma and dust. To calculate this, we need the energy of the particles, which we get in step 4, from $E_j = mv_j^2/2$. From literature, we need the cross-sections for the i different collision processes $\sigma_i(E_j)$.

The average number of particles which experience a collision during a time-step Δt is calculated as follows. First, the total collision cross-section, which is the sum of all the collision cross-sections over the energy range considered in the code, is determined. The ion-neutral cross sections are taken from [38]. The electron collision cross-sections are taken from [39]. Then the corresponding total collision frequency is determined and the maximum is determined *once*,

$\frac{\nu_1(\epsilon_i)}{\nu_{max}}$	$U \leq$	$\frac{\nu_1(\epsilon_i)}{\nu_{max}}$	Collision type 1
$< U \leq$	$\frac{\nu_{max}(\nu_1(\epsilon_i) + \nu_2(\epsilon_i))}{\nu_{max}}$	Collision type 2	
	\vdots		
$\sum_{j=1}^N \frac{\nu_j(\epsilon_i)}{\nu_{max}} < U$			Null collision

Table 2.1: The determination of the type of collision for every particle i from a total of N types of collisions.

$$\sigma_T(\epsilon) = \sigma_1(\epsilon) + \dots + \sigma_N(\epsilon) \quad (2.69)$$

$$\nu_T(\epsilon) = n_{gas} \sigma_T(\epsilon) \sqrt{\frac{2\epsilon}{m}} \quad (2.70)$$

$$\nu_{max} = n_{gas} max_{\epsilon} (\sigma_T(\epsilon) \sqrt{\frac{2\epsilon}{m}}) \quad (2.71)$$

The average fraction of particles experiencing a collision in the discharge within the time interval Δt is then given by,

$$P_{max} = 1 - \exp(-\nu_{max} \Delta t). \quad (2.72)$$

The colliding particles are randomly chosen from the total number of super-particles. For each particle is decided which kind of collision (assuming there are N different types of collisions) it will undergo, using a computer generated random number $U \in [0, 1)$, as shown in table 2.1. The "Null Collision" is an artificial collision, which changes nothing to the particle velocities. It only serves to keep ν_T constant over the whole energy range.

For the collisions with the dust particles a similar approach is followed, but now only between the boundaries of the dust clouds at z_1, z_2 , and z_3, z_4 . The cross-sections are given by [40],

$$\begin{aligned} \sigma_{capt} &= \min \left[\pi R^2 \left(1 \pm \frac{Q_d}{4\pi\epsilon_0 w_{+,e} R} \right), \pi L_{nn}^2 \right], \\ \sigma_{scat} &= \min(\pi \lambda_D^2, \pi L_{nn}^2) - \sigma_{capt}, \\ L_{nn} &= \left(\frac{3}{4\pi} \frac{1}{n_d} \right)^{1/3}, \\ \lambda_D^{-2} &= \lambda_e^{-2} + \lambda_+^{-2}, \end{aligned} \quad (2.73)$$

$$\lambda_{e,+}^2 = \frac{2\epsilon_0 \bar{w}_{e,+}}{3e^2 n_{e,+}}.$$

For collisions with the dust particles, the maximum collision frequency has to be calculated every time-step, since it depends on the dust charge, which changes every time-step. Once the type of collisions is chosen, the number of super-particles as well as the dust charge density within the clouds and the velocities of the colliding particles are updated.

When a collision occurs, the energy of the particles is changed (for instance in an ionization, the ionization potential is subtracted and the remaining energy divided over the two electrons), and the new velocity components are calculated, using computer generated random numbers for the angles. A complete description is given in [39, 41].

References

- [1] G. B. Rybicki, A. P. Lightman, *Radiative Processes in Astrophysics*, John Wiley & Sons, New York, 1979
- [2] F. F. Chen, *Introduction to plasma physics and controlled fusion*, Plenum Press, New York, 1984
- [3] A. Bogaerts, E. Neyts, R. Gijbels, and J. van der Mullen, *Spectrochim. Acta B* **57**, 609-658 (2002)
- [4] A. Bogaerts, and R. Gijbels, *J. Anal. At. Spectrom.* **15**, 1191-1201 (2000)
- [5] M. S. Barnes *et al.*, *Phys. Rev. Lett.* **68**, 313 (1992)
- [6] R. V. Kennedy, and J. E. Allen, *J. Plasma Physics* **69**, part. 6, 485-506 (2003)
- [7] R. V. Kennedy, and J. E. Allen, *J. Plasma Physics* **67**, part. 4, 243-250 (2002)
- [8] I. H. Hutchinson, *Principles of plasma diagnostics, first edition*, Cambridge University Press, Cambridge, 1987
- [9] M. Lampe, R. Goswami, Z. Sternovsky, S. Robertson, V. Gavrilishchaka, G. Ganguli, and G. Joyce, *Phys. Plasmas* **10**, 1500 (2003)
- [10] S. A. Khrapak *et al.*, *Phys. Rev. E* **72**, 016406 (2005)
- [11] S. Ratynskaia *et al.*, *Phys. Rev. Lett.* **93**, 085001 (2004)
- [12] O. Havnes *et al.*, *J. Geophys. Res.* **92**, 2281 (1987)
- [13] M. Klindworth, *Fundamentals and Applications of Langmuir Probe Diagnostics in Complex Plasmas*, PhD. Thesis, Christian-Albrechts University, Kiel, 2004
- [14] D. A. Mendis, and M. Rosenberg, *Annu. Rev. Astron. Astrophys.* **32**, 419-463 (1994)

- [15] S. M. Lyth, F. Oyeleye, R. J. Curry, J. Davis, and S. R. P. Silva, *J. Vac. Sci. Technol. B* **24**, Issue 3, 1362 (2006)
- [16] W. I. Milne *et al.*, *J. Mater. Chem.* , 933-943 (2004)
- [17] R. C. Ister, R. W. Wood, C. C. Klepper, N. H. Brooks, M. E. Fenstermacher, and A. W. Leonard, *Phys. Plasmas* **4**, 355 (1996)
- [18] G. L. Delzanno, G. Lapenta, and M. Rosenberg, *Phys. Rev. Lett.* **92**, 035002 (2004)
- [19] H.-C. Wu, B.-S. Xie, *Phys. Plasmas* **12**, 064503 (2005)
- [20] M. R. Akdim, and W. J. Goedheer, *Phys. Rev. E* **67**, 066407 (2003)
- [21] J. E. Daugherty *et al.*, *J. Appl. Phys.* **73**, 1617 (1993)
- [22] S. A. Khrapak, A. V. Ivlev, G. E. Morfill, and H. M. Thomas, *Phys. Rev. E* **66**, 046414 (2002)
- [23] S. A. Khrapak, A. V. Ivlev, S. K. Zhdanov, and G. E. Morfill, *Phys. Plasmas* **12**, 042308 (2005)
- [24] A. V. Ivlev, S. K. Zhdanov, S. A. Khrapak, and G. E. Morfill, *Plasma Phys. Control. Fusion* **46**, B267-B279 (2004)
- [25] A. V. Ivlev, S. K. Zhdanov, S. A. Khrapak, and G. E. Morfill, *Phys. Rev. E* **71**, 016405 (2005)
- [26] I. H. Hutchinson, *Plasma Phys. Control. Fusion* **48**, 185-202 (2006)
- [27] P. S. Epstein, *Phys. Rev.* **23**, 710 (1923)
- [28] S. A. Khrapak, and G. E. Morfill, *Phys. Plasmas* **13**, 104506 (2006)
- [29] O. Arp, D. Block, M. Klindworth, and A. Piel, *Phys. Plasmas* **12**, 0122102 (2005)
- [30] G. Gozadinos, A. V. Ivlev, and J. P. Boeuf, *New J. Phys.* **5**, 32 (2003)
- [31] G. E. Morfill, H. M. Thomas, U. Konopka, H. Rothermel, M. Zuzic, A. Ivlev, and J. Goree, *Phys. Rev. Lett.* **83**, 1598-1601 (1999)
- [32] J. D. P. Passchier, *Numerical Fluid models for RF discharges*, PhD. Thesis, University Utrecht, 1994
- [33] G. J. Nienhuis, *Plasma models for silicon deposition*, PhD. Thesis, University Utrecht, 1998
- [34] M. R. Akdim, *Modelling of Complex Plasmas*, PhD. Thesis, University Utrecht, 2003

- [35] I. Revel *et al.*, J. Appl. Phys. **88**, 2234 (2000)
- [36] E. W. McDaniel, *Collision phenomena in ionized gases*, John Wiley & Sons, New York, 1964
- [37] C. K. Birdsall, and A. B. Langdon, *Plasma Physics via Computer Simulation*, Adam Hilger, New York, 1991
- [38] W. H. Cramer. J. Chem. Phys. **30**, 641 (1959)
- [39] V. Vahedi, M. Surendra, Comp. Phys. Com. **87**, 179-198 (1995)
- [40] W. J. Goedheer, Y. I. Chutov, IEEE Trans. Plasma Sci. **32**, 606-613 (2003)
- [41] M. H. L. van der Velden, W. J. M. Brok, J. J. A. M. van der Mullen, W. J. Goedheer, and V. Banine, Phys. Rev. E **73**, 036406 (2006)

3. Modelling of dust transport in dusty plasma in the presence of a magnetic field

Abstract.

We extended a fully self-consistent two-dimensional fluid model for radio-frequency discharges by adding a homogeneous axial magnetic field and the effect it has on the transport of plasma species in a low temperature dusty discharge. This magnetic field has an important effect on the (ambipolar) diffusion of ions and electrons in the bulk of the discharge. This causes an important change in the force balance of the dust particles and in the timescales for the formation of a dust-free void.

We compare the parameters of the modelled discharge with the parameters of a planet formation region around a Young Stellar Object (YSO). From this, we conclude that a magnetic field has an important effect on the transport of dust in both low temperature RF discharges under micro-gravity conditions and dusty plasmas around YSO's, and must therefore be important for the formation of planets and stars, as well as for the plasma enhanced fabrication of micro-electronics.

Based on :

Phys. Rev. E, **72**, 046403 (2005)

Authors :

V. Land, W. J. Goedheer

3.1 Motivation

Many modern industries rely heavily on the use of plasma to enhance fabrication processes. Plasmas are used to coat surfaces to enhance their durability, for instance the inside of car engines, or for the deposition of thin films with special electric properties, such as the films used in the fabrication of solar cells. Plasma is also useful to very precisely deposit or etch small structures, which is very important for the modern microchip industry. These plasmas usually are chemically active, and ions and radicals can form small nanometer sized clusters, called nanoparticles [1, 2, 3]. Recently, different models have been used to study the formation of nanoparticles, while some of these models included the transport of these nanoparticles through the plasma [4, 5].

Through a process that is not well understood, nanoparticles coagulate to form larger particulates in the micrometer range. We refer to these particulates as "dust particles". The Coulomb interaction for the nanoparticles is not very important since their charge is low, for sizes up to a few nanometers [4]. The coagulation process is therefore believed to involve impact coagulation by Brownian motion or Van der Waals (or dipole-dipole) interactions [6]. The latter force typically goes as $\propto 1/r^6$ and is therefore important only when the nanoparticles are able to come very close to each other.

Once the size of a coagulate reaches the sub-micron or micron range, $R \sim 0.1 - 10 \mu m$, it collects a significant amount of electrons and ions. Its charge can be tens of thousands of elementary charges. Because of this large charge, the plasma-dust and dust-dust interactions become dominant and determine the transport of the dust particles through the plasma. These forces act over much larger distances.

Sometimes electric and magnetic fields are used to guide and confine the plasma, such as in magnetron sputtering devices [7] and of course in fusion devices. There, plasma-wall interactions in the divertor region result in flakes of wall material entering the plasma. The properties of these dusty plasmas are relatively unknown, but the presence of the dust has important effects on the device properties and operation [8].

Recent observations have shown that micrometer sized dust particles are also present in plasmas around Young Stellar Objects (YSO's) [9, 10]. Since in this case the dust particles are orbiting a heavy central object (we assume in Keplerian orbits), we can ignore the force of gravity, which in experiments on Earth usually is the dominant force. Observations of matter outflow and jets in YSO's are connected to magnetic activity and magnetic fields.

Considering the above, the necessity to model the effect of a magnetic field on a dusty plasma, while taking into account the complex interaction between the dust and the plasma, and the corresponding transport of the dust through the plasma, becomes obvious.

3.2 The experiment and the model

The geometry we use in our model resembles that of the PKE experiment discussed in [11, 12]. Figure 3.1 shows this geometry. This experiment has been extensively used on board of the International Space Station to understand the full three-dimensional transport of dust in dusty plasmas. In this experiment argon gas is introduced at low pressures between two electrodes powered with a high frequency (13.56 MHz) potential in push-pull mode and an argon plasma is formed. When the plasma has become periodic (over one RF cycle), dust particles are introduced through two shakers in the upper and lower electrode. The dust particles are illuminated by a laser sheet and a CCD-camera captures the light scattered by the dust particles. We note that the outer walls of the vessel are far away from the plasma and we assume cylindrical symmetry and use a 2-D model.

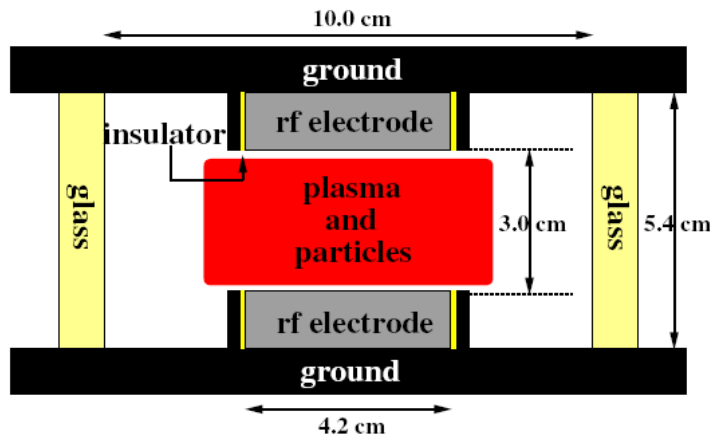


Figure 3.1: Sketch of the PKE experiment, in which argon plasma is formed. The dust particles are introduced through both electrodes, with the use of shakers placed in the center of the electrodes.

For the simulations presented in this chapter, spherical particles with a radius of $6.8 \mu\text{m}$ are used. We have extended the 2-D fluid model for the transport of dust in low temperature RF plasmas [13], which is discussed in chapter 2, to include the effect of a homogeneous axial magnetic field on the plasma parameters.

In the model, the particle balance for the electrons, (positive and negative) ions and metastable atoms, and the energy density balance for the electrons, are solved using the drift-diffusion scheme as explained in chapter 2. Once a periodic solution for the plasma parameters is obtained, dust particles are introduced.

From the plasma parameters, all the forces acting on the dust particles, which include the electrostatic force, the ion drag force and the thermophoretic force,

are calculated on the grid. A drift-diffusion equation for the dust transport is then obtained by assuming that the neutral drag is balanced by these forces. For the electrostatic force, the time-averaged electric field is used. A very important force for the calculation of the dust transport comes from the interaction between ions and the charged dust particles. This force is called the ion drag force. In the simulations presented in this chapter, the original approach by Barnes et al. [14] is used, together with the *electron Debye length* as the maximum impact parameter. See chapter 2 for a description. Even though non-linear scattering, trapped ions, ion flow speed and ion-neutral collisions can play an important role [15, 16, 17, 18], they are not considered here. The implementation of the complete ion drag model is presented in chapter 5. It suffices to say that the error introduced by using the old model for the current simulations is less than 25 % for a limited volume of the plasma, and even decreases for higher magnetic field.

3.3 Dusty plasmas without magnetic field, and with $B=0.25$ Tesla

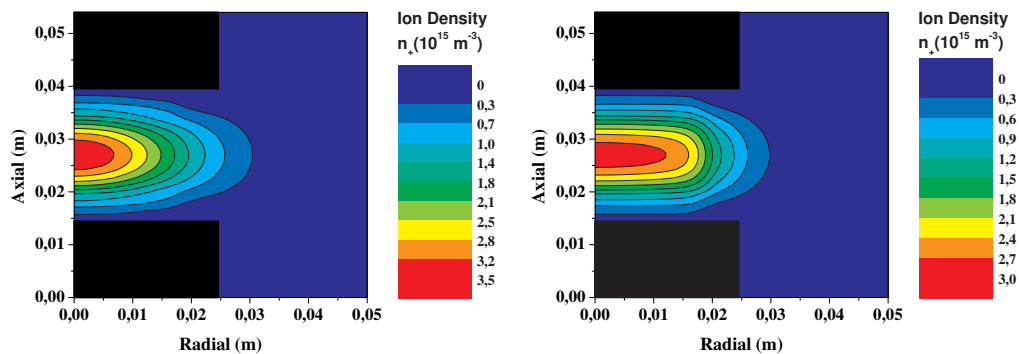


Figure 3.2: **Left:** Time averaged ion density for a magnetic field- and dust-free discharge. The plasma is mostly formed between the electrodes. We can clearly see the bulk of the discharge as the central maximum in the ion density. No dust particles have been added.

Right: Similar figure, but now with magnetic field. The bulk of the plasma is modified by the application of a magnetic field. The maximum value of the ion density is less, but the volume filled by the ions larger, indicating that the total numbers of ions is roughly the same in both discharges. No dust particles have been added.

In this section, we compare the profiles for a magnetic field-free dusty dis-

charge and a dusty discharge with a magnetic field of $B = 0.25$ Tesla. We use a background pressure of 40 Pa with a 100 Volt peak-to-peak potential at 13.56 MHz. Please note that we do not consider negative ions (irrelevant for argon), nor metastables in these calculations. We first compare the ion density. In both discharges the plasma is mainly created between the electrodes, which are the black rectangles in the figures.

Figure 3.2 shows the ion density profiles before any dust is introduced. In the left figure no magnetic field is applied. In the figure on the right, the magnetic field applied has a value of $B = 0.25$ Tesla. We can see how the ion density profile changes due to *the presence of the magnetic field only*. The quasi neutral bulk is extended radially. However, the maximum value of the ion density in the case of an applied magnetic field is less, indicating that the total amount of ions in the discharge is approximately the same.

In figure 3.3 and further, we compare profiles for magnetic field-free plasmas and plasmas with a magnetic field, at the end of the simulation, at which time 10^6 dust particles, with a radius of $6.8 \mu\text{m}$, have been added. We can see how the change in the ion density profile induced by the magnetic field changes the plasma and dust parameters.

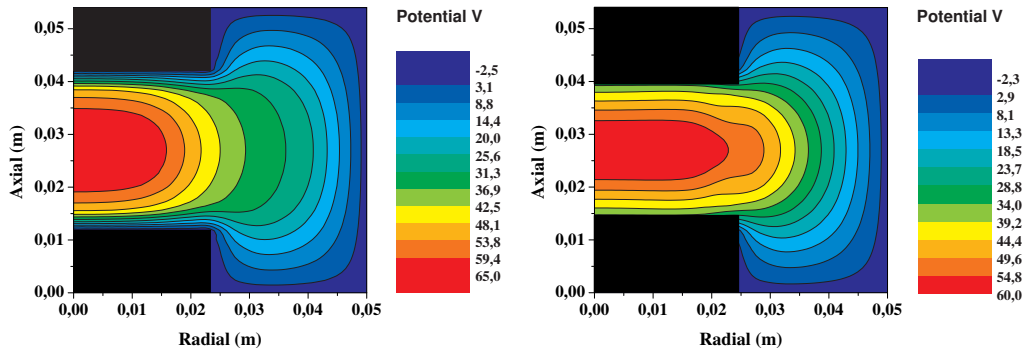


Figure 3.3: **Left:** The time-averaged potential profile for the magnetic field-free discharge. The equipotential in the center corresponds to the quasi-neutral bulk of the plasma, where the plasma densities have their maximum. In front of the electrodes, we see the large sheath electric fields. Towards the outer wall we see the electric field caused by charge separation.

Right: The same for the magnetized discharge. The equipotential of the quasi-neutral bulk now has a cigar-like shape following the changed plasma profile.

In figure 3.3 we present the potential profile averaged over one RF-cycle. The left figure shows the magnetic field-free case. We see the quasi-neutral bulk of

the plasma between the electrodes as the equipotential area. In front of the electrodes the large electric fields of the sheath-regions appear. Near the end of the electrodes the radial electric field changes from approximately zero to an electric field pointing towards the outer walls. This electric field, generated due to the high mobility of the electrons, accelerates the ions towards the outer wall.

The right figure shows the potential for the magnetized discharge. The potential profile is almost the same, however, we see a big change in the electric field-free bulk of the plasma, which has become cigar-shaped, much like the ion density profile. This change in the bulk potential results from the reduced electron mobility in the applied magnetic field. Since the transport in the bulk is ambipolar, the ion transport is also affected.

Figure 3.4 shows the ion density profiles at the end of the simulations, when the dust has reached its equilibrium density profile. In the bulk of the discharge the ion density profiles are similar to the ones shown in figure 3.2, with the exception that the recombination of ions (and electrons) on the dust particles has reduced the ion (and electron) density radially, confining the plasma to a smaller volume, i.e. inside the dust free void, as was also described in [13]. Clearly, the effect of the magnetic field on the plasma parameters is also important when a large number of dust particles is introduced to the plasma, since also here the ion profiles look very different.

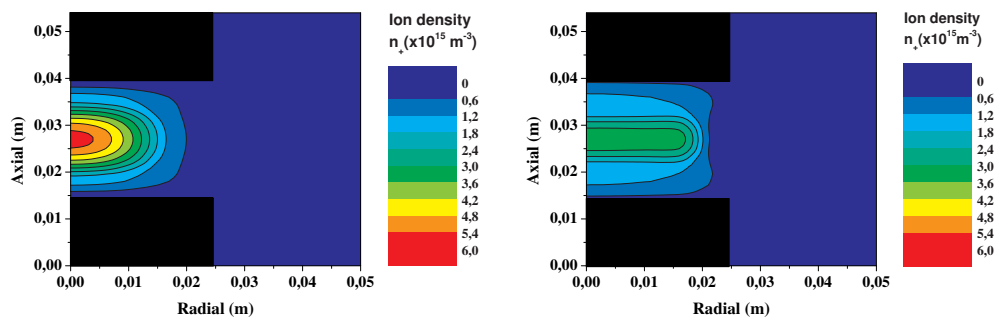


Figure 3.4: **Left:** Time averaged ion density for a magnetic field-free discharge, *after the introduction of one million dust particles*. One can also see the effect of recombination of the ions on dust particles.

Right: Same as on the left, but now with the magnetic field. The bulk has a cigar-shaped maximum in the ion density, corresponding to the bulk seen in the potential of figure 5. The maximum value of the ion density is less, indicating that the total number of ions is roughly the same in both discharges.

The change in ion density is reflected in the dust density profiles. The ions are accelerated out of the center of the discharge, causing the ion drag force which

pushes the dust particles out of the center of the discharge. A dust-free void is formed in the center of the discharge.

The dust density for the magnetic field-free discharge, presented in figure 3.5 on the left, clearly shows the dust-free void, as well as the dust-free sheath regions. In this case a local maximum in the dust density is created outside the electrodes, due to the transport of dust particles in the radial direction. For this discharge the time needed to form a closed boundary around the void is 1.15 seconds (see section 3.4).

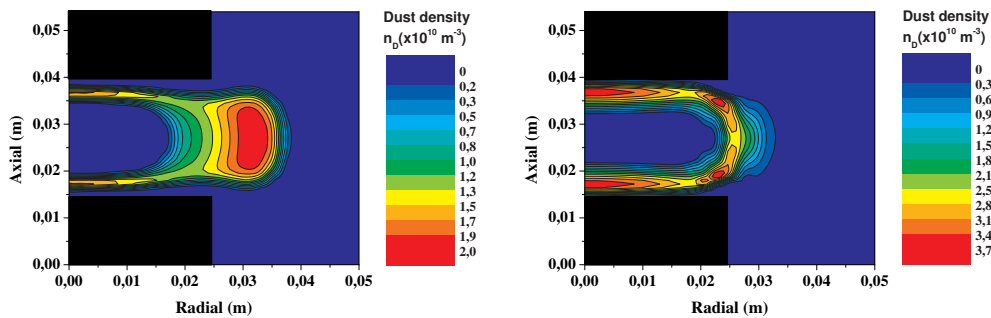


Figure 3.5: **Left:** Dust density profile for a magnetic field-free dusty discharge. We can clearly see the dust-free void in the center of the discharge. The sheath regions are also dust-free. In this case, we find a local maximum in the density just outside of the electrodes. The closed boundary around the void was formed after ± 1.15 seconds.

Right: Dust density profile for a magnetized dusty discharge. The central dust-free void is now clearly cigar-shaped, due to the change in the ion density profile. There is no local maximum in the dust density outside of the electrodes. In this magnetized case, the void was closed after 0.55 seconds, about twice as fast as in the unmagnetized case.

The right figure shows the dust density for the magnetized case. The void has a very different shape, due to the change in the ion density profile. The much sharper boundary of the ion density profile causes a much sharper boundary of the dust-free void. We also see that the sheath regions are less clear. The dust charge is slightly less in front of the electrodes in this case ($36.000e$ to $48.000e$ instead of $43.000e$ to $49.000e$ in the un-magnetized case), which means that the electrostatic repulsion is slightly less, moving the force balance between the axial ion drag force and the electrostatic force closer to the electrode surfaces.

The most important observation is that for a magnetic field strength of $B = 0.25$ Tesla, a closed boundary around the void is formed *already after 0.55 seconds*. This means there is a big difference in the dust-transport properties of both

discharges. We also observe that there is no distinct maximum in the dust density formed outside of the electrodes.

The dust inserted in the discharge becomes negatively charged, because of the high electron mobility compared to the ion mobility. Towards the outer wall the electron density drops sharply, resulting in a large volume with a positive net space charge. The electrons also cool down in the outer regions of the discharge and both these effects result in a reduction of the negative charge carried by the dust. This effect is even enhanced by the magnetic field. The typical amount of electrons on a dust particle, indicated by Z_D , in the plasma bulk is 40.000 and is plotted on the left in figure 3.6 for the magnetic field-free discharge. The right figure shows how the dust charge in the bulk of the magnetized discharge is almost the same as the dust charge in the un-magnetized discharge. Note that the charge per particle is computed everywhere in the simulation based upon the calculated plasma parameters, also in regions where there is no dust present.

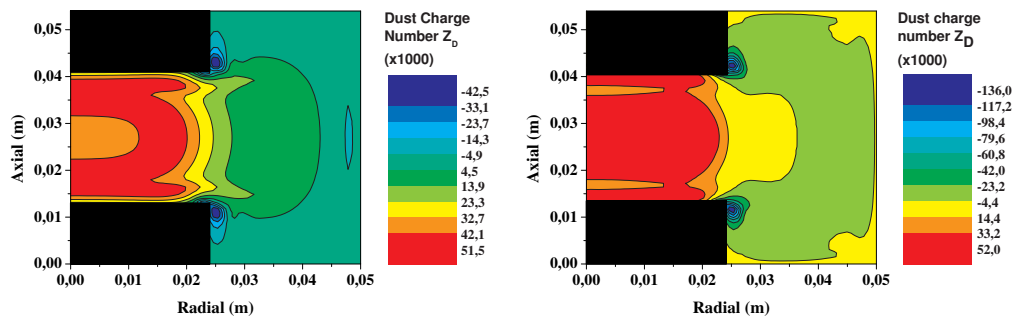


Figure 3.6: **Left:** Number of electrons on a dust particle for a magnetic field-free dusty discharge. The dust is mainly negatively charged, which results from the high electron mobility compared to the ion mobility. Typical dust charges are on the order of 10^4 electrons.

Right: Number of electrons on a dust particle for the magnetized discharge. The dust charge is again negative. The typical dust charge is similar to that of the un-magnetized discharge, in the order of 10^4 electrons per dust particle.

3.4 Dust transport with an applied magnetic field

An important observation is the large reduction in the time needed to form a closed dust-free void. In order to compare the results for different magnetic field strengths, we define the time when the dust sources are turned on as $t = 0$. Furthermore, we define the time when a dust-free void is formed as that moment when

dust contours of $n_d = 8 \cdot 10^9 \text{ m}^{-3}$ are closed around the void. This value has no physical meaning, but is chosen only because this value was easy to identify. It would be physically more appropriate to use the coupling parameter as a constraint, for instance by identifying the void formation time as the moment where $\Gamma > \Gamma_{cr} \approx 160$ [19], but the coupling parameter becomes very large for small values of the density, which makes it very hard to identify the right time from this criterion.

The void formation times found in the simulations are shown in figure 3.7. The error bar indicates the possible error we make in taking the right frame. For higher magnetic fields, the void closes faster and it is more difficult to identify the moment when the dust contours are closed. For low magnetic fields, we estimate an error of approximately one frame, but for higher magnetic fields the error is two frames. Each frame corresponds to a duration of 0.02 seconds.

We see that for increasing magnetic field, the time needed to form a closed void is decreased by more than a factor of 2. This means that either the transport of dust particles through the plasma is increased, or the distance to the force balance point is reduced, or a combination of both factors. In order to understand this reduction in the void formation time, as well as the change in the void shape, we will compare the plasma and dust parameters *at the moment the void is closed*. Since these times are different for different magnetic fields, this also means that the total number of dust particles at these times will be different.

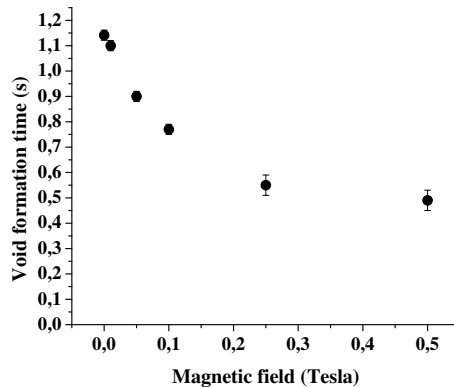


Figure 3.7: The time needed to form a closed void. The definition is taken to be closed contours of dust density $n_d = 8 \cdot 10^9 \text{ m}^{-3}$ around the void. For higher magnetic fields, the time needed to form a closed void becomes much shorter. This means that there is increased transport of dust in the plasma.

The formation of a dust-free void is the result of dust transport through the

plasma. Dust particles will move to points where all the forces acting on them cancel. The two most important forces acting on the dust particles are the ion drag force and the electrostatic force. The thermophoretic force does not play an important role. The electrostatic force pulls the negatively charged dust particles inwards, while the ion drag force is pushing the dust particles towards the outside. The change in the ion density distribution is therefore important for the transport of dust. The left frame in figure 3.8 shows the ion density profiles in the plane of symmetry at $z = 0.027$ m. For higher magnetic fields, large gradients appear near the edge of the electrodes at $r = 0.021$ m. The quasi-neutral bulk between the electrodes becomes larger for higher magnetic fields. The total number of ions, which corresponds to the surface under the graphs, remains about equal, which indicates that the total ionization does not change. On the right, we see that for high magnetic fields, the gradient in the ion density almost doubles for the highest magnetic field. The change in the gradient causes a change in the forces acting on the dust particles near that point on the symmetry axis where all the forces balance.

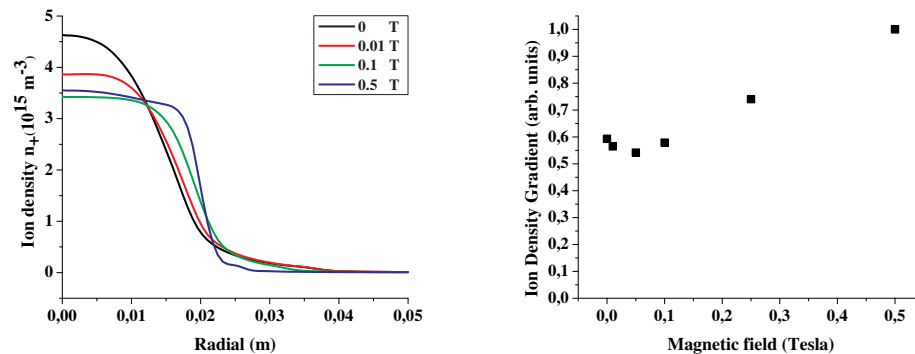


Figure 3.8: **Left:** Time averaged ion density profiles in the plane of symmetry at $z = 0.027$ m for different values of the magnetic field. A large quasi-neutral bulk builds up between the electrodes, together with an increasing gradient at the edge of the electrodes.

Right: The radial gradient in the ion density near the edge of the electrode, in the plane of symmetry in arbitrary units. We see how for low magnetic fields the gradient is slightly decreased. For high magnetic fields the gradient becomes larger.

Figure 3.9 shows the net radial force in the plane of symmetry. The dust particles move to the points where the net force is zero. These points are marked by the different colored lines on the horizontal axis. The black lines indicate the gradient in the force at these balance points. Note that for the magnetic field-free

discharge, the force balance occurs far away from the discharge center, as was indicated by the local dust density maximum in figure 3.5. For the discharges with large magnetic fields, the force balance lies much closer to the discharge center.

The change in the ion density profiles strongly affects the transport of dust in the discharge. The magnetic field does not change the mobility and diffusion of the ions directly however, since the ions are too heavy to be magnetized by the magnetic fields used in the simulations. In order to understand the change in the ion density profiles, we analyze the differences in ion transport in the next section.

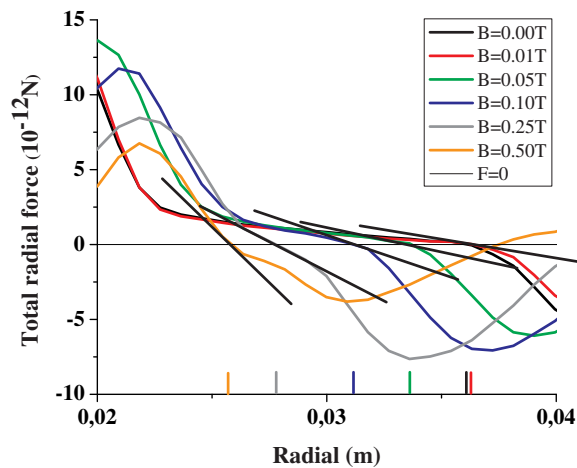


Figure 3.9: The net force acting on dust particles in the radial direction in the plane of symmetry at $Z=0.027$ m. The points where the forces balance for different values of the magnetic field, is indicated by the colored lines on the horizontal axis. The black lines shows the gradient in the force at these points.

Since we calculate the drift velocity of the dust assuming that the friction with the neutrals balances all other forces, there can not be an overshoot followed by a damped oscillation when the dust moves towards the equilibrium point. In case of low friction, the frequency of the oscillations would also be affected by the magnetic field. The stronger derivative of the net force would increase this oscillation frequency with increasing magnetic field. We are not able to study this within the context of our model. This is also true for dust vortices, often observed in dusty plasmas under micro-gravity. However, the force field calculated to simulate the dust transport does show vortices when used to track single dust particles, as was shown in [20]. The results were similar to the theoretical calculations performed in [21]. We also do not consider Brownian motion of dust particles around equi-

librium positions, which might affect the true transport timescales involved. However, the effect of Brownian motion will not be a dominant transport mechanism for the processes simulated here.

3.5 Ion transport and ambipolar diffusion

One possibility for the large radially extended bulk in the ion density is an increase in the effective electric field in the bulk. The left frame of figure 3.10 shows the electric potential in the bulk of the discharge. We see that it extends more and more in the radial direction for increasing magnetic field. We do not observe an increase in the bulk effective electric field, in fact, we see that it decreases.

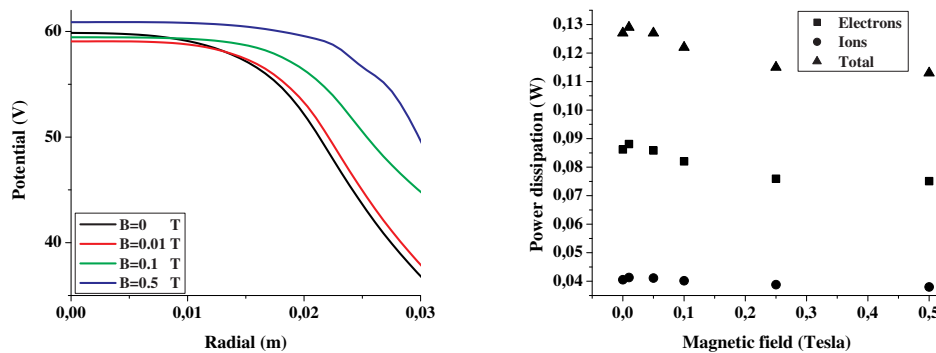


Figure 3.10: **Left:** Time averaged potential profiles in the bulk in the plane of symmetry, for different values of the magnetic field. There is no enhanced radial component of the electric field in the quasi-neutral bulk, the gradient in the potential is practically the same for different values of the magnetic field, or even decreases slightly.

Right: The dissipated power for the electrons, ions and the total dissipated power for different values of the magnetic field, indicating the level of ionization. The dissipated power hardly changes, which means that the total ionization in the discharge remains the same for increasing magnetic field.

Another explanation would be a change in ionization. We have already seen that the total number of ions does not change very much. A change in ionization will also be reflected in a change in the dissipated power in the plasma. In the right frame, we see the dissipated power. It remains about the same for different values of the magnetic field; ~ 0.1 Watt. There is no change in the total ionization in the discharge large enough to explain the difference in the ion density distribution.

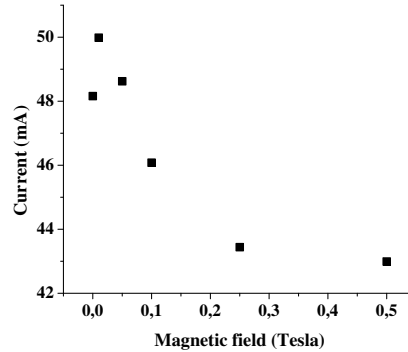


Figure 3.11: The current to the electrodes for different values of the magnetic field. The current to the electrodes does not change very much, which means that the current towards the outer walls does not change very much as well (the total current has to be conserved). Thus, the current distribution in the discharge does not show an important change for increasing magnetic field.

A change in the currents might explain the changes observed; maybe more current is directed to the outer wall, instead of to the electrodes, leading to more Ohmic heating of electrons in the radial direction, causing more ionization radially than axially. However, the current to the electrodes, shown in figure 3.11, also remains equal. There is no important change in the current distribution inside the discharge with an applied magnetic field.

The only remaining explanation is therefore a change in the diffusion of positive ions in the bulk towards the outer wall. The diffusion in the quasi-neutral bulk will be mainly *ambipolar diffusion*. Ambipolar diffusion is based on the equality of the electron and ion fluxes, together with the assumption of quasineutrality. In a dusty plasma this reads $n_+e = n_e e + eZ_D n_D$ and the equations for the ambipolar diffusion have to be changed accordingly [22, 23]. However, when the dust particles are introduced, the ion drag forcing them to move "around the void", is mainly due to ions diffusing out of the bulk of the discharge, where no dust is present. The ions will therefore diffuse out of the bulk with a diffusion coefficient equal to the normal ambipolar diffusion coefficient:

$$D_a = \frac{\mu_i D_e + \mu_e D_i}{\mu_e + \mu_i}. \quad (3.1)$$

Using equation (2.68), we notice that the ambipolar diffusion coefficient is reduced when the electrons become magnetized. Figure 3.12 shows the electron-magnetized ambipolar diffusion coefficient for the discharge parameters used in

the simulation. Without magnetic field, the ambipolar diffusion coefficient reduces to the classical value for $\mu_e \gg \mu_i$; $D_a = D_i(1 + T_e/T_i)$, which is indicated by the dashed line. For very large magnetic fields, the ambipolar diffusion coefficient approaches the magnetized electron diffusion coefficient, indicated by the dot-dashed line. We can also rewrite the equality of fluxes in the bulk to derive the *ambipolar electric field*. The result for electropositive discharges [24] is:

$$\mathbf{E}_{amb} = -\frac{d \ln(n_{+,e})}{dx} \left(\frac{D_e - D_+}{\mu_e + \mu_+} \right). \quad (3.2)$$

Comparing the calculated ambipolar electric field with the effective electric field in the bulk found from the simulations, we find a good agreement, as shown in table (3.1).

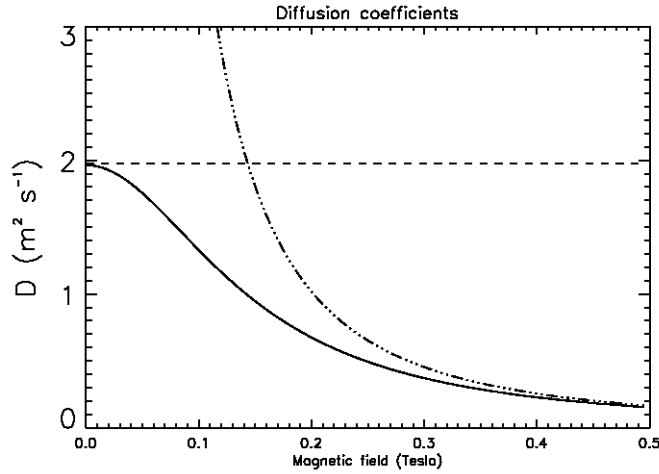


Figure 3.12: Radial ambipolar diffusion coefficient for different magnetic field strengths. The solid line represents the ambipolar diffusion, the dashed line the magnetic field free value and the dot-dashed line the magnetized electron diffusion coefficient. We see that for higher magnetic fields the diffusion of ions out of the bulk becomes less, because of the magnetization of the electrons, and approaches the *magnetized electron* diffusion.

Since the total ionization remains the same, while the diffusion of the ions is reduced for higher magnetic field, the area between the electrodes fills up with ions, resulting in the cigar-shaped bulk. The total current to the outer wall is roughly the same however, as figure 3.11 shows. This means that the gradient in the ion density must increase, since the flux of ions in the bulk is now given by the ambipolar diffusive flux:

$$\Gamma_+ = -D_a \frac{\partial n_+}{\partial x}. \quad (3.3)$$

B (Tesla)	Ambipolar field (V/m)	Bulk field (V/m)
0	239	240
0.01	140	150
0.05	100	125
0.1	52	60
0.25	38	42
0.5	19	20

Table 3.1: The calculated ambipolar electric field according to equation (3.2) and the effective electric field found from the model according to equation (2.64) and (2.65) for different values of the applied axial magnetic field, \mathbf{B} . We see that in the bulk of the discharge the effective electric field equals the ambipolar electric field. The flux of plasma particles in the bulk of the discharge is therefore the ambipolar flux. The magnetic field reduces the ambipolar electric field in the bulk and thus the ambipolar flux of plasma particles out of the bulk of the discharge.

We indeed see that the ion density gradient near the edge of the void increases with increasing magnetic field and thus with decreasing ambipolar diffusion. One more thing we need to consider is a possible change in the charging of the dust particles in the presence of a magnetic field, for instance by a change in the electron orbits.

3.5.1 Effect of magnetic field on charging

Until now, we assumed that the effect of the magnetic field on the charging currents to dust particles can be neglected. This is important for the interaction between dust particles, and thus for the formation of voids as well. In [25] it was mentioned that a magnetic field can have an important effect on the charge of dust particles. The charge is reduced when the electrons are magnetized and the electron cyclotron radius becomes smaller than the capture radius of the dust particles as derived by OML theory; $R > r_c$.

For an electron orbiting with constant cyclotron radius, there are two degrees of freedom, the translational direction, parallel to the magnetic field, and the azimuthal direction, perpendicular to the magnetic field. Assuming that both degrees of freedom contribute equally to the kinetic energy of the electron, i.e.

$$k_B T_e = \frac{1}{2} m_e v_e^2 = \frac{1}{2} m_e (v_{\perp}^2 + v_{\parallel}^2) = \frac{1}{2} m_e (2v_{\perp}^2), \quad (3.4)$$

we rewrite the criterion for the reduction of the dust charge, by using $v_{\perp} = \omega_{c,e} r_c = eB r_c / m_e$ as:

$$r_c B = \frac{m_e}{e} \sqrt{\frac{k_B T_e}{m_e}}. \quad (3.5)$$

This means that for a change in the charging of dust particles by the magnetization, we can find the critical magnetic field as:

$$RB > \frac{m_e}{e} \sqrt{\frac{k_B T_e}{m_e}}. \quad (3.6)$$

Filling in the numbers, this gives:

$$R(\mu m)B(\text{Tesla}) > 2.386 \sqrt{T_e(\text{eV})}, \quad (3.7)$$

which was also stated by Tsytovich et al. in units of kGauss [25]. The critical magnetic field for the ions is $\mu = \sqrt{m_i T_i / m_e T_e}$ times higher.

In our simulations the dust particle radius is $6.8 \mu m$. The typical electron energy is a few eV. This means that the critical magnetic field strength is approximately 0.6 Tesla. In our simulations we stayed below this value and therefore we conclude that the magnetic field does not have an important effect on the charging of the dust particles. Therefore we can still use the OML theory to calculate the dust charge.

3.6 Comparison with planet formation region

We start with considering the magnetization of the ions and electrons in dusty plasma around a YSO. Using literature [26], we find the values for the neutral density, temperature and the magnetic field: $n_n \approx 10^{17} \text{ m}^{-3}$, $T_n \approx 100 \text{ K}$, $B \approx 10^{-3} \text{ T}$. The neutral pressure is $P = n_n k_B T_n = 1.38 \cdot 10^{-4} \text{ Pa} = 1.04 \cdot 10^{-6} \text{ Torr}$. The mobility at such low background pressures is very high, $\mu_e = 30/P(\text{Torr}) = 2.9 \cdot 10^7 \text{ m}^2 \text{ s}^{-1} \text{ V}^{-1}$. The electron momentum transfer frequency is then $\nu_{m,e} = e/m_e \mu_e \approx 6.1 \cdot 10^3 \text{ Hz}$. The electron cyclotron frequency is given by $\omega_{c,e}/2\pi = eB/2\pi m_e \approx 2.8 \cdot 10^7 \text{ Hz}$. So, $H_e = 4590 \gg 1$ as in our simulations.

For the ion species we assume that hydrogen will be the most common element, and we estimate that hydrogen is $\sqrt{m_{ar+}/m_{H+}} \approx 6$ times more mobile than the argon used in our model [27]. Then, we find a mobility of $\mu_{H+} \approx 8.4 \cdot 10^5 \text{ m}^2 \text{ s}^{-1} \text{ V}^{-1}$. The momentum transfer frequency has a value of $\nu_{m,H+} = e/m_p \mu_{H+} \approx 115 \text{ Hz}$. The ion cyclotron frequency is given by $\nu_{c,H+} = eB/2\pi m_p \approx 1.5 \cdot 10^4 \text{ Hz}$. In this case, $H_{H+} \approx 132 \gg 1$. We see that $H_e \gtrsim H_{H+}$.

So, for a pure atomic hydrogen plasma, the ambipolar diffusion would equal the magnetized ion (or electron) diffusion, since they are both roughly equal. Even though this differs from our model situation, the ambipolar diffusion would still

be reduced, compared to the case without magnetic field, since the ambipolar diffusion coefficient would be $D_a = D_i(1 + T_e/T_+) \approx D_e$ for $\mu_e \gg \mu_+$ and $T_e \gg T_+$, which both hold. Furthermore, plasmas around YSO's most likely also contain molecular hydrogen ions (H_2^+) due to the low temperature, and most likely even He^+ , as hydrogen and helium are the most common elements, which would bring the situation closer to our simulations, due to their higher mass.

The dust particle diameters as observed in [9, 10] and as observed in meteorites on Earth are all in the μm range [28]. Therefore, our choice of a radius of $6.8 \mu m$ fits well within the range of these observations.

The source of ionization in a star formation region around a YSO consists of ionization by cosmic rays and by the intense UV flux originating from the YSO. The remaining energy of the UV photon after the ionization will almost completely be picked up by the electron, leaving a cold population of ions and a hot population of electrons, similar to the situation in our code.

Even though the experiment in our model has walls at which the plasma ends, the local ionization and transport of plasma particles in the quasi-neutral part is similar. Once the ionization by cosmic rays and UV photons becomes smaller than the recombination of the plasma to neutrals, the plasma ends. An interior plasma is therefore surrounded by neutral gas, which will act not so much as a sink of plasma, but at least as a sink of energy. The role of UV-radiation in a dusty plasma has been discussed in [29], and will be further investigated in chapter 7.

In our model we use a fluid description of the plasma and dust particles. This can be done since the Knudsen number $l_{m,fp}/L_{exp}$ is very small, with $l_{m,fp}$ the mean free path of the particles, which is in the order of a millimeter, and L_{exp} the size of the experiment, which is several centimeters. In a planet formation region $l_{m,fp}$ is much larger, due to the low background density. However, L can be hundreds of A.U.'s. There are many collisions of plasma particles with the background within the dimensions of the YSO plasma. The only difference would involve the timescales on which collisions occur.

The process of planet formation includes the process of the actual formation of micrometer sized dust particles through the coagulation of weakly charged, nanometer sized particulates, which involves weak, short range forces. However, a large part of the planet formation process involves the agglomeration of larger, micrometer sized dust particles. These particles will carry a significant charge and therefore the plasma-particle and interparticle forces will dominate over weak, short range forces and the transport of dust particles through the plasma becomes important.

We have shown that a magnetic field plays an important role in the transport of plasma and dust particles in low temperature plasmas, which shares many parameters with the dusty plasmas around YSO's. The better confinement of electrons as compared to ions creates regions where the ratio of the ion and electron den-

sity becomes so high that the dust may even get a positive charge, thus enhancing agglomeration. We therefore conclude that magnetic fields play an important role in the transport of dust particles, thus in the possibility of agglomeration of these dust particles and most likely in the process of planet formation in general.

3.7 Conclusions

A magnetic field in a low pressure RF discharge under micro-gravity conditions has important consequences for the transport of plasma particles and consequently for the transport of dust. The electrons are magnetized and their perpendicular mobility and diffusion coefficient are reduced. This also reduces the ambipolar diffusion of plasma particles out of the quasi-neutral bulk of the discharge.

The ion density profile is affected by the magnetic field and the quasi-neutral bulk covers a larger part of the area between the electrodes. For high magnetic fields a large gradient in the ion density builds up. The point where all the forces acting on the dust particles cancel moves inward. The large gradient in the ion density results in a large gradient in the total force around this point. The combined effect of the reduced distance injected dust particles have to travel before reaching force balance and the increased force they experience close to this point, results in a reduction of the timescale on which a closed void is formed. We believe that it is important to check our findings in future low temperature RF experiments, extended with an applied magnetic field.

References

- [1] G. S. Selwyn, J. Singh and R. S. Benett, J. Vac. Sci. Technol. A **7**, 2758 (1989)
- [2] M. Meaudre, R. Meaudre, R. Butté and S. Vignoli, J. Appl. Phys. **86**, 946 (1999)
- [3] P. Roca i Cabarrocas, J. Non-Cryst. Solids **266-269**, 31 (2000)
- [4] U. Kortshagen and U. Bhandarkar, Phys. Rev. E **60**, 887 (1999)
- [5] K. de Bleecker, A. Bogaerts and W. Goedheer, Phys. Rev. E **70**, 056407 (2004)
- [6] M. Z. Jacobson and J. H. Seinfeld, Atm. Env. **38**, 1839-1850 (2004)
- [7] H. Kakati, A. R. Pal, H. Bailung, and Joyanti Chutia, J. Appl. Phys **100**, 083303 (2006)
- [8] J. Winter, Plasma Phys. Control. Fusion **46**, B583-B591 (2004)
- [9] Y. K. Okamoto *et al.*, Nature **431**, (2004)
- [10] C. M. Telesco *et al.*, Nature **433**, (2005)
- [11] G. E. Morfill *et al.*, Phys. Rev. Lett **83**, 1598 (1999)
- [12] A. P. Nefedov, G. E. Morfill *et al.*, New J. Phys. **5**, 33.1-33.10 (2003)
- [13] M. R. Akdim, W.J. Goedheer, Phys. Rev. E. **67**, 066407 (2003)
- [14] M. S. Barnes *et al.*, Phys. Rev. Lett. **68**, 313-316 (1992)
- [15] S. A. Khrapak *et al.*, Phys. Rev. E. **66**, 046414 (2002)
- [16] M. Lampe *et al.*, Phys. Rev. Lett. **86**, 5278 (2001)
- [17] I. H. Hutchinson, Plasma Phys. Control. Fusion **47**, 71 (2005)
- [18] A. V. Ivlev *et al.*, Phys. Rev. Lett. **92**, 205007 (2004)
- [19] S. Ichimaru, Rev. Mod. Physics **54**, 1017 (1982)
- [20] M. R. Akdim and W. J. Goedheer, Phys. Rev. E. **67**, 056405 (2003)

-
- [21] O. S. Vaulina, A. A. Samarian, O. F. Petrov, B. W. James and V. E. Fortov, *New J. Phys.* **5**, (2003)
- [22] J. X. Ma *et al.*, *Phys. Plasmas* **9**, 5 (2002)
- [23] Sh. Amiranashvili and M. Y. Yu, *Phys. Plasmas* **9**, 11 (2002)
- [24] R. N. Franklin, *J. Phys. D: Appl. Phys.* **36**, 828-831 (2003)
- [25] V. N. Tsytovich, N. Sato and G. E. Morfill, *New J. Phys.* **5**, 43.1-43.9 (2003)
- [26] G. T. Birk., *A&A* **330**, 1070-1076 (1998)
- [27] E. W. McDaniel, *Collision phenomena in ionized gases*, (John Wiley & Sons, 1964)
- [28] M. Zolensky *et al.*, *Meteoritics & Planetary Science* **38**, 305-322 (2003)
- [29] V. E. Fortov *et al.*, *New J. Phys.* **5**, 102.1-102.17 (2003)

4. Experiments on dusty DC discharge with applied magnetic field

Abstract. *The secondary effect of an applied magnetic field in a plasma is the occurrence of drift velocities of charged particles. In typical dusty plasma experiments, the so called $\mathbf{E} \times \mathbf{B}$ drift is dominant when the magnetic field is homogeneous. This drift in the micro-gravity experiment simulated in chapter 3 has been calculated. The resulting dust flow is shown in this chapter.*

We performed experiments in a dusty DC discharge to measure the effect of such a magnetic field induced flows on the dust transport. This chapter introduces the experiment, shows how the dusty plasma parameters were found and presents the results and conclusions regarding the dust response to the magnetic field.

Both the plasma as well as the dust show a response in the $\mathbf{E} \times \mathbf{B}$ direction to a change in the magnetic field. The dust response consists of two distinct parts; first a fast response on the same timescale as the plasma response, followed by a second slow response on a timescale of seconds. The fast response is most likely caused by the flow of ions in the changing background potential. The slow response is most likely the transport of dust towards the new equilibrium position when the plasma has settled, involving the balance between the plasma induced forces and the neutral drag.

Based on Oral/Poster: :

7th WELTPP, Kerkrade, The Netherlands (2004)/

DPP05, Denver, United States of America (2005)

Authors :

V. Land, W. J. Goedheer /

V. Land, E. Thomas, Jr., and Jeremaiah Williams

4.1 Motivation

In chapter 2 it is described how in the drift-diffusion approximation the flux of plasma particles can be described by

$$\Gamma_j = n_j \mu_j \mathbf{E} - D_j \nabla n_j, \quad (4.1)$$

and how in the presence of a magnetic field the perpendicular mobility and diffusion coefficient of magnetized particles (with $\nu_{m,j}/\omega_{c,j} < 1$) has to be replaced through

$$\mu_{\perp,j} (D_{\perp,j}) \rightarrow \left[1 + \frac{\omega_{c,j}^2}{\nu_{m,j}^2} \right]^{-1} \times \mu_{\perp,j} (D_{\perp,j}). \quad (4.2)$$

This equation is not complete though. For a homogeneous magnetic field (so ignoring any gradient in the magnetic field), equation 4.1 becomes,

$$\Gamma_j = n_j \mu_j \mathbf{E} - D_j \nabla n_j + \left(\frac{\mathbf{v}_E + \mathbf{v}_{P,j}}{1 + \frac{\nu_{m,j}^2}{\omega_{c,j}^2}} \right) n_j, \quad (4.3)$$

with,

$$\begin{aligned} \mathbf{v}_E &= \frac{\mathbf{E} \times \mathbf{B}}{B^2}, \\ \mathbf{v}_{P,j} &= \frac{-\nabla P \times \mathbf{B}}{Z_j e n_j B^2}. \end{aligned} \quad (4.4)$$

These terms are drift velocities with which the charged particles will flow through the plasma, induced by the magnetic field. For a general force \mathbf{F} acting on the plasma particles, a drift velocity is introduced, $\mathbf{v}_{dr} = \mathbf{F}_j \times \mathbf{B}/q_j B^2$. Due to the symmetry considerations, these terms play no role in the calculations of chapter 3, however, the induced flow of plasma can interact with dust particles. Especially an additional flow of ions in a magnetized discharge causes an additional ion drag term, which leads to dust transport.

We can make an estimate of the relative importance of the drift velocities. The absolute value of the ratio of the velocities can be written, using $\mathbf{E} = -\nabla V$, as

$$\left| \frac{\mathbf{v}_E}{\mathbf{v}_P} \right| = \frac{en \nabla V}{\nabla P}. \quad (4.5)$$

Assuming constant temperature for the plasma particles and equal gradient lengths for the potential and the density, we can rewrite the above, using the ideal gas law $P = nk_B T$,

$$\left| \frac{\mathbf{v}_E}{\mathbf{v}_P} \right| \approx 10^4 \frac{n}{T(K)} \frac{\Delta V}{\Delta n}. \quad (4.6)$$

From the center of the discharge to the outer wall $\Delta n \approx n$ and $\Delta V \approx (10 \sim 100 \text{ Volts})$, so that the above becomes,

$$\left| \frac{\mathbf{v}_E}{\mathbf{v}_P} \right| \approx \frac{10^4}{T(K)} (10 \sim 100) = \frac{10^5 \sim 10^6}{T(K)}. \quad (4.7)$$

We see that both for ions ($T_+ \approx 10^2 K$) and electrons ($T_e \approx 10^4 K$), the $\mathbf{E} \times \mathbf{B}$ drift is the dominant magnetic field induced drift velocity. Therefore, an additional drift flux of ions perpendicular to both $\mathbf{E}(r)$ and $\mathbf{B}(z)$ will be generated by the electric field, given by

$$\Gamma_{dr} = n_+ \left(\frac{\omega_{c,+}^2}{\nu_{m,+}^2 + \omega_{c,+}^2} \right) \frac{\mathbf{E}(r) \times \mathbf{B}(z)}{B^2}, \quad (4.8)$$

which points in the $-\theta$ direction for the discharge in chapter 3. When this flux of ions interacts with a cloud of dust particles, it will lead to an additional azimuthal ion drag force.

Assuming that in equilibrium this induced ion drag is balanced by the neutral drag force, the dust flow velocity induced by these ions drifting with the $\mathbf{E} \times \mathbf{B}$ drift can be expressed as,

$$\mathbf{v}_{dr} = \frac{m_+ v_s}{m_D \nu_{mD}} (\sigma_s + \sigma_c) \Gamma_{dr}, \quad (4.9)$$

A calculation of the induced dust drift velocity is shown in figure 4.1.

Experimental studies have been done in order to investigate the interaction between plasma and dust particles due to induced fluxes in crossed electric and magnetic fields [1, 2]. Most of these investigations used the Barnes formulation for the ion drag [3]. New insights in the importance of the local non-linearity of the ion scattering problem, as well as the importance of ion flow and ion-neutral collisions have resulted in new formulations for the ion drag force. This is the point addressed in chapter 5.

In order to get a better understanding of the importance of magnetic fields in dusty discharges, we performed experiments at the Plasma Sciences Laboratory of Auburn University in Auburn, Alabama. In this laboratory, we constructed a DC experiment with a mounted electromagnet. The next section discusses the experimental setup.

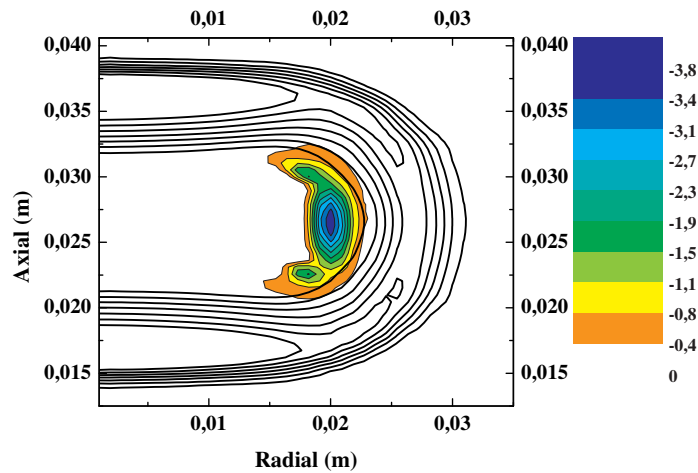


Figure 4.1: Calculation of the dust drift velocity in $cm\ s^{-1}$ for the discharge of chapter 3, with $B = 0.25\ T$. We see that the inside of the dust cloud (shown by the contour lines) rotates in the left-hand direction with respect to the central axis of the discharge. The maximum in rotation is mainly due to the high ion density on the inside of the dust cloud.

4.2 Device

We performed the experiments in the Dusty Plasma Experiment (DPX) device. The DPX device consists of two 100 mm diameter 6-way ISO 100 stainless steel crosses. In the first section plasma is created between two powered electrodes, the second section is used for pumping and gas feed [4]. Figure 4.2 shows a schematic of the device, together with the Particle Image Velocimetry (PIV) lasers, which will be described further on. The device has several ports to access the plasma with probes, and has several windows through which light coming from the plasma or laser light reflected by dust particles can be collected by a CCD camera.

In a typical experiment, we first pumped the vessel to a base pressure of less than 10 mTorr. Next, we opened the gas feed to allow argon gas to enter the vessel until a background pressure was reached of $P_{gas} \sim [100 - 300]$ mtorr, measured by a type DV-6 thermocouple gauge. Then, the electrodes were biased by two power supplies and an argon plasma was created. Typical values for the anode voltage and cathode voltage were $V_a \sim +100V$ and $V_c \sim -160V$ respectively, depending on the background pressure.

We then introduced an electrically floating tray from the bottom port, on top of which aluminum oxide (Al_2O_3) dust particles were placed. When the potential

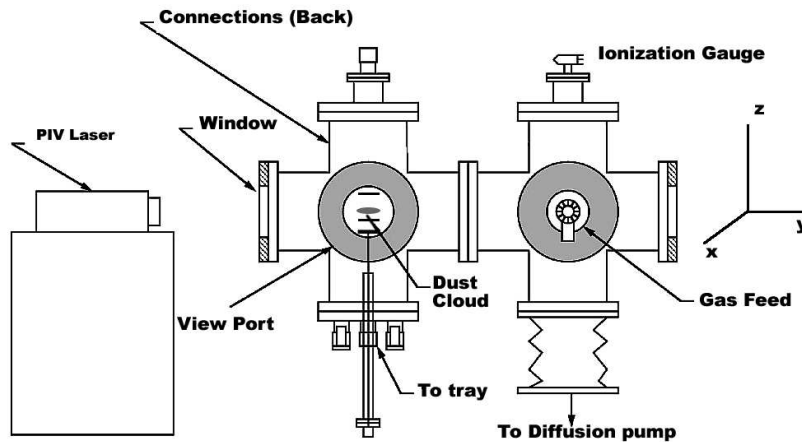


Figure 4.2: Schematic of the DPX experimental setup. Plasma is created in the left chamber between the negatively biased cathode (bottom) and the positively biased anode (top). Note that in the experiments discussed in this thesis, the dust cloud is suspended between the electrodes, whereas in [4] the electrodes were reversed and the dust cloud was suspended in the anode spot, below the positively biased anode. Figure adapted from [4].

difference was increased above a certain threshold potential, arcing occurred between the tray and the cathode, resulting in the ejection of dust particles from the tray into the plasma. The dust charged up and was suspended above the cathode by the different plasma forces.

To study the response of dusty plasma to a magnetic field, we installed an electromagnet inside the left chamber in two ways. In the first setup the magnet was installed on the back port, so that the magnetic field pointed along the x axis. A camera was mounted on the top window, with the direction of view in the $-z$ direction. In order to view the dust cloud, the anode was made from wire mesh, allowing the camera to focus through the wire mesh onto the dust cloud. This setup is schematically shown in figure 4.3 on the left-hand side.

If the main electric field at the position of the dust cloud balances the force of gravity, while dust particles obtain a negative charge, then the electric field must point downwards. The magnetic field in front of the magnet is roughly dipolar and was measured in the plane of symmetry of the magnet, using a portable Hall probe. We measured two components of the magnetic field (B_θ, B_z) and reconstructed the total magnetic vector for different heights above the magnet. A plot of the reconstructed magnetic field, measured in air, is shown in figure 4.4. We assume that the magnetic susceptibility of the plasma (and for air) is very small, $\chi_m^{pl} \ll 1$,

so that the magnetization of the plasma is small, $\mathbf{M}_{pl} \approx 0$. That way, the magnetic field in the plasma, \mathbf{B}_{pl} equals the magnetic field plotted, $\mathbf{B}_0 = \mu_0 \mathbf{H}_0$ ¹, since $\mathbf{B}_{pl} = \mu_0 (\mathbf{H}_0 + \mathbf{M}_{pl}) \approx \mu_0 \mathbf{H}_0 = \mathbf{B}_0$.

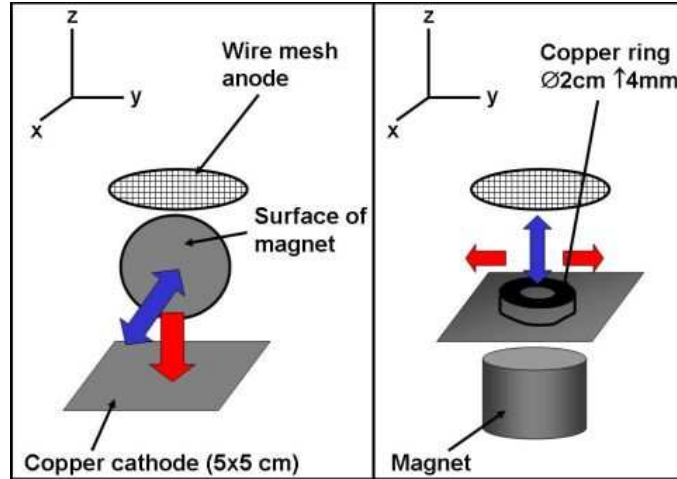


Figure 4.3: The two different setups used in the left chamber of the DPX device. In the first setup (left) the magnetic field points in the $\pm \hat{x}$ direction (blue arrow). We assume that the sheath electric field (red arrow) points in the $-\hat{z}$ direction. In the second setup (right) we attached a copper ring to the cathode and introduced the magnet from below. The radial electric field (red arrows) introduced by the ring, together with the vertical magnetic field (blue arrow) result in an azimuthal $\mathbf{E} \times \mathbf{B}$ direction.

The strength of the magnetic field could be adjusted by controlling the current through the magnet. Reversing the polarity of the applied potential (swapping the minus and plus pole) resulted in reversing the direction of the magnetic field. The strength of the magnetic field at different heights above the center of the magnet for different values of the applied potential is shown in figure 4.4 on the right hand side. It shows that the magnetic field varies linearly with the applied potential.

In the setup of figure 4.3 on the left hand side the dust cloud was suspended in a horizontal plane, near the edge of the cathode sheath and formed a thin pancake structure there. The electric field in the sheath is assumed to point downwards, towards the cathode. When the magnetic field vectors point away from the magnet in the $+\hat{x}$ direction, as in figure 4.4, the overall $\mathbf{E} \times \mathbf{B}$ direction in the horizontal plane, where the dust is suspended, is $(-\hat{x}, -\hat{y})$ in the left half, and $(+\hat{x}, -\hat{y})$ in the right half of the setup shown in figure 4.3. When the magnetic field is reversed, the $\mathbf{E} \times \mathbf{B}$ -direction is $(+\hat{x}, +\hat{y})$ in the left half and $(-\hat{x}, +\hat{y})$ in the right half.

¹The magnetic susceptibility of air at room temperature is $\chi_{air}^{T=293} = 0.38 \cdot 10^{-6}$, so $\mu_{air} \approx \mu_0$.

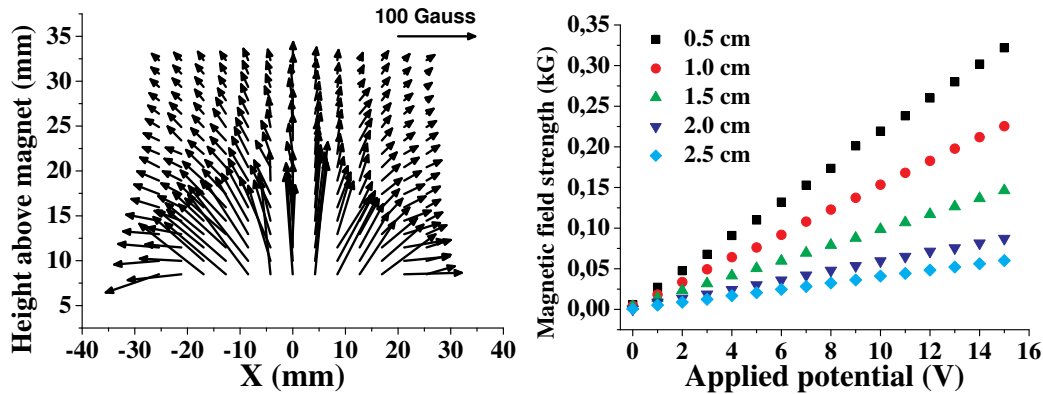


Figure 4.4: The magnetic field vectors in the symmetry plane of the magnet (left) measured using a Hall probe, and the magnetic field strength at different heights above the center of the magnet (right). We are grateful to John McKee at Auburn University for providing the latter measurement.

We used another setup, shown in figure 4.3 on the righthand side, in order to obtain an azimuthal $\mathbf{E} \times \mathbf{B}$ drift, similar to the experiments in [1]. In order to achieve this, we attached a copper ring to the cathode. This ring introduces a large radial component of the electric field to the sheath electric field. The magnetic field points vertically, either in the $+\hat{z}$, or the $-\hat{z}$ direction. The resulting $\mathbf{E} \times \mathbf{B}$ direction is in the $\pm\theta$ direction.

In order to qualitatively and quantitatively determine the response of dusty plasma formed in the DPX device to the applied magnetic field, we used different diagnostics to determine the plasma properties and measured the movement of the dust. The diagnostics and the measured plasma properties are presented in the next section.

4.3 Diagnostics

We used two types of probes and two types of optical video capture systems during the experiments. Probes typically have a small piece of metal exposed to the plasma. The first type of probe we used is called a Langmuir probe [5]. This is a small piece of graphite attached to a power source. We controlled the potential of this piece of graphite and measured the current from the plasma to the probe. The second type of probe is an emissive probe [6, 7]. This is a piece of tungsten connecting two electrically conducting wires. The tungsten is exposed to the plasma. We send a current through the loop and measured the potential. These measurements give information about plasma densities and the electron temperature, by directly giving the plasma and floating potential.

The different optical systems consist of a (digital) camera which either collects light emitted by the plasma, or laser light reflected by dust particles suspended in the plasma. We used a 30 Hz full color camera together with a stationary red diode laser, as well as a 15 Hz black and white camera connected to a PIV laser system. The latter system allows us to follow the transport of dust through the plasma at distinct time intervals. We now shortly describe the principle of the diagnostics used.

4.3.1 Langmuir probe

We constructed a Langmuir probe and introduced it through a port on the far right side of the DPX device, through the gas feed chamber and into the plasma chamber. It consists of a long graphite wire surrounded by a ceramic housing. The wire is approximately 1 mm thick. A 4 mm long part extends out of the ceramic housing and is exposed to the plasma. The other end of the graphite wire exits the vacuum-sealed end of the probe and is connected to a power supply. The probe is inserted off-axis. By rotating the port and by retracting the probe horizontally, we are able to measure at different positions in the plasma chamber. A schematic of the probe is shown in figure 4.5.

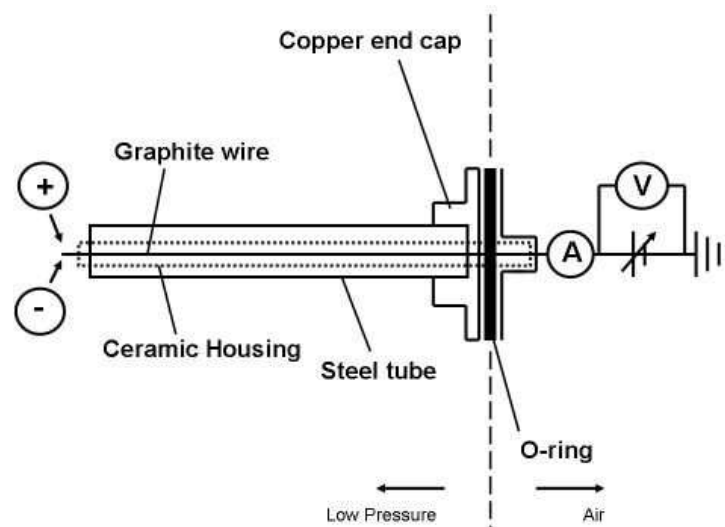


Figure 4.5: A small piece of graphite is exposed to a plasma. The potential of the graphite surface is controlled by the power supply. The probe will collect ions and electrons from the plasma. The collected current is measured as a function of the potential applied to the probe.

When the probe is biased very negatively with respect to the plasma potential,

it repels electrons and attracts ions. For increasing potential, energetic electrons can overcome the repelling potential of the probe and the current decreases. When the applied potential equals the floating potential at the position of measurement in the plasma, no net current will be collected by the probe. Therefore, the point where the current equals zero is a good indication of the floating potential. For increasing applied potential more and more electrons will be attracted by the probe, while less and less ions are able to reach the positively biased, repelling probe. When the probe is very negatively biased, a maximum amount of ions can be collected from the plasma. This is called the ion saturation current. When the probe is very positively biased the current saturates to the electron saturation current.

Figure 4.6 shows a typical Langmuir trace we obtained during the experiments. From this graph the floating potential is measured to be approximately 86 V. An estimate for the ion saturation current is $-0.14\mu\text{A}$. The graph shows how the current suddenly becomes very negative for very negative bias potentials with respect to the floating potential. This may be caused by sputtering of the probe by positive ions gaining a large amount of energy in the attractive potential around the probe, especially at high neutral pressures [8]. No further experiments were done to investigate this effect.

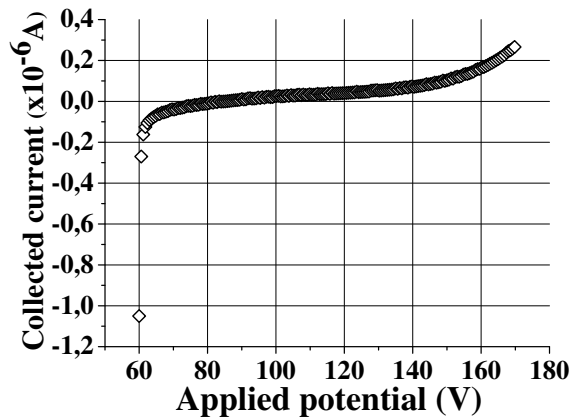


Figure 4.6: Measured Langmuir trace. We estimate the floating potential at 86 Volts from the point where the net current is 0. From the slope at that point we estimate the ion saturation current, the current for very negative bias potential with respect to the floating potential, at $-0.14\mu\text{A}$. The sudden drop in current around 60 Volts (-26 Volts with respect to the floating potential) might be due to sputtering of the probe by energetic ions.

During the Langmuir probe measurements, we did not acquire a good estimate for the plasma potential. We need to know the obtained floating potential with respect to the plasma potential and not with respect to the laboratory ground to

calculate the dust charge. Therefore, we used an emissive probe, both passive as well as equipped with an operational amplifier.

4.3.2 Emissive probe

An emissive probe looks very similar to a Langmuir probe, however in this case two graphite wires are introduced in a ceramic housing. The two wires are connected by a tungsten wire, which is exposed to the plasma. This way a closed circuit is formed. A schematic is shown in figure 4.7.

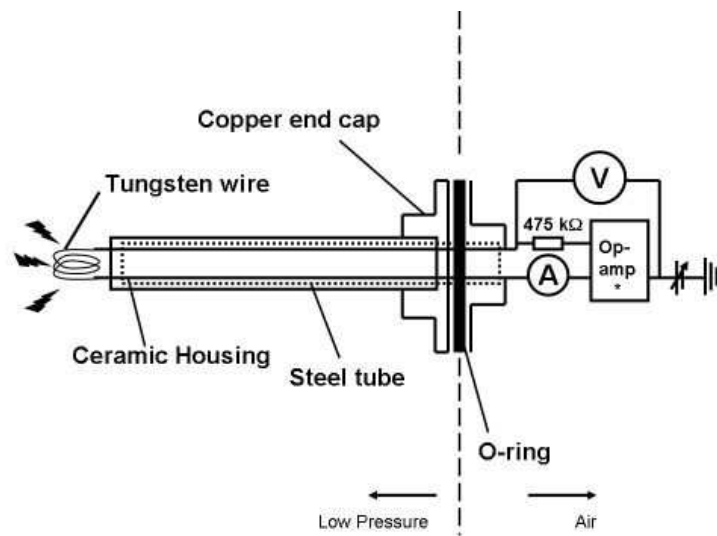


Figure 4.7: A small tungsten wire is exposed to the plasma. It forms a closed loop with two graphite wires. When a current is sent through the wire, the tungsten heats up and emits electrons. By emitting electrons the potential of the tungsten wire increases. An emissive probe with an OP-AMP can measure the floating potential at zero current. A passive emissive probe measures ground at that current.

When a current is sent through the closed circuit, the tungsten starts to heat up. At some point it starts to emit light and electrons, and the potential measured over the tungsten wire rises. As long as the potential with respect to the surrounding plasma potential is negative, the electrons escaping from the tungsten are not easily replaced by electrons coming from the plasma. When the potential on the tungsten equals the local plasma potential, electrons collected from the plasma will balance the electrons emitted by the tungsten and the current saturates. The potential at the point where the measured current saturates, is therefore a measure of the plasma potential. An active emissive probe, with an operational amplifier

(OP-AMP) included in the circuit measures the floating potential directly at zero current.

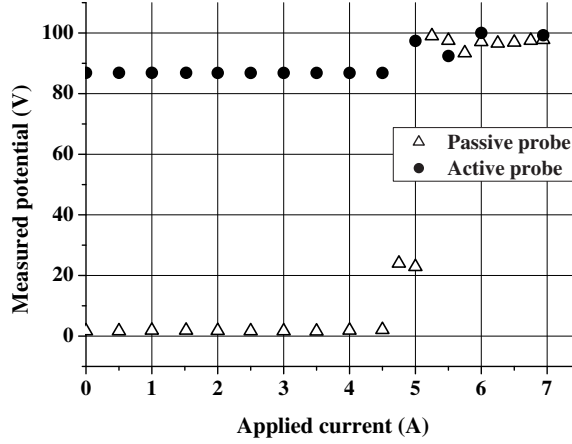


Figure 4.8: The measurements with both the passive as well as the active emissive probe show that the plasma potential is approximately 99 Volts. The active emissive probe confirms the value of the floating potential around 86 Volts.

The results for both the passive and active emissive probe are shown in figure 4.8. It confirms the value of the floating potential at approximately 86 Volts. The plasma potential is measured at 99 Volts. Therefore, the floating potential in fact reads -13 Volts with respect to the surrounding plasma.

From the measurements done with the probes, several plasma parameters can be estimated, the electron temperature T_e , the plasma density $n_{e,+}$ assuming quasi-neutrality, and the dust charge in electrons. The first follows from the floating potential with respect to the plasma potential ($V_F - V_P$) [9],

$$\frac{e(V_F - V_P)}{T_e} = \frac{1}{2} \left[\ln\left(2\pi \frac{m_e}{m_+}\right) - 1 \right]. \quad (4.10)$$

m_+ is the mass of the argon ion. Using the values measured we estimate the electron temperature to be $T_e \approx 2.5$ eV.

The plasma density can be found from the ion saturation current. This current is given by the Bohm flux ($en_{+,s}v_B$) times the surface of the sheath around the Langmuir probe tip A_s ,

$$I_{is} = eJ_{is} = eA_s n_{+,s} v_B = eA_s n_{\infty} \exp(-1/2) \sqrt{\frac{eT_e(\text{eV})}{m_+}}. \quad (4.11)$$

Using the electron temperature we found from the potential measurements, we find a plasma density $n_\infty \approx 4.4 \cdot 10^{13} m^{-3}$. Here we assumed that the surface of the sheath around the probe tip can be approximated by the actual surface of the tip, which is a tiny cylinder of length 4 mm and a diameter of 1 mm.

The dust charge can be estimated assuming that the floating potential measured would be the equilibrium potential of the dust particles once they are positioned there. The floating potential is then connected to the dust particle charge through the capacitor model for the dust particle (see section 2.2.4),

$$\phi_d = V_F - V_P = \frac{-eZ_d}{4\pi\epsilon_0 r_d}. \quad (4.12)$$

The dust particles we use have a diameter of 1.2 μm . The charge is then approximately -5400e. OML theory gives approximately -4000e. Therefore $Z_d \sim [4000 - 5400]$.

4.3.3 Camera and PIV system

Micrometer sized dust particles introduced in the plasma can be made visible by irradiating them with a laser. The dust particles will scatter the laser light, which can then be collected by a CCD camera. We used two different systems. The most simple one consisted of a 30 Hz full color camera, together with a low power stationary red diode laser. With the full color camera we were able to simultaneously capture the light coming from the plasma, and the red laser light being reflected by the dust simultaneously.

The second optical system is somewhat more involved. In the PIV system two frequency doubled Nd-YAG lasers (25 mJ, 532 nm) fire shortly after each other, separated by a time interval $0.0005 \text{ ms} \leq \Delta t \leq 30 \text{ ms}$. The consecutive shots are repeated at a 15 Hz frequency. The lasers are coupled to a CCD camera in such a way that the shot of the first laser is collected by the first frame of the camera and the shot of the second laser is collected by the second frame. This technique is called "frame straddling".

In a statistical model, the separate frames are divided into 64×64 boxes and using cross-correlation techniques, the movement of all the particles in the interrogation boxes is determined. This way, displacement vectors are derived for the movement of large numbers of particles. The two-dimensional velocity profile inside the illuminated part of the dust cloud can then be obtained.

Unfortunately, the alignment of the two lasers turned out to be insufficient to obtain acceptable velocity profiles. However, we could still use the data collected by one of the two laser shots. This would give us a detailed picture of the dust transport in time intervals of 1/15 s, since the laser intensity was much higher than the diode laser intensity *and* the PIV camera was fitted with a macro lens,

allowing us to zoom in much further on the dust cloud. A disadvantage is that the plasma glow could not be detected at the same time. A detailed description of the (stereoscopic) PIV laser setup and the DPX device can be found in [4, 10, 11, 12, 13]. We now turn to the results.

4.4 Plasma and particle response

4.4.1 Setup 1 – Plasma response

The response of the plasma to an applied magnetic field in setup 1 is shown in figure 4.9. We can see two distinct glows. The bright glow is near the wire mesh anode and is due to sharp points and edges on the surface of the wire mesh and the supporting ring around the wire mesh. Sharp points locally create large electric fields, resulting in acceleration of electrons, increasing the excitation and ionization. This is then seen as an increase in the light emission.

The diffuse glow is the large volume plasma glow near the cathode sheath. This plasma glow is situated in front of the magnet at approximately 0.5-1.5 cm from the magnet surface. The magnetic field strength there is approximately 100-300 Gauss, since we usually kept the potential of the magnet power supply at around 10-12 V, see figure 4.4.

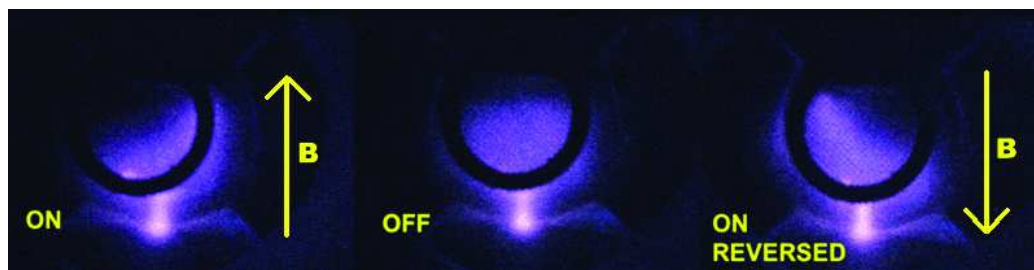


Figure 4.9: Three frames taken from the top port with the full color camera. The black ring is the support ring for the wire mesh anode. The magnet is mounted on the topside of these pictures, facing down. The direction of the magnetic field is indicated by the yellow arrows. The center figure shows the plasma glow without magnetic field. When the magnet is turned on, a clear response of the plasma glow is observed, consistent with the $\mathbf{E} \times \mathbf{B}$ direction.

The figure shows the diffuse glow of the bulk plasma in front of the cathode, which shifts when the magnetic field is turned on. The electric field at the position of the plasma glow is the sheath electric field in front of the cathode, which points downwards (pointing into the paper in figure 4.9). The direction of the shift in

the plasma is then consistent with the $\mathbf{E} \times \mathbf{B}$ direction in this electric field and the dipolar magnetic field of the magnet.

The positive ions in the discharge are not magnetized. The ion cyclotron frequency $\nu_{c,+} = \omega_{c,+}/2\pi = 0.38\text{-}1.14 \cdot 10^4$ Hz, whereas the ion-neutral collision frequency is approximately [14] $\nu_{m,+} = 1,7 \cdot 10^6$ Hz. Because $\nu_{c,e} = 2.8\text{-}8.4 \cdot 10^8$ Hz, and the electron-neutral collision frequency is $\nu_{m,e} = 5.9 \cdot 10^8$ Hz, the electrons are just magnetized.

Between collisions electrons will gyrate around magnetic field lines and slowly drift in the $\mathbf{E} \times \mathbf{B}$ direction. This causes the difference in glow. The plasma as a whole shifts to a new equilibrium position when the magnetic field is turned on and off, in the $\mathbf{E} \times \mathbf{B}$ direction.

4.4.2 Setup 1 – Particle response

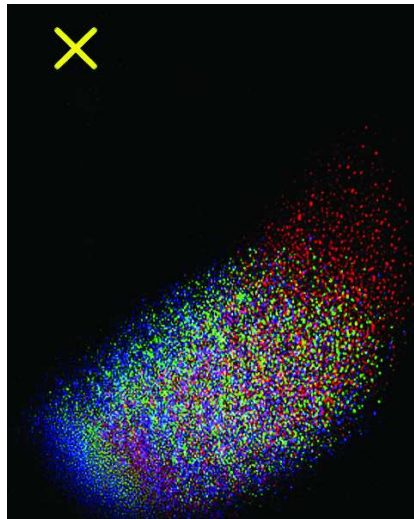


Figure 4.10: Three frames taken in the setup as in the rightmost picture of figure 4.9 shown overlaid. The yellow cross indicates the position of the center of the cathode. The first frame is indicated by the red, the second by the green, the third by the blue. The response of the dust particles is in the same direction as the change in the plasma glow. Note that the initial response, between the red and the green frame, seems to be more pronounced than the response of the dust between the green and the blue frame.

Dust particles were introduced into the plasma chamber and the response to the magnetic field was recorded using the PIV laser system with the PIV macro camera mounted on the top port. Three frames taken after the first shot of the PIV

laser are combined in figure 4.10. The red color is the first shot, green the second and blue the third. Between every shot was a time interval of 0.133 seconds. The orientation is the same as in figure 4.9, however a smaller part is shown, since we have zoomed in. The yellow cross indicates the center of the cathode.

The shift of the dust particles coincides with the shift of the plasma, that is in the $\mathbf{E} \times \mathbf{B}$ direction. Also note that the shift between the first and the second shot (red to green) is much bigger than the shift between the second and third shot (green to blue). This was repeatedly observed and will be discussed later.

4.4.3 Setup 2 – Plasma and particle response

In setup 2 we used the full color camera to look simultaneously at the plasma as well as the particle response. This camera collected both the light emitted by the plasma, as well as laser light scattered by the dust particles immersed in the plasma. As a laser we used a simple red diode laser. Using cylindrical lenses the laser beam is expanded in a thin (thickness ~ 1 mm) vertical sheet. The capture rate of the camera is 30 frames per second.

Using this configuration, we looked at the response of the plasma and the dust particles simultaneously, when a change in the magnetic field configuration occurred. In figure 4.11, ten consecutive frames are shown, after inverting the colors and enhancing the images. The black streaks are dust clouds. The grey color represents the plasma glow. The black square indicates the position of the ring attached to the cathode. The outer diameter of this ring is 20 mm, the inner diameter 16 mm. The height of the ring is 4 mm. In frame 1, the magnetic field was on, pointing upwards. It was then turned off.

From the images we can conclude the following. There is a clear change in both the plasma glow, as well as in the position of the dust clouds. The change in plasma glow seems to take approximately three frames. The dust response seems to consist of two distinct parts. First, there is a quick response to the change in plasma glow, which can be seen in frames 1, 2, 3 and 4. Once the plasma has settled however, there is very little change to be observed in the position of the dust particles. The transport of dust seems to be much slower from frame 5 and onwards.

Apparently, there is dust transport connected to the direct change in the plasma parameters, and slower transport when the plasma is at its equilibrium position. This difference in the response of dust particles to a change in the plasma was also observed in [4]. In that experiment a sudden pulse was applied to the electrodes, to cause a perturbation of the plasma potential. They also observed a fast initial response of the dust to the perturbation, followed by a secondary slow response. The reported velocities, i.e. $\sim cm s^{-1}$ in the initial phase and $\sim mm s^{-1}$ in the later phase, correspond well to the velocities we estimate in both phases, ~ 2

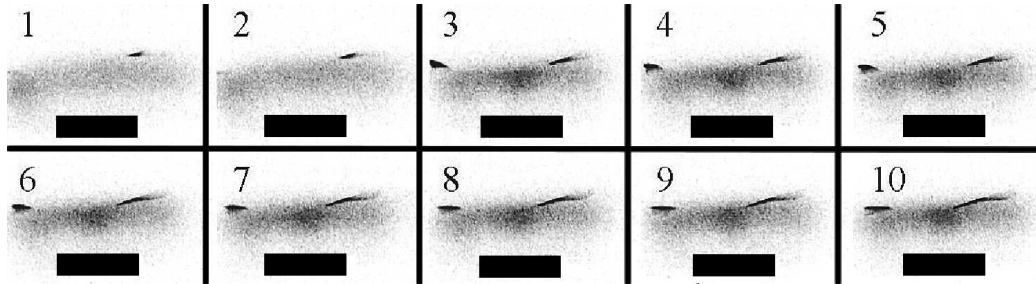


Figure 4.11: A greyscale figure of 10 frames of a movie made with the full color camera, after converting the colors. The black plumes is laser light scattered by dust particles, the lighter grey plasma glow. The first frame starts approximately when the magnetic field (pointing up) is turned off. The black squares mark the ring attached to the cathode.

$cm\ s^{-1}$ and $\sim 8.5\ mm\ s^{-1}$ respectively.

The fact that the plasma response can be distinguished to take about 3 frames, or roughly $0.1\ s$ is an interesting observation on itself. The time τ_{it} it takes an ion to cross the potential drop, V_c , in front of the cathode, called the ion transit time, is given by [15]

$$\tau_{it} = \left(\frac{eV_c}{k_B T_e} \right)^{3/4} \omega_{p,+}^{-1}, \quad (4.13)$$

where $\omega_{p,+} = \sqrt{e^2 n_+ / \epsilon_0 m_+}$ is the ion plasma frequency. Assuming that V_c approximately equals the potential applied to the cathode [16], we find for the ion transit time, $\tau_{it} \approx 1.64 \cdot 10^{-5} s$. This timescale is much shorter than the time scale observed in figure 4.11.

When the magnetic field is turned off, the electrons will immediately respond, but the ions can not respond to this instantaneous change in electron density because of their high mass. This causes a charge separation, slowing down the electrons, and speeding up the ions. Assuming that the potential jump roughly equals the electron temperature, over a distance of roughly a centimeter (estimated from the video-frames), we can make a guess for the mobility and diffusion coefficient of the ions. Since $\mu \propto L^2 / \Delta V \tau$, we estimate $\mu \approx 10^{-4} / (2.5 \times 3/30) \sim 4 \cdot 10^{-4} m^2 V^{-1} s^{-1}$. In a similar way, we can find the diffusion coefficient as: $D \sim L^2 / \tau \sim 10^{-3} m^2 s^{-1}$. The diffusion coefficient corresponds reasonably well to the diffusion coefficient for argon at 100 mtorr neutral pressure, even though it is off by factor of two.

We then postulate that the initial fast response of the dust is induced by ions diffusing to their new equilibrium position, following the change in electron den-

sity in the plasma after switch-off of the magnet. This initial response would then be an ion drag force, during a short time. This fast response is then followed by a longer and slower dust transport, because of the large inertia of the dust and the neutral drag force.

In order to get a better understanding of the plasma in front of the cathode, we used the emissive probe to measure the plasma potential. The final section deals with these results. These measurements together with observations of waves in the dust cloud in its final equilibrium position seem to indicate an important role for the ions in the equilibrium force balance.

4.5 Measurements on dust cloud at equilibrium position

The plasma potential measured with the emissive probe above the ring and cathode is shown in figure 4.12. From these measurements it can clearly be seen how the vertical electric field changes sign from pointing downwards outside of the ring to pointing upwards inside and above the ring. The dust cloud in equilibrium is suspended above the ring. The negative charge of the dust means that the electric field above the ring would pull them down towards the cathode. Since gravity also points downwards, another force must act on the particles, pushing them up. The most likely explanation would involve the ion drag force.

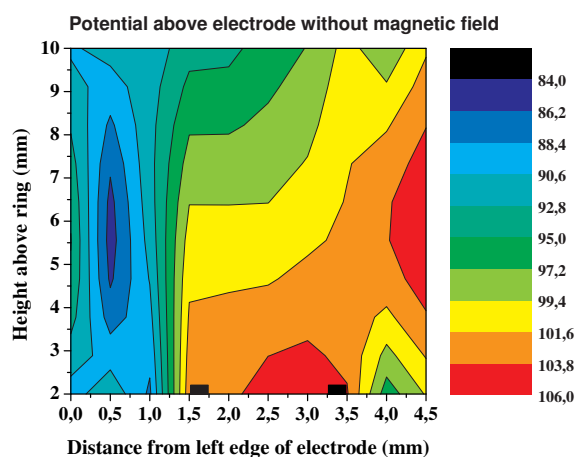


Figure 4.12: The plasma potential above the cathode in setup 2, measured with the emissive probe. The height is measured from the top of the ring, the black squares indicate the position of the ring.

The dust cloud in the final equilibrium position was measured with the PIV system. Waves were observed running in the dust cloud. From the measurements at distinct time-intervals we tried to measure the direction of propagation of the waves. Even though at dust-plasma boundaries waves are reflected, we obtained several consecutive frames from which we could observe the wave propagation. Such waves were also observed in the DPX device before and were reported in [4, 10] and are a general feature of DC discharges. In these experiments the dust cloud was suspended below the anode and the propagation of the dust acoustic waves was downward *away from the anode*. Several excitation mechanisms for these waves are proposed, one of which is an instability due to streaming ions [17].

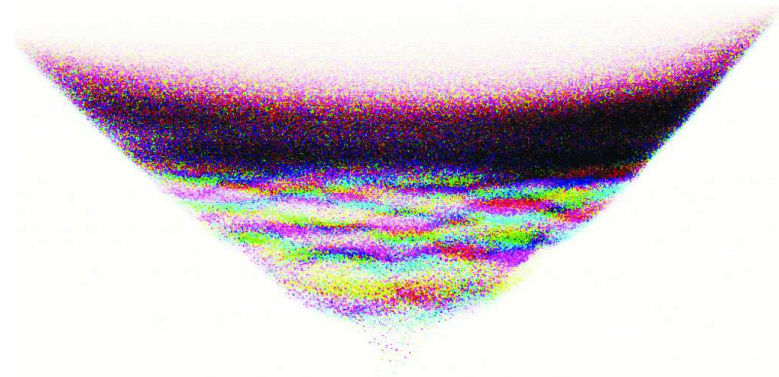


Figure 4.13: The dust cloud in equilibrium. Three consecutive frames taken with the PIV system are overlaid, colored blue-pink-yellow, approximately 0.2 seconds apart.

From the figure we can see that there are waves running up from the lower point, which is closest to the ring on the cathode. The width of the cloud corresponds reasonably well with the width of the ring attached to the cathode, showing that the dust fills the potential structure above the ring. Using the linear dispersion relation for dust acoustic waves, which relates the phase velocity to the dust density and charge [4],

$$v_{ph}^2 = \frac{k_B T_+}{m_D} \frac{n_D}{n_+} Z_D^2, \quad (4.14)$$

and using the value for Z_D derived above, together with the phase velocity derived from the frames in figure 4.13, 5 mm s^{-1} , we find for the dust density $n_D \approx 10^7 - 10^8 \text{ m}^{-3}$, which is the average value for the lower part of the dust cloud. In the dark band above the density is much higher. In fact no waves were observed there. The value of the dust density, together with the obtained dust charge gives

a value for the *Havnes parameter*, $\mathcal{P} = n_D Z_D / n_e \sim 10^{-2}$ in the region where the waves are running. In the dark band above this region, the electron depletion could be much higher, resulting in $\mathcal{P} \sim 0.1$ or even $\mathcal{P} \sim 1$.

From the observed waves it seems plausible that above the ring, ions are accelerated from the cathode/ring towards the dust cloud. The ions impinging on the dust particles then induce an ion drag force to balance the downward electrostatic acceleration and the force of gravity. From the derived dust charge, figure 4.12 and the mass, we can derive the magnitude of this force;

$F_{ion} \geq m_D g + e Z_D \times (\Delta V / \Delta z) \sim 2.2 \cdot 10^{-14} + 1.5 \cdot 10^{-12} = 1.5 \cdot 10^{-12} N$. This value for the ion drag force seems acceptable. We also find such values in our modelling results of RF discharges in chapter 5.

4.6 Conclusions

The experiments indicate that both plasma as well as dust particles respond to an applied magnetic field by a drift in the $\mathbf{E} \times \mathbf{B}$ direction. The dust response consists of two parts, an initial fast response on a short timescale, which seems to indicate a role of ions, possibly an induced ion drag. The final response takes much longer, typically seconds. This is most likely due to the inertia of the dust and the neutral drag force.

Using all diagnostics, we determined the plasma densities, $n \sim 4.4 \cdot 10^{13} m^{-3}$, the electron temperature $T_e \sim 2.5 eV$, the dust charge number $Z_D \sim 4000-5400$ and the lower limit of the dust density $n_D > 10^7 - 10^8 m^{-3}$.

Measurements with the emissive probe and measurements on dust acoustic waves with the PIV system, indicate that the electric field in setup 2, above the ring attached to the cathode, points away from the cathode/ring. This implies that the force keeping the dust in place is the ion drag force. The necessary value for this force $F_{ion} \sim 1.5 \cdot 10^{-12} N$.

References

- [1] U. Konopka, D. Samsonov, A. V. Ivlev, J. Goree, V. Steinberg, and G. E. Morfill, *Phys. Rev. E* **61**, 1890 (2000)
- [2] K. Matyash, M. Fröhlich, H. Kersten, G. Thieme, R. Schneider, M. Hannemann, and R. Hippler, *J. Phys. D: Appl. Phys.* **37**, 2703-2708 (2004)
- [3] M. S. Barnes, J. H. Keller, J. C. Forster, J. A. O'Neill, and D. K. Coultas, *Phys. Rev. Lett.* **68**, 313 (1992)
- [4] E. Thomas, Jr. and M. Watson, *Phys. Plasmas* **6**, 10, 1999
- [5] H. M. Mott-Smith and I. Langmuir, *Phys. Rev.* **28**, 727 (1926)
- [6] I. Langmuir, *Phys. Rev.* **33**, 954 (1929)
- [7] R. E. Kemp and J. M. Sellen, Jr., *Rev. Sci. Instrum.* **37**, 455 (1966)
- [8] N. Hershkowitz and M. H. Cho, *J. Vac. Sci. Technol. A* **6**, 2054 (1988)
- [9] I. H. Hutchinson, *Principles of Plasma Diagnostics*, (Cambridge University Press, Cambridge, 1990)
- [10] E. Thomas, Jr. and R. L. Merlino, *IEEE Trans. Plasma Sci.* **29**, 152 (2001)
- [11] E. Thomas, Jr., *Phys. Plasmas* **9**, 17 (2002)
- [12] E. Thomas, Jr., B. M. Annaratone, G. E. Morfill, and H. Rothermel, *Phys. Rev. E* **66**, 016405 (2002)
- [13] E. Thomas, Jr., J. D. Williams, and J. Silver, *Phys. Plasmas* **11**, L37 (2004)
- [14] A. D. Richards, B. E. Thompson, and H. H. Sawin, *Appl. Phys. Lett.* **50**, 492 (1987)
- [15] D. Arbel, Z. Bar-Lev, J. Felsteiner, A. Rosenberg, and Ya. Z. Slutsker, *Phys. Rev. Lett.* **71**, 2919 (1993)

- [16] S. J. Choi, M. J. McCaughey, T. J. Sommerer, and M. J. Kushner, *Appl. Phys. Lett.* **59**, 3102 (1991)
- [17] V. E. Fortov, A. G. Khrapak, S. A. Khrapak, A. P. Nefedov, O. F. Petrov, and V. M. Torchinsky, *Phys. Plasmas* **7**, 1374 (2000)

5. Large-angle scattering, ion flow speed, ion-neutral collisions and the ion drag force

Abstract. *The ion drag force is one of the most important forces acting on dust particles in a dusty plasma. The first expressions for this force were derived for a single dust particle placed in a collisionless plasma, without flow. Recent theories show deviations from these expressions when there are ion-neutral collisions and a significant ion flow. Experiments have until now only shown a small deviation from the standard expressions, however.*

We extended our fluid dusty plasma model to include recent theories for the calculation of the ion drag force, including the effect of non-linear ion scattering, ion flow and ion-neutral collisions. A change in the dust charge due to these collisions is also considered.

Inside the dust-free void, non-linear scattering is very important. In the dust cloud the effect is only moderate. Ion flow speeds are typically low, except near the electrodes. Thus, the effect of the ion flow speed is small. Only near the outer walls does the screening length become much larger than the ion mean free path and is the ion drag force increased by collisions. The dust charge does change with increasing ion flow.

When we compare our model with experiments, we conclude that large-angle scattering is important and the velocity dependent linearized Debye length is the appropriate screening length. Using small-angle scattering with the electron Debye length actually overestimates the ion drag, resulting in inconsistent values of the electric field and the ion drift speed.

Based on :

New Journal of Physics, **8**, 8 (2006)

Authors :

V. Land, W. J. Goedheer

5.1 Motivation

The three most important forces for dusty plasmas under micro-gravity are *neutral drag*, *the electrostatic force* and *the ion drag* (and the mutual interaction between the charged dust particles), because the thermophoretic force is usually much smaller [1, 2]. It is intriguing to realize that none of these forces is completely understood either theoretically or through experiments in a flowing, collisional plasma.

For the neutral drag, the Epstein formulation is generally used [3]. It describes the interaction of neutral particles with hard spheres. The momentum transfer by the neutral particles to the spheres during collisions depends on the way they reflect from the spheres. Usually, specular reflection is assumed, which is similar to the way light reflects from a smooth surface.

Experimentally, it is concluded in [4] that the neutral drag force corresponds well with this formulation, but in [5, 6] the neutral drag force is found to be smaller than the value given by the Epstein formulation for specular reflection. It should be noted that in [5] the mass of the dust particles is underestimated by almost an order of magnitude (for aluminum dust particles, with a mass density of 2.7 g cm^{-3} and a radius of $0.6 \text{ }\mu\text{m}$, we find a mass of $\approx 2.5 \times 10^{-15} \text{ kg}$ instead of the reported $2.5 \times 10^{-16} \text{ kg}$), which results in errors in the analysis.

The electrostatic force depends on the dust charge. Normally, the charge on a dust particle in a plasma is calculated using Orbital Motion Limited theory (OML) [7]. This theory gives the electron and ion current to a charged dust particle. In equilibrium these currents are equal and the dust charge can then be calculated. Even though this theory depends on many assumptions, a Particle-In-Cell (PIC) model [8], shows remarkable good agreement with OML theory, again for a *collisionless* flowing plasma. However, it is only used in the limiting cases of dust particle radii much smaller than the ion Debye length, or in the case of a plasma with equal ion and electron temperature.

Khrapak et al. show experimentally that collisions can dramatically reduce the charge on dust particles in a plasma [9]. This is caused by an increase in the ion current to the dust particle due to charge-exchange collisions. They also give a theoretical calculation of the ion current in the presence of these collisions based on [10].

The ion drag force strongly depends on the shielding of the dust particle by plasma particles and thus on the potential distribution around the dust particle. In a dusty plasma, the dust particle is the heaviest species. The scale length over which the potential around a dust particle vanishes is then some function of both the electron as well as the ion Debye length.

The ion drag also depends on the ion flow speed [11]. Large ion flow speeds cause a strong anisotropy in the ion distribution around the dust particle, which

causes a strong anisotropy in the shielding of the dust particle. Furthermore, the ion speed determines the size of the Coulomb radius around a charged dust particle. This length scale plays an important role in the scattering of ions, as will be shown.

Finally, collisions of ions with neutrals change the ion drag force [12, 13] in a similar way as collisions change the dust charge; particles outside the solid angle of particle-scattering or particle-capture enter the solid angle after a collision, which increases the ion drag force acting on a dust particle.

Different experimental determinations of the ion drag force in complex plasmas [14, 15, 16] give ambiguous answers and usually can be explained by both the original approach of Barnes *et al.* [17] as well as the more recent theoretical description [11], which has led to many discussions e.g. [18, 19].

Since we can self-consistently model dusty plasmas under micro-gravity for different experimental settings, we are able to investigate the importance of different ion drag models and to compare them with experiments. This chapter reports our findings.

5.2 Results for different models

We compare the dust transport for different models. We begin by briefly showing the results with the approach by Barnes *et al.* (small angle scattering) and then compare them with the results obtained by using the approach of Khrapak *et al.* (large angle scattering). In all the following results, we modelled an argon discharge at 40 Pa background pressure and at a 100 Volt peak-to-peak applied potential. The geometry is similar to the geometry of the PKE chamber [20]. We introduced 1 million dust particles with a radius of $6.8 \mu\text{m}$. In the experiments, dust particles were introduced through two shakers in the electrodes. In our model, we add source terms for the dust particles at the same positions, simulating the injection of the dust particles into the plasma from the electrodes.

5.2.1 Small angle scattering and large angle scattering

Figure 5.1 shows the final dust densities for the Barnes approach with the linearized Debye length as the cut-off radius (left) and the Barnes approach with the electron Debye length (right), see equation 2.50. Similar results were also shown in [1, 2], where the ion drag force was enhanced by a factor of 5, instead of using the electron Debye length as the cut-off length. Even though these results are not new, they do teach us one important thing; apparently, *the fact that the void does not appear, implies that the momentum transfer cross section for ion-dust collisions should be larger than that calculated using the Coulomb scattering theory*

with the linearized Debye radius as the upper limit for the impact parameter. The ion drift itself is not sufficient to produce a void.

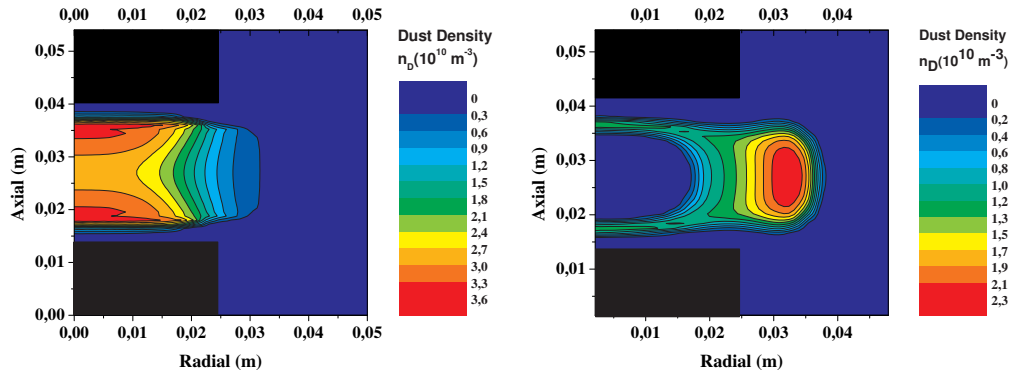


Figure 5.1: **Left:** The final dust density profile when the ion drag force is calculated with the Barnes logarithm and the *linearized Debye length* as the cut-off radius in equation 2.50. Clearly, no void is formed.

Right: Same as on the left, but now calculated with the Barnes logarithm and the *electron Debye length* as the cut-off radius in equation 2.50. Clearly, this increases the ion drag force in the bulk of the discharge enough and a dust-free void is formed.

The electron Debye length is not a physical cut-off length for the potential around very negatively charged dust particles. Therefore Khrapak *et al.* included non-linear scattering into the linear framework. They introduced a parameter, $\beta(v)$, which depends on the dust charge, the ion flow and the linearized Debye length, $\beta(v) = \rho_0(v)/\lambda_D(v)$, as explained in section 2.3.3. When this parameter is large, ion scattering in the potential becomes non-linear within the screening length, which enhances the scattering cross-section.

Figure 5.2 shows this parameter calculated self-consistently in our model for the final dust density profile shown in the right frame of figure 5.1. We see that inside and near the edge of the void, $\beta(v) > 1$, which means that the Barnes form of the logarithm is no longer valid, as discussed in section 2.3.3. Of course, inside the void no dust particles are present, so the effect of scattering of ions beyond $\lambda_D(v)$ is only important near the edge of the void for the dust cloud observed in our simulations. However, for a dust particle introduced in the void the ion drag force is such that it will still be accelerated out of the void and in that case scattering beyond the screening length is important.

When we look at the final dust density profile calculated with the Khrapak form of the ion drag, shown in figure 5.3 on the left, we indeed see a change in the shape of the void around the quasi-neutral bulk of the discharge. The final

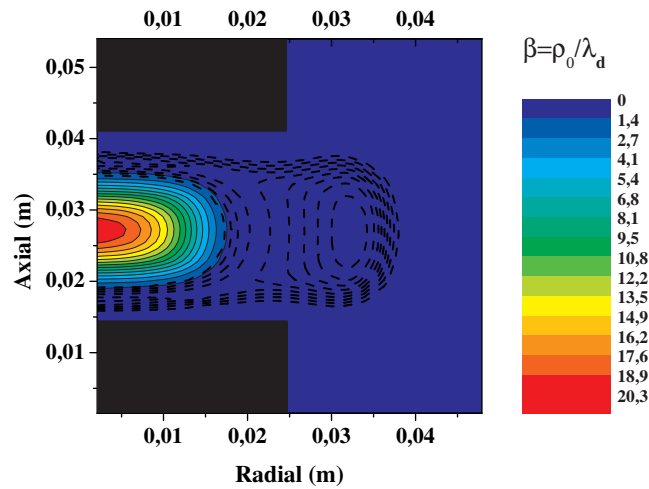


Figure 5.2: The parameter measuring the importance of scattering beyond the linearized Debye length (large angle scattering), as discussed in section 2.3.3. For $\beta > 1$, this scattering is important. The dashed lines correspond to the dust density contours from figure 5.1. Scattering beyond λ_D seems to be important only inside the void or near the void edge.

size of the void is somewhat smaller and the void has a more rectangular shape. The density gradients near the edges of the void are steeper than in the case of the calculation with the Barnes approach, which indicates a narrower potential well around the point of force balance. The importance of large angle scattering is shown in figure 5.3 on the right. Inside the dust cloud the value of $\beta(v)$ is moderate. Inside the void however $\beta(v) \gg 1$.

The total force (ion drag + thermophoretic + electrostatic) in the radial direction, at the axis of symmetry ($Z=0.027$ m), two seconds after the first dust was added to the discharge, is shown in figure 5.4. It shows the force for the Barnes approach with the linearized Debye length, where no void is formed (dashed line). Inside the bulk, $\beta \gg 1$, so the ion drag force calculated with the approach by Khrapak with the linearized Debye length (dotted line) is larger than the ion drag force calculated with the approach by Barnes with the electron Debye length (solid line). However, β drops to smaller values rapidly for increasing radial position, and in that case the approach by Barnes with the electron Debye length can overestimate the ion drag force, especially for larger particles, as was also mentioned and shown in [16, 18]. Another important observation is that the void edge does not correspond to the point where $F_r = 0$. However, figure 5.4 does not include the mutual interaction force between the charged dust particles, which prevents

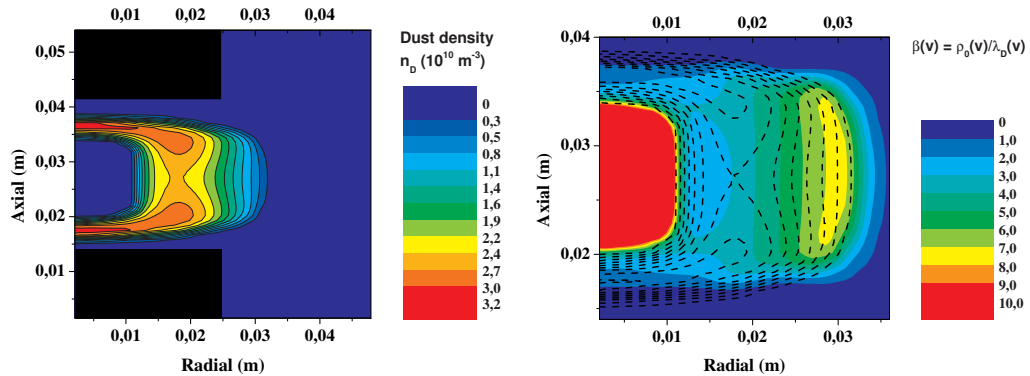


Figure 5.3: **Left:** The final dust density profile for the calculation with the Khrapak form of the Coulomb logarithm, using equation 2.52. Notice the change in the shape and size of the void. Also note that the radial dust transport is smaller here. **Right:** $\beta(v)$ for the solution with the Khrapak form of the Coulomb logarithm. Inside the dust cloud $\beta(v)$ stays below 7, which means that equation (2.52) and equation (2.38) are reasonable. Inside the void again scattering beyond the screening length is very important. Dashed lines correspond to the final dust density profile shown in the left frame.

them from reaching the force balance point exactly, as discussed in section 2.3.6.

5.2.2 Ion flow speed

We have already seen that the ion flow in this discharge is not large enough to make the linearized Debye length approach the electron Debye length near the edge of the bulk of the discharge. However, ion flow can have an important effect on the ion drag force. Figure 5.5 shows the ion drift velocity normalized to the thermal ion velocity, where we assume that $T_i \approx T_n = 293K$, for the solution with the Khrapak logarithm.

We see that the ions move close to the thermal velocity in the bulk of the discharge. Axially, they are accelerated by the dust, but mainly by the global electric field induced by the applied potential on the electrodes. Radially, this electric field plays only a minor role. The main electric field in the radial direction is caused by the charged dust cloud and by the electric field caused by the difference in mobility of the ions and electrons moving to the outer walls.

It is interesting to note that the scattering of ions on the charged dust particles decelerates the ions inside the dust cloud back to thermal drift velocities. Once they reach the edge of the dust cloud, they escape and are accelerated towards the outer walls again. This behavior of the ion drift speed was also assumed in

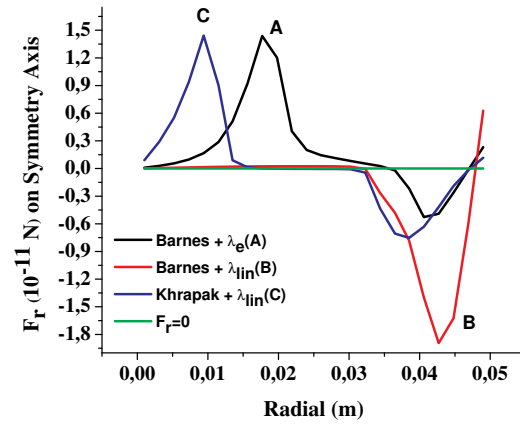


Figure 5.4: The total radial force at the axis of symmetry for both the approach by Barnes *et al.* with the electron Debye length (black, labelled 'A'), the linearized Debye length (red, labelled 'B') as well as the approach by Khrapak *et al.*, with the linearized Debye length (blue, labelled 'C'). The force balance point shifts inwards for the latter approach, resulting in a smaller void and less transport outwards. The thin green line indicates $F_r = 0$.

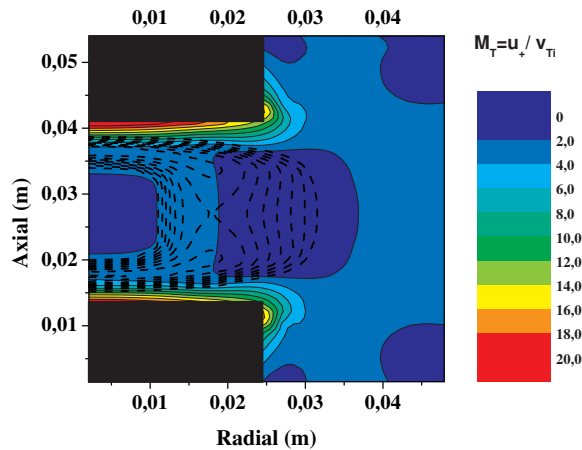


Figure 5.5: The ion drift velocity solved self-consistently from the effective electric field. Dashed lines correspond to the final dust density profile shown in figure 5.3.

[21], where an analysis of dust acoustic waves lead to the conclusion that the ions were decelerated in the dust to sub-thermal drift speeds. We see that the thermal ion Mach number, M_T , never exceeds 4 inside the dust cloud, except close to the electrodes in the (pre-)sheaths. We therefore mainly expect an effect of the ion flow speed on the ion drag force close to the electrodes. Near the void edge the Mach number, $M_T \sim 2 - 4$, which is in good correspondence with [21, 22]. This value of the Mach number near the void edge is to be expected since the ratio of the ion drag force and the electrostatic force decreases rapidly for $M_T > 1$ [22] and force balance is reached within this range of Mach numbers.

Figure 5.6 shows the final dust density profile when we use the Khrapak form of the Coulomb logarithm together with the empirical adjustment of the ion drift velocity as suggested by Hutchinson (the grey contours), see equation 2.57, as well as the final dust density profile when we only use the Khrapak form of the Coulomb logarithm (solid lines), with equation 2.52.

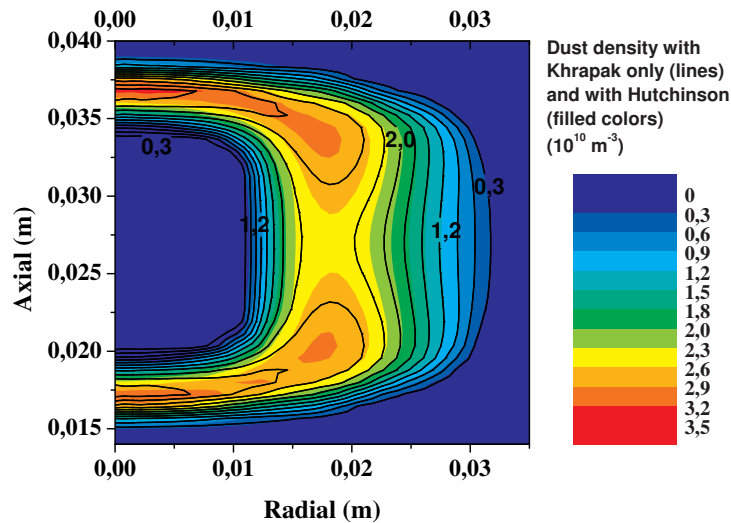


Figure 5.6: A zoom in on the dust density profiles for the calculation using the Khrapak form, equation 2.52 (black, solid lines) and the case where the effect of flow has been included, equation 2.57 (grey contours, called 'K+H'). Note that the values and spacings are equal for the lines and the color contours. The effect of flow is mainly visible near the void edge and the outside of the cloud.

In our discharge the electron energies range from 3 - 7 eV, so on average the electron energy is approximately 5 eV. This means that the Bohm velocity corresponds to a thermal Mach number of $M_B \approx 13$. According to [8], the effect of ion drift becomes important for $u_+ \approx 0.55v_B$, which thus corresponds to a thermal

Mach number of $M_T \approx 7$. The collection force however becomes dominant when $M_T \approx \sqrt{(\lambda_D/R)\beta_T}$, where $\beta_T = e^2 Z_D / 4\pi\epsilon_0 k_B T_+ \lambda_D$ [23]. In the sheath this corresponds to a thermal Mach number of $M_T \approx 8.5$.

The shape of the dust cloud edge in front of the electrodes is therefore determined by the collection force and is approximately the same for both solutions. The shape of the inner edge of the void is mainly determined by ions flowing below the Bohm speed. For our solution of the ion flow, the increase in the scattering ion drag force is approximately 15 %. Inside the dust cloud the ions are first accelerated, leading to a slight increase in the ion drag force, but then decelerated again by (recombination on) the negatively charged dust particles. The dust contours on the outside of the dust cloud are again the same, since ions are showing almost no drift there, as is shown in figure 5.5.

5.2.3 Collisions

We consider two effects of collisions between flowing ions and neutrals (charge-exchange collisions), namely the effect of these collisions on the ion flow towards the dust particles and thus the charging of dust particles, and on the increase of momentum transfer caused by these collisions and the corresponding increase of the ion drag force. One of the important parameters here is the ratio of the linearized Debye length and the ion-neutral mean free path. Figure 5.7 shows this parameter for the calculation with the Khrapak form of the logarithm.

We see that the ratio is very small inside the void. This has to do with the small size of the linearized Debye length, which in the bulk equals the ion Debye length. The mean free path is calculated for constant momentum transfer frequency and therefore only depends on the drift velocity of the ions. We expect no effect of the collisions on the ion drag force in the bulk of the discharge. Towards the outer edge of the dust cloud however, the "Collision function", $\mathcal{K}(x)$, becomes comparable to the Coulomb logarithm Λ , which happens when $x = \lambda_D / l_{mfp} \approx 3$ in equation (2.57).

When we compare the dust density distribution for the solution with the Khrapak form including the adjustment for ion flow and a similar solution, but now including the effect of collisions on the ion drag force, we indeed see the largest shift near the outer edge of the dust cloud, which is shown in figure 5.8.

Finally, we included the effect of collisions on the charging of dust particles. It is important to realize that even though x might be smaller than 1, the charging can still be affected when $e\phi_D/E_s$ is large enough, and this is exactly the case in the bulk of the discharge.

Figure 5.9 shows the charge per dust particle for the calculation when we use the Khrapak form of the Coulomb logarithm, together with the standard OML expressions, equation 2.31, and equation 2.32 for the currents towards the dust

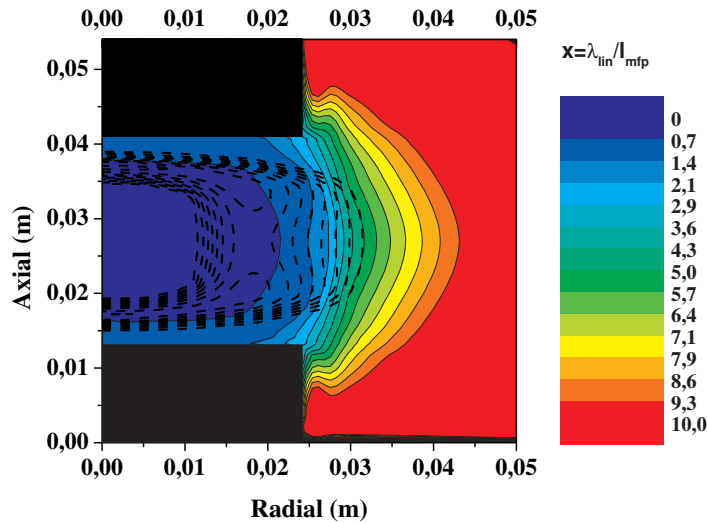


Figure 5.7: The ratio of the linearized Debye length to the mean free path for ion-neutral collisions, called 'x'. When this ratio is large, collisions occur within the screening length of the dust particles and will affect both the charging of the dust particles as well as the ion drag force acting on the dust particles. Dashed lines correspond to the final dust density profile as shown by the color contours in figure 5.6.

particles, in the upper figure. The bottom figure shows the same, when the effect of ion-neutral collisions is included in the current balance towards the dust particles, using equation 2.38. We see that the charge a dust particle in the bulk would have is reduced by a factor of 2 or more. Near the void edge, the effect of the collisions is very small, since both λ_D/l_{mfp} and $e\phi_D/E_s$ are small. Near the outer edge of the dust cloud the ions are decelerated and $e\phi_D/E_s$ becomes large again, reducing the charge on the dust particles. Near the walls the linearized Debye length becomes very large, as is shown in figure 5.7, and the charge is reduced here as well.

Finally, in figure 5.10, we show the total radial force along the axis of symmetry for the simulations above. We see that the total force with the reduced charge deviates the most from the simple Khrapak solution. Inside the void, the force is much more repelling than in the other cases, since the electrostatic force pulling the particles in is reduced. The force balance point (where $F_r = 0$) also lies slightly more inward. Only for the calculation including the reduced dust charge, does the total force actually change sign at the point where it becomes zero. The other forces stay very close to 0 for a large radial interval before becoming neg-

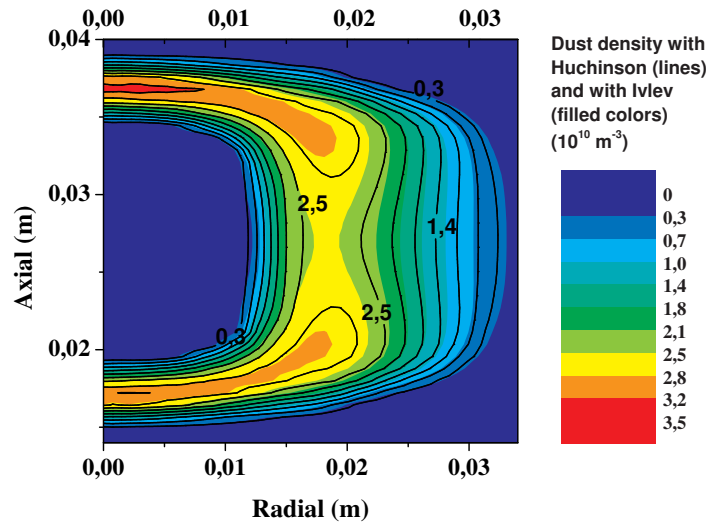


Figure 5.8: A zoom on the dust density profiles for the calculation using the Khrapak form with the adjustment for ion flow (black, solid lines, called 'H') and the case where the effect of collisions has also been included (color contours, called 'H+I') in equation 2.57. The largest shift in dust density is observed near the outside of the dust cloud.

ative (pointing inward) near the outer wall. It is here that also the effect of the collisions on the ion drag force becomes important. Towards the outer wall (at the outer edge of the dust cloud), the force is clearly less negative, due to the increase in the outward ion drag force. Near the edge of the void the force is slightly increased, due to the ion flow speed. This effect is very small, however.

5.3 Comparison with experiments

Here we will discuss the experimental results as found and discussed in [14, 18, 19] and [15, 16]. The first papers discuss measurements of trajectories of particles falling through the bulk of a RF discharge. The last two discuss the formation of voids around (Langmuir) probes introduced into a complex plasma.

5.3.1 Particles falling through RF discharge

In this experiment dust particles were released from the topside of a vertical tube at relatively high pressures. The dust particles fell through a plasma volume powered by a RF generator. Using a laser sheet and a CCD camera the trajectories of

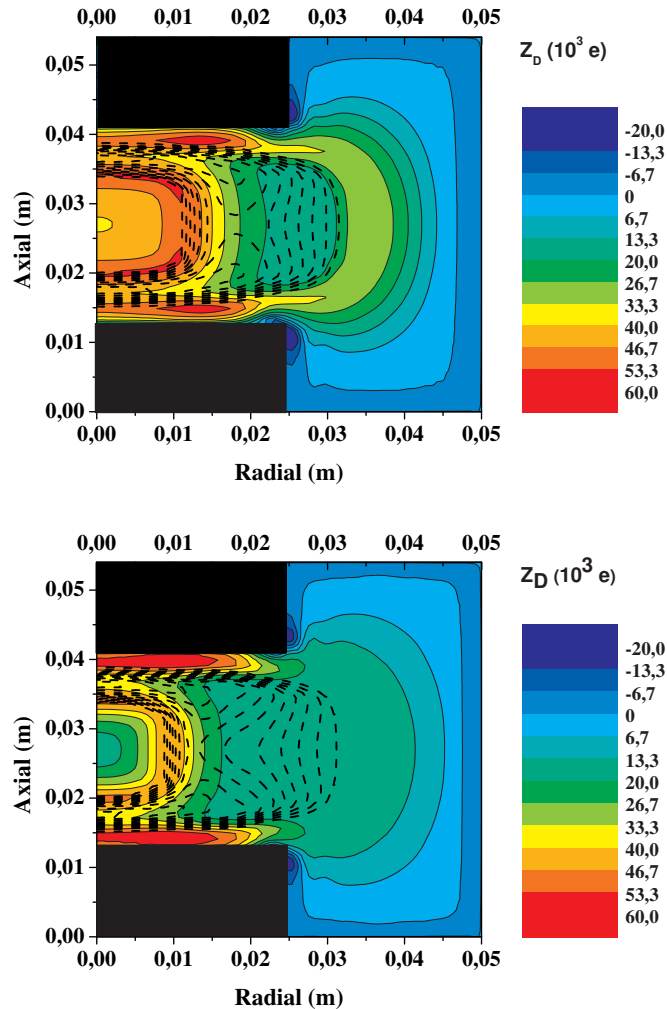


Figure 5.9: **Top:** The number of electrons on a dust particle, Z_D , calculated for the ion drag force with the Khrapak logarithm, equation 2.52. The charge is given by $Q_D = -eZ_D$, so that a positive number in the graph corresponds to a negative dust charge, and a negative charge number to positively charged dust. Note that the charge is calculated throughout the chamber, even where no dust is present.

Bottom: The same as in the upper figure, but now with the effect of ion-neutral collisions on the ion current to the dust particles, using equation 2.38. In the bulk and towards the outer edge, the charge ($Q_D = -eZ_D$) is reduced significantly.

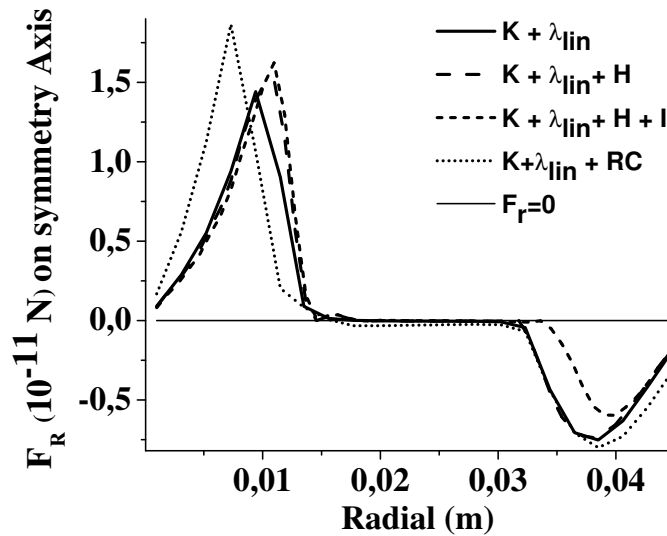


Figure 5.10: The net radial force along the axis of symmetry for the different calculations. 'K' stands for the Khrapak approach, 'H' for the Hutchinson addition, 'I' for the calculations where the collision operator for the ion drag force was taken into account and 'RC' for the calculations with the reduced charge, due to the effect of charge-exchange collisions on the ion current to the dust particles.

the dust particles were captured. From the trajectories perpendicular to the tube, the ratio of the electrostatic force and ion drag force was determined. This ratio (typically between 0.5-5) was then plotted against the Debye length over the dust particle radius and the Debye length over the ion mean free path.

It was observed that the ions showed only small drift velocities, $M_T \leq 2$, which seems reasonable when we look at the ion flow in the bulk of our simulations. Secondly, it was stated that for higher pressures, the assumption of collisionless theory might fail. From our calculations, the effect of the collisions on the charge of the dust particle might be even more important. Since $F_{ion} \propto Q_D^2$ and $F_E \propto Q_D$, one then overestimates the ion drag force even more, by using OML theory to determine the dust charge.

One statement made in [14] is that in the case of the ion drag force calculated with the approach by Khrapak, the ion drag force shows a dramatic increase up to a factor of 40. Figure 5.11 shows the ratio of the radial ion drag force to the radial component of the electrostatic force. (Similar to the ion drag force and electrostatic force considered in the experiment.) Clearly, even for the approach with the Khrapak logarithm and the linearized Debye length, the ratio of the two forces lies between 2-4 in the bulk of the discharge, which seems to be in reasonable agreement with figure 3 in [14].

We did not include the ratio for the calculation using the Barnes form of the Coulomb logarithm together with the linearized Debye length as the cut-off radius. From figure 5.4, and the fact that no void is present for this calculation, we can see that the ratio would be very small. So comparing the Khrapak form of the Coulomb logarithm with the linearized Debye length as the cut-off radius with the Barnes form and the linearized Debye length, would indeed show a large difference. But in [14], the electron Debye length was used as the maximum impact parameter.

5.3.2 Void formation around probe

In these experiments probes were introduced in a dusty plasma, biased negatively with respect to the surrounding plasma. The electric field accelerates positive ions towards the probe tip and negatively charged dust particles away from the probe tip. The ions streaming towards the probe tip are collected and deflected by the dust particles, and the corresponding ion drag force acts towards the probe. The equilibrium position of the dust around the probe comes from the balance between the electrostatic force *away from* the probe and the ion drag force *towards* the probe. This results in the formation of a void around the tip of the probe.

In [15] dust particles were suspended in the anode spot of a DC discharge, after which a probe was introduced into the plasma. The reported electric field around the probe is in the range of $1200 \sim 3400 \text{ Vm}^{-1}$, which is much larger than the vertical electric field which balanced the force of gravity, resulting in the original vertical equilibrium position of the dust particles in the anode spot. The average ion drift velocity reported was 1000 m s^{-1} , which, for room temperature, means a thermal Mach number of $M_T \sim 3$, which is in agreement with the Mach number at the void edge found in our simulations.

The ion drag in [15] was calculated using the Barnes equation with the electron Debye length as the upper value for the impact parameter. For $M_T \sim 3$ the ion drag might therefore be somewhat overestimated for the dust particles used ($2.9 \mu\text{m}$) and the plasma density ($\sim 10^{15} \text{ m}^{-3}$) reported. Using numbers in the paper, we find $\beta(v) \approx 5$. Thus, it is justified to use equation (2.52) for the ion drag. We then find a total ion drag force of $F_{ion} \approx 3.1 \times 10^{-12} \text{ N}$. This is an order of magnitude smaller than the value found in [15] ($\approx 2 \times 10^{-11} \text{ N}$).

The electric field required to balance the ion drag is then given by $E = F_{ion}/Q_D$. The reported charge was $Q_D \sim 5200e$, which results in an electric field of approximately 3725 Vm^{-1} . The value calculated in [15] seems to be an order of magnitude too low, since $2 \times 10^{-11} \text{ N}/(5200e) \approx 24000 \text{ Vm}^{-1}$, where $(3400-1200) \text{ Vm}^{-1}$ was reported.

Using an ion-neutral collision cross section of $65 \times 10^{-20} \text{ m}^2$ [16] and a neutral density $N \sim 10^{21} \text{ m}^{-3}$, we find the argon ion mobility as $\mu_i \approx 1$. Which means

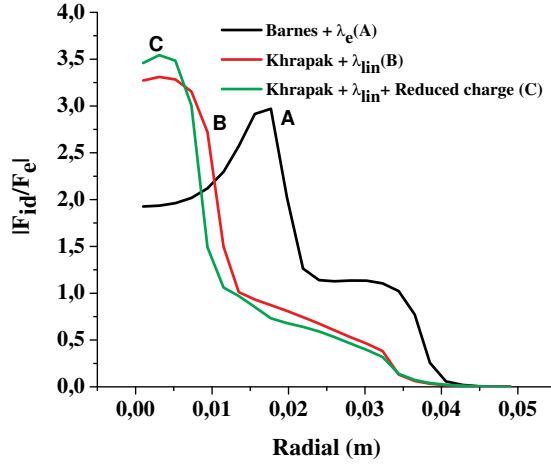


Figure 5.11: The ratio $|F_{ion}/F_E|$ for the different simulations. In the bulk, the ratio lies approximately between 2 and 4 for all the theoretical approaches. All values agree well with the values found in experiment.

that the drift velocity $u_i = \mu_i E$ would give $u_i \approx 4 \times 10^3 m s^{-1}$. This value is of the same order as the drift velocity assumed ($500-1500 m s^{-1}$), even though it is somewhat too high. The ion drag force calculated including large angle scattering gives the best results in this case.

In [16] a probe was introduced inside the void of a dusty plasma under micro-gravity. We have seen that inside the void $\beta(v) \gg 1$ and that the charge of dust particles is reduced with respect to the OML charge. However, the ratio of F_{ion}/F_E remains approximately the same. The parameters in [16] are almost the same as used in our simulations, except for the dust particle size. The forces in balance are also in the $10^{-12} N$ range, however, the charge is calculated using OML theory. Again, estimating the ion drift velocity from the balance with the electric field (and using the OML value of the dust charge $Q_D = 10000e$), we find for the solution with Barnes an electric field of $E = 850 V m^{-1}$ while for the solution with Khrapak and the ion Debye length $E = 331 V m^{-1}$. The first results in an ion drift velocity of approximately $u_+ = 1000 m s^{-1}$, while the latter gives approximately $u_+ = 300 m s^{-1}$.

Even though both solutions are in the right order, in the first approach it was assumed that the ions were flowing with the Bohm speed, $u_+ \equiv v_B = 2800 m s^{-1}$, where in the latter approach ions were assumed to flow at the thermal speed, $u_+ = v_T = 300 m s^{-1}$. So the approach with Khrapak and the ion Debye length is again more self-consistent, as far as the electric field and the ion flow

calculated from the force balance is concerned.

As was mentioned, using thermal ions and the ion Debye length gives the lower limit for the ion drag force. The real ion drag force lies somewhere in between. This seems to be consistent with the experiment mentioned in [15] and discussed above. It is likely that at the void edge, ions are flowing with $M_T \approx 3$ and large angle scattering with the linearized Debye length is important. Using the approach by Barnes with the electron Debye length strongly overestimates the ion drag force, which results in inconsistent ion drift velocities.

5.4 Conclusions

Our modelling and the comparison with experiments show that large angle scattering is very important for the interaction between ions and dust particles. Still, the formation of a void is observed for all the simulations, except for the Barnes approach with the linearized Debye length. The flow speed of the ions is not sufficient to create a void and the Barnes form of the Coulomb logarithm results in an insufficient ion scattering cross section.

When applying the theory to experiments performed in the recent past, it seems that the ion drag force has been overestimated in most cases, by using the Barnes approach with the electron Debye length. This is also confirmed by our simulations, where the void is much larger for the calculation with this approach than with the approach by Khrapak. This smaller size of the void also corresponds better with the size of the void usually observed in experiments under micro-gravity conditions done in the PKE chamber.

The shape of the void observed in these experiments depends on the pressure and input power and on the size of the dust particles used. In [24] small in-situ grown particles form a clear lentil shaped void. Small particle size means small charge, which means small $\beta(v)$. Both the solution of Barnes *et al.* and the solution of Khrapak give reasonable and similar solutions in this limit, which, from our simulations, result in more round-shaped voids. The pressure in these experiments was also relatively high, resulting in slow ion drift speeds and many ion-neutral collisions.

In other experiments, larger particles were used, for instance with a $7.5 \mu m$ radius in [20]. The shape of the void in this experiment is less lentil shaped and more rectangular, especially for higher input powers. Since near the void edge, the ion drift speed is always similar ($M_T \approx 2 - 3$), the higher dust particle radius will result in a higher $\beta(v)$, so that the solution with the modified Coulomb integral differs greatly from the solution with the Barnes form of the Coulomb logarithm, which in our simulation indeed produces more rectangular shaped voids.

Ion-neutral collisions in a dusty plasma under micro-gravity do not have an

important effect on the ion drag force for the range of parameters considered here, except at the outer edge of the dust cloud, near the outer walls of the discharge. They do change the charge however, especially when the ion flow is low and the dust charge high, which is the case in the bulk of the discharge.

Ions do not flow faster than $M_T \sim 4$ in dust clouds in the dusty plasmas modelled, except in front of the electrodes. Inside the dust cloud they are decelerated again, in some simulations even below the thermal velocity. This means that the correction proposed by Hutchinson plays only a minor role in the transport of dust in dusty RF discharges like the one modelled here. In other types of discharges, such as DC discharges, this might be different though. The value of the Mach number near the void edge always lies between 2 and 4.

It is worthwhile to mention that we do *not* observe a steep dust density gradient on the inside of the void. This can be due to the limited resolution in our simulations, since this high density layer on the inside is typically a few particle layers thick. It is still a question whether or not this sharp void-dusty plasma boundary results from the matching between the two regions and the necessary space charge layers [25, 26], or is a shock-like structure [27].

References

- [1] M. R. Akdim and W. J. Goedheer, Phys. Rev. E **65**, 015401(R) (2002)
- [2] M. R. Akdim and W. J. Goedheer, Phys. Rev. E **67**, 066407 (2003)
- [3] P. S. Epstein, Phys. Rev. **23**, 710 (1923)
- [4] B. Liu, J. Goree, and V. Nosenko, Phys. Plasmas **10**, 9 (2003)
- [5] W. E. Amatucci, D. N. Walker, G. Gatling, and E. E. Scime, Phys. Plasmas **11**, 2097 (2004)
- [6] E. Thomas, Jr. and J. Williams, Phys Rev. Lett. **95**, 055001 (2005)
- [7] J. E. Allen, Phys. Scr. **45**, 497-503 (1992)
- [8] I. H. Hutchinson, in "New Vistas in Dusty Plasmas" (proceedings of the 4th International Conference on the Physics of Dusty Plasmas), AIP Conference Proceedings, Vol 799, page 38 (2005)
- [9] S. A. Khrapak *et al.*, Phys. Rev. E **72**, 016406 (2005)
- [10] M. Lampe, R. Goswami, Z. Sternovsky, S. Robertson, V. Gavrishchaka, G. Ganguli, and G. Joyce, Phys. Plasmas **10**, 1500 (2003)
- [11] S. A. Khrapak, A. V. Ivlev, G. E. Morfill, and H. M. Thomas, Phys. Rev. E **66**, 046414 (2002)
- [12] A. V. Ivlev, S. A. Khrapak, S. K. Zhdanov, G. E. Morfill, and G. Joyce, Phys. Rev. Lett. **92**, 205007 (2004)
- [13] A. V. Ivlev, S. K. Zhdanov, S. A. Khrapak, and G. E. Morfill, Phys. Rev. E **71**, 016405 (2005)
- [14] C. Zafiu, A. Melzer, and A. Piel, Phys. Plasmas **10**, 1278 (2003)
- [15] E. Thomas, Jr., K. Avinash, and R. L. Merlino, Phys. Plasmas **11**, 1770 (2004)
- [16] M. Klindworth, A. Piel, A. Melzer, U. Konopka, H. Rothermel, K. Tarantik, and G. E. Morfill, Phys. Rev. Lett. **93**, 195002 (2004)

-
- [17] M. S. Barnes, J. H. Keller, J. C. Forster, J. A. O'Neill, and D. K. Coultas, *Phys. Rev. Lett.* **68**, 313 (1992)
- [18] S. A. Khrapak, A. V. Ivlev, G. E. Morfill, H.M. Thomas, S. K. Zhdanov, U. Konopka, M. H. Thoma, and R. A. Quinn, *Phys. Plasmas* **10**, 4579 (2003)
- [19] C. Zafiu, A. Melzer, and A. Piel, *Phys. Plasmas* **10**, 4582 (2003)
- [20] G. E. Morfill, H. M. Thomas, U. Konopka, H. Rothermel, M. Zuzic, A. V. Ivlev, and J. Goree, *Phys. Rev. Lett.* **83**, 1598-1601 (1999)
- [21] S. Khrapak *et al.*, *Phys. Plasmas* **10**, 1 (2005)
- [22] M. Kretschmer *et al.*, *Phys. Rev. E* **71**, 056401 (2005)
- [23] A. V. Ivlev, S. K. Zhdanov, S. A. Khrapak and G. E. Morfill, *Plasma Phys. Control. Fusion* **46** (2004) B267-B279
- [24] M. Mikikian, L. Boufendi, A. Bouchoule, H. M. Thomas, G. E. Morfill, A. P. Nefedov, and V. E. Fortov, *New J. Phys.* **5**, 19 (2003)
- [25] B. M. Annaratone *et al.*, *Phys. Rev. E* **66**, 056411 (2002)
- [26] P. M. Bryant, *New J. Phys.* **6**, 60 (2004)
- [27] V. N. Tsytovich, S. V. Vladimirov, and G. E. Morfill, *Phys. Rev. E* **70**, 066408 (2004)

6. The plasma inside a dust free void: Hotter, denser, or both?

Abstract. *This chapter continues the investigation of the presence of a void in dusty plasmas under micro-gravity conditions as started in chapter 5. In this chapter we focus on the effect of dust on the electrons and on the mechanism which supplies the energy required for the source of ionization in the dust free void. We start by using a global model to predict the effect of the dust on the electron density and temperature. We then continue by using the fluid model to show how the ionization inside the void comes about. The heating of the electrons takes place inside the dust clouds, due to electron depletion. Due to this depletion, a growing electron temperature gradient exists, which points in the right direction to act together with the time-averaged electric field, causing the transport of heat into the void. This heat is then lost inside the void through the creation of plasma by inelastic electron-impact ionizations. We also show that this heat transport is not due to a similar gradient in the electron density. We compare our results of the fluid model with results of the particle-in-cell/Monte Carlo approach in the final section of this chapter.*

Based on :

New Journal of Physics **9**, 246 (2007)

Authors :

V. Land, W. J. Goedheer

6.1 Motivation

In a plasma where small sub-micron particles form through chemical reactions [1], or in dusty plasma experiments done under micro-gravity conditions [2], a dust-free void is usually observed. This void results from flowing ions being scattered and collected by the dust particles, thereby transferring momentum and pushing them in the direction of the dominant ion flow. Consequently, this void requires ionization inside the dust-free void. The corresponding peak in optical emission inside the void has indeed been observed in many cases, for instance in [3, 4], and more recently in [5, 6].

Dust particles in a plasma collect ions and electrons. In equilibrium, the electron current to the dust equals the ion current and the potential of the dust particles reaches the floating potential. Thus, plasma continuously recombines on the dust and the dust acts as an extra sink for plasma. This loss of plasma has to be compensated by ionization. In the region of depletion, this requires an increase in the average electron energy (i.e. electron temperature), because every single electron must have a higher ionization probability. One can then wonder why the ionization occurs inside the void, since there is no depletion of plasma there.

It was first proposed that the increased ionization is due to an increased electron temperature in the void, caused by the electron depletion in the dust cloud. In a way, this depletion increases the resistivity of the plasma, increasing the electric field [1, 3]. This increased electron temperature was also shown in several simulations [7, 8, 9].

In experiments however, no increase of the electron temperature was observed [10]. It was then supposed that the increased ionization was due to the enhanced electron density in the void, with respect to the electron depleted plasma in the surrounding dusty region [4, 11]. In a recent experiment in an inductively coupled dusty plasma [6], it was shown that both the electron temperature and the electron density increase in the void. This was also the result of a simulation [12]. In this one dimensional simulation the dust and plasma components were not coupled self-consistently, however.

Finally, a recent paper [13] shows that the void is also present when very few particles are used. This means that also in a dust-free discharge the same principles must apply, namely high ionization in the center of the discharge, resulting in the diffusion of ions from the center outwards. Apparently, this is still so when a large amount of dust is present.

In this chapter we show how this complex structure of the void comes about. We first demonstrate by using a simple global model, similar to the approach followed in [14, 15], that we always expect an increase in the electron temperature when dust is added to a plasma, but that the behavior of the electron density inside the void strongly depends on whether the dust causes a volume loss process or a

surface like process. The latter can happen when a void forms. We show that the plasma in the void is both hotter as well as denser, and we show why this is so. In the end we compare these results with simulations done with the particle-in-cell/Monte Carlo model.

6.2 Plasma response to dust: Global model

The electron temperature in a discharge is determined by the balance between plasma creation (ionization) and plasma losses (Bohm fluxes to the walls; $F_{Bohm} = n_{e,\infty} \exp(-1/2)u_B \approx 0.6 n_e u_B$). In a global model [14, 15], we can write this as

$$n_n n_e \langle \sigma v \rangle \times V = 0.6 n_e u_B \times S, \quad (6.1)$$

where V is the volume in which ionization takes place, $\langle \sigma v \rangle$ is the (electron energy dependent) ionization rate, u_B is the Bohm velocity, $u_B = \sqrt{k_B T_e / m_+}$, with T_e the electron temperature, and m_+ the ion mass. S is the surface area of the walls surrounding the plasma. The input power then determines the plasma density, since

$$P_{input} = n_n n_e \langle \sigma v \rangle \times V \times \epsilon_{ion}, \quad (6.2)$$

with ϵ_{ion} the effective energy required to produce one ion.

Suppose now that through chemical reactions small particles have formed homogeneously throughout the discharge. They are well below 30 nm, so that no void forms [16]. We can then assume that the loss of plasma on the dust results in a *volume* loss process. We therefore rewrite equation 6.1 into

$$n_n n_e \langle \sigma v \rangle \times V = 0.6 n_e u_B \times S + n_D n_e k_{rec} \times V, \quad (6.3)$$

where n_D is the dust particle density and k_{rec} is the recombination rate of ions and electrons on the dust, which follows from Orbital Motion Limited charging theories, as explained in chapter 2. Rewriting this gives

$$(n_n \langle \sigma v \rangle - n_D k_{rec}) \times \frac{V}{S} = 0.6 u_B. \quad (6.4)$$

Since no void has formed, we assume that V/S does not change. Figure 6.1 shows the volume production term and the Bohm loss, as well as the production term corrected for the volume losses on the dust found from equation 6.4. This plot is for a radius of the plasma volume of 2.3 cm, such that $V/S \approx 0.0075$. This corresponds to a plasma with the size of the void shown in section 6.4, homogeneously filled with dust. $\langle \sigma v \rangle$ is calculated for argon and is the same as used in

our fluid model. In this plot, the volume losses to the dust correspond to 50 % of the volume production in the plasma.

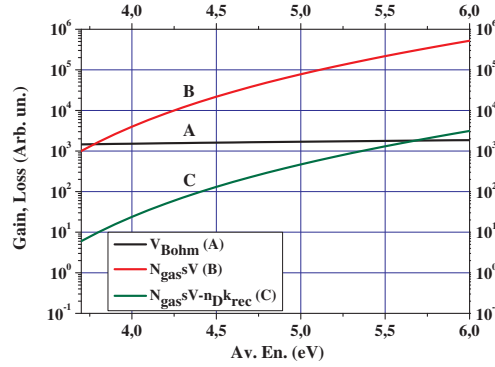


Figure 6.1: This figure shows the losses to the walls, represented by the thick black line, labelled 'A', the volume production without extra losses, represented by the red line, labelled 'B', and the production corrected for the volume losses, represented by the green line, labelled 'C'. Where they cross the thick black line is the equilibrium point. We see that with volume losses, the equilibrium shifts to a higher temperature resulting in higher production.

We see that an extra volume loss term shifts the balance of production and loss to a higher temperature. This of course corresponds to a higher plasma production rate. Assuming that the input power is constant, and that the effective energy required to form an ion also does not change, it follows from equation 6.2 that this increase in production requires a *decrease* in the plasma density, n_e . The conclusion then is that *volume loss processes increase the electron temperature, but decrease the plasma density*.

Assume now that the dust particles have grown further, and a void forms. This way the losses on the dust particles make a transition from a homogeneous volume loss process to a more localized *surface* loss process, where the inside of the dust-free void acts like a wall. We therefore rewrite the particle balance as

$$n_n n_e \langle \sigma v \rangle \times \tilde{V} = n_e u_B \times \tilde{S}, \quad (6.5)$$

where \tilde{S} is the effective absorption surface of the inside of the void. \tilde{V} is the new volume in which plasma is formed, which is the volume inside the void. We rewrite this again as:

$$n_n \langle \sigma v \rangle \times \frac{\tilde{V}}{\tilde{S}} = u_B. \quad (6.6)$$

We see that now the volume to surface ratio becomes important. Both the dust density and size (which determine \tilde{S}) as well as the discharge settings (which play a role in the volume of the void, \tilde{V}) determine the losses in the plasma. Figure 6.2 shows the production and losses again, for two ratios of the volume over the surface. We see that a smaller void (which has a smaller volume over surface ratio) results in a higher electron temperature and more production.

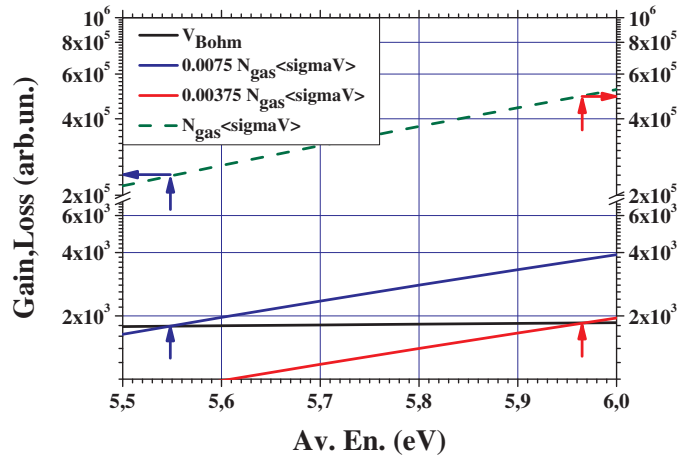


Figure 6.2: This figure shows the losses to the "walls", represented by the black line, the volume production without extra losses, represented by the green, dashed line, and the production corrected for the surface losses for a large and smaller void, represented by the blue and red line, respectively. We see that with surface losses, the balance shifts to a higher temperature for decreasing size of the void.

For a 8 times smaller volume of the void (going from the dashed to the dotted line in figure 6.2), we see that the production becomes 2 times higher. This way, we find from equation 6.2, that the plasma density must be 4 times *higher*. So, when the dust forms a void and acts like a wall, with dominant surface loss processes, *the electron temperature goes up together with the plasma density*. We now turn to the results of the self-consistent fluid model, and show in more detail what happens to the plasma properties in a dusty plasma when a void forms.

6.3 Modelled geometry

We model the geometry of the PKE-Nefedov experiment, which was used aboard the International Space Station [2]. This is a RF device with two cylindrical elec-

trodes, 3 cm apart, with a radius of 2.1 cm, both powered by a 13.56 MHz harmonic potential in push-pull mode. The electrodes are shielded by a so called dark-shield with a radius of 2.4 cm to prevent the generation of a discharge between the sides of the electrodes and the outer wall.

The simulation is started without dust at a constant potential of 100 Volt peak-to-peak. This corresponds to a total power of $W_{tot} = 6 \cdot 10^{-2}$ W. The background pressure is set at $P_n = 204$ mtorr (27 Pa) at 273 K. In this plasma the total power equally divides between the ions ($W_+ = 2.8 \cdot 10^{-2}$ W) and the electrons ($W_e = 3.2 \cdot 10^{-2}$ W).

When the dust-free plasma reaches a periodic solution, the dust is added. In the experiment dust is introduced with two shakers in the electrodes, which we model by adding source terms for the dust just above the lower and below the upper electrode. The dust particles are mono-disperse and have a radius of 6.8 μm . During the run the void evolves self-consistently. With the dust present, we keep the total power constant (at $6 \cdot 10^{-2}$ W), which in the final equilibrium state requires a lower driving potential of only $V = 78.8$ V peak-to-peak. We add 500.000 dust particles in total and calculate until the equilibrium dust structures are formed. With this amount of dust, the power is distributed over the plasma as $W_e = 4 \cdot 10^{-2}$ W and $W_+ = 2 \cdot 10^{-2}$ W.

Even though we do not present them here, the results for a dusty discharge at a constant driving potential of 100 Volts (instead of constant applied power) are similar. It is interesting to note that the total power then increases to $8 \cdot 10^{-2}$ W.

6.4 Results

When we introduce dust in the discharge, the electron density and temperature change. This is shown in figure 6.3. The general conclusions of the global model are indeed confirmed. When a small number of dust particles is added, the loss terms are best described by a volume loss, which means an increase in temperature, with a decrease in density. When more and more dust particles are introduced, and a void forms, the dust acts more and more as a wall. The temperature still increases, but the density also starts to rise. The exact details, such as the intermediate rise and fall in electron density, do not follow from the global model. These exact details depend also on the exact way we model the sources of the dust particles. Most important is another effect, which will be the focus of this paper from now on. It has to do with the spatial separation of the source of electron heating, which drives the ionization, and on the position where this heat is used for ionization.

We start with a dust-free discharge. The left panel of figure 6.4 shows the power taken up by the electrons. Most of the power is taken up in the pre-

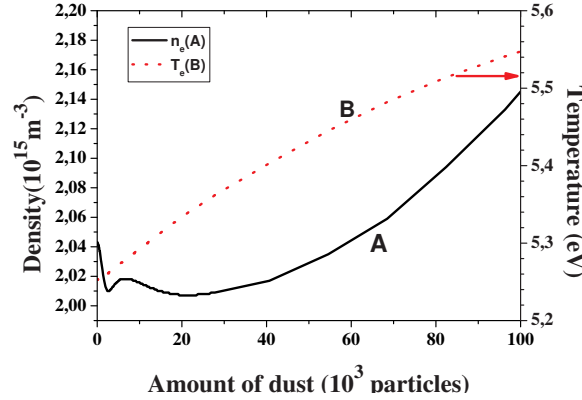


Figure 6.3: The average electron energy (eV) and the central electron density for different times after the dust sources are turned on. It is shown against the total amount of dust particles added to the discharge.

sheaths. The average electron temperature ($\epsilon = \frac{3}{2}k_B T_e$) is homogeneous however, as shown in figure 6.4 in the bottom.

The ionization profile peaks in the center of the discharge, despite the power dissipation in the pre-sheaths. The electron density is also highest there, as shown in figure 6.5. Already in the dust-free case, we see a clear separation between the position where the electrons gain energy and are heated, and in the position where they deposit this heat and ionize the background gas.

We now turn our attention to the discharge with added dust particles. The final dust density is shown in figure 6.6 on the left side. The dust-free void is clearly visible. The electron density on the right shows how indeed the plasma is confined inside the void and has a higher density of $4 \cdot 10^{15} \text{m}^{-3}$ instead of $2 \cdot 10^{15} \text{m}^{-3}$.

The heating of the electrons is shown in figure 6.7 on the left-hand side. We see that most of the power is taken up inside the dust clouds. This is expected since the electron depletion is high there. The average electron energy is again reasonably homogeneous in the bulk of the plasma, but is higher than in the dust-free case, about 6 eV instead of 5 eV.

The ionization profile peaks inside the void, as seen in figure 6.7 in the bottom panel, and reaches much higher values of $9 \cdot 10^{20} \text{m}^{-3} \text{s}^{-1}$, instead of $2 \cdot 10^{20} \text{m}^{-3} \text{s}^{-1}$. This high ionization rate agrees with the high amount of optical emission observed in dusty discharges under micro-gravity conditions.

Obviously, the heating of the electrons and the ionization are again spatially separated, but the effect is clearly enhanced by the presence of the dust. In equation 2.66 the transport of electron energy is given by:

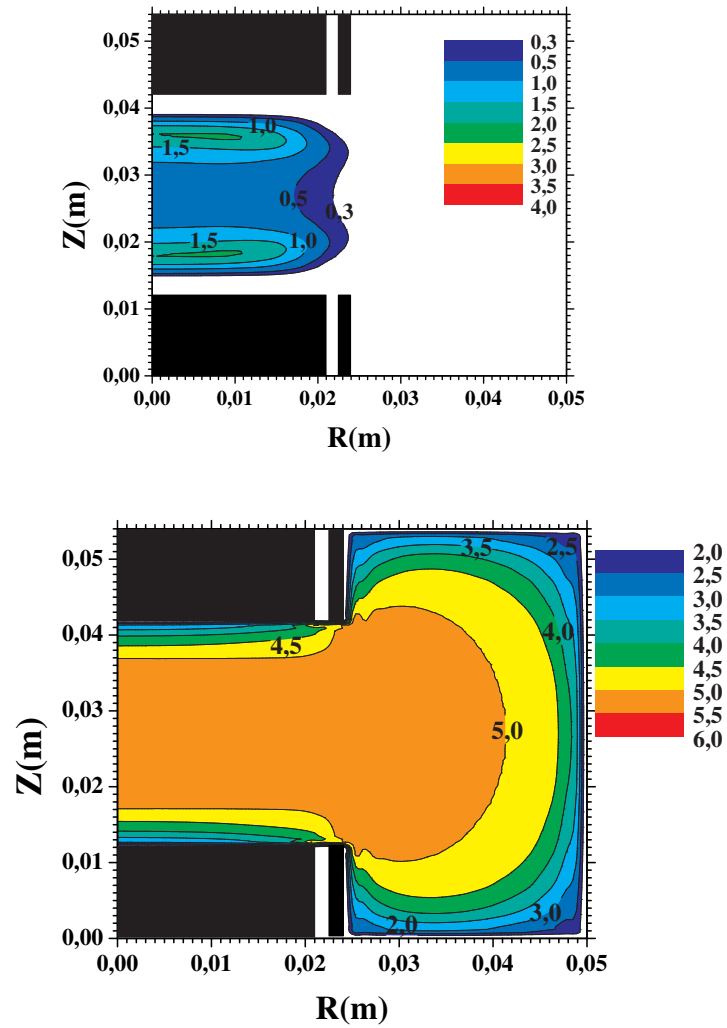


Figure 6.4: **Top:** The energy taken up by the electrons in kW m^{-3} . The electrons mainly pick up energy in the pre-sheaths. **Bottom:** The average electron energy (eV), which is reasonably homogeneous for a large part of the discharge.

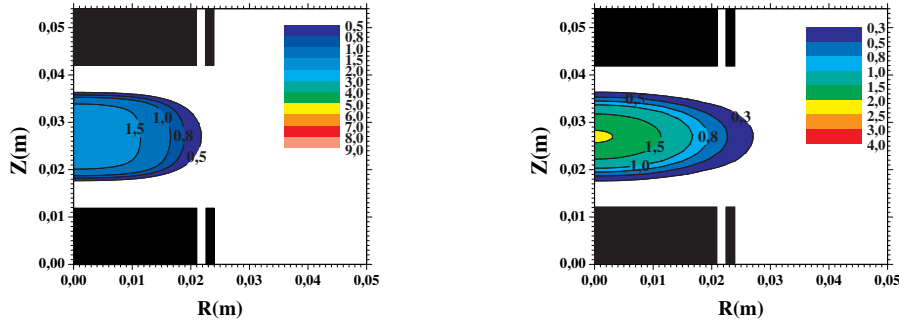


Figure 6.5: **Left:** The ionization in $10^{20} \text{ m}^{-3} \text{ s}^{-1}$, which is highest in the center. **Right:** The electron density in 10^{15} m^{-3} .

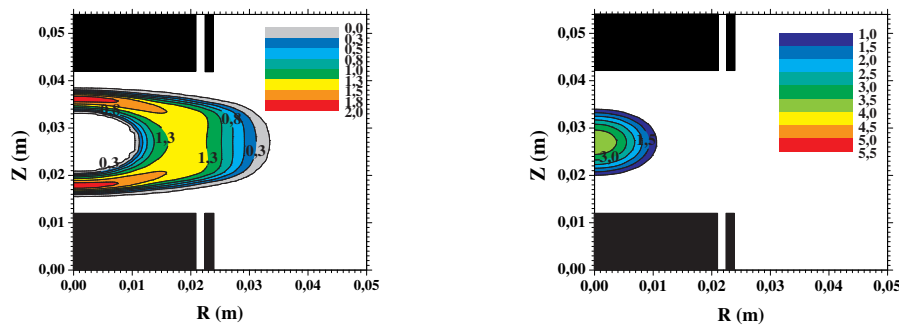


Figure 6.6: **Left:** The dust density in 10^{10} m^{-3} . The dust-free void in the center is clearly visible.

Right: The electron density in 10^{15} m^{-3} . The plasma is confined within the volume of the void.

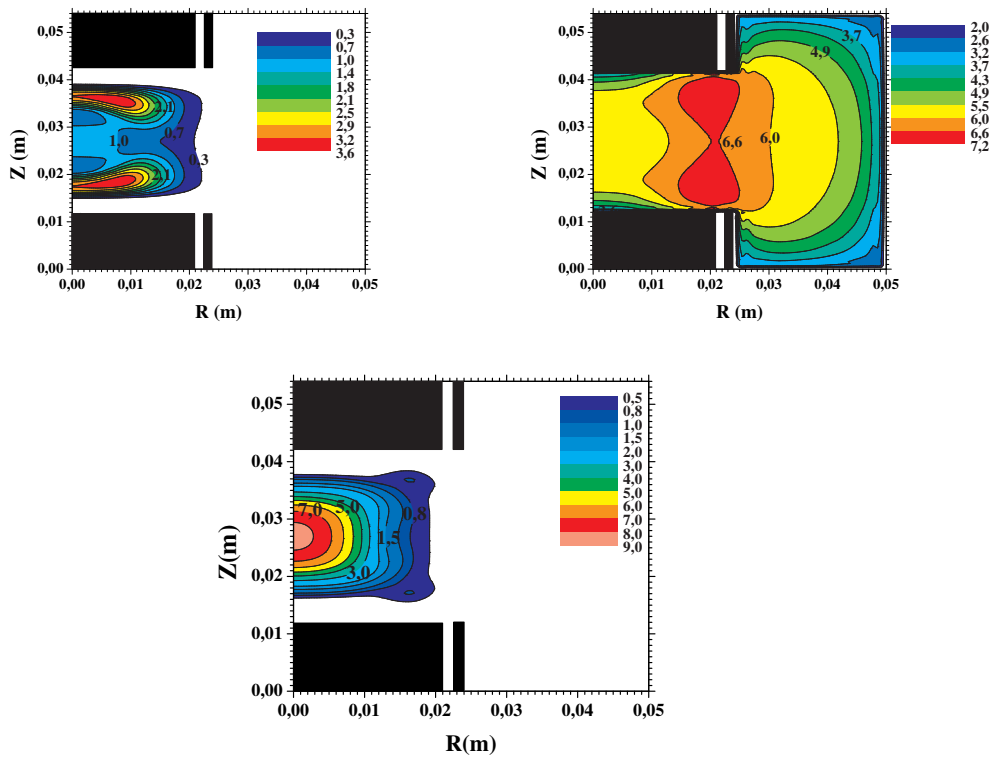


Figure 6.7: **Left:** The power dissipation in the dusty discharge at constant input power in kW m^{-3} . **Right:** The ionization in the dusty discharge. The ionization clearly peaks inside the void, and is much more pronounced in the presence of dust, which means much higher optical emission from the plasma in comparison with a dust-free discharge. **Bottom:** The average electron energy (eV), which is again homogeneous in the plasma bulk, but has a higher value than in the dust free case.

$$\frac{\partial w_e}{\partial t} + \nabla \cdot \Gamma_{w_e} = \mathbf{J}_e \cdot \mathbf{E} - S_{w_e}. \quad (6.7)$$

The time averaged energy balance (over one RF cycle) for the electrons can then be written as

$$\nabla \cdot \bar{\Gamma}_{w_e} = \bar{\mathbf{J}}_e \cdot \bar{\mathbf{E}} - \bar{S}_{w_e}. \quad (6.8)$$

The bar indicates averaging in time over one RF cycle. The term on the left-hand side is the divergence of the heat flux. The first term on the right-hand is the source of heating, the Ohmic heating, and the second term contains all the sinks, with the main loss term due to electron impact ionization. Regions of negative divergence of the energy flux thus correspond to regions with more ionization than heating, whereas regions of positive divergence correspond to regions with a net Ohmic heating of the electrons.

Figure 6.8 shows the time averaged axial energy flux over the central axis in the dusty discharge. We clearly see that the region with positive divergence ($\partial_z \bar{\Gamma}_{w_e,z} > 0$) lies inside the dust clouds. The central void corresponds with the region of negative divergence ($\partial_z \bar{\Gamma}_{w_e,z} < 0$). The energy flux is such that the heat produced in the dusty region is transported to the central void, where it is lost in ionizations.

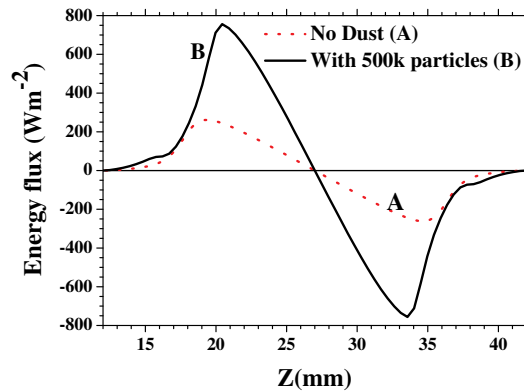


Figure 6.8: The axial electron energy flux (kW m^{-2}) along the central axis of the discharge. The heating in the cloud and the ionization in the void, together with the transport of the heat from the dust to the void is clearly shown.

In the dust-free discharge, the situation is similar, where the heat production in the pre-sheaths is also transported inwards, where it is lost to ionization, but in case of the dusty discharge it is much more pronounced.

Using equation 2.66 and assuming that the diffusion of electron energy density is negligible to the contribution of the drift in the electric field, we have

$$\Gamma_{w_e} = -\frac{5}{3}\mu_e w_e \mathbf{E}. \quad (6.9)$$

In the RF discharge, we can separate the electric field and the electron energy density in an average component and in a time-varying component, $w_e \rightarrow w_{e,0} + \tilde{w}_e$, $\mathbf{E} \rightarrow \mathbf{E}_0 + \tilde{\mathbf{E}}$. This way we can write

$$\begin{aligned} \Gamma_{w_e} &= -\frac{5}{3}\mu_e(w_{e,0} + \tilde{w}_e)(\mathbf{E}_0 + \tilde{\mathbf{E}}) = \\ &= -\frac{5}{3}\mu_e(w_{e,0}\mathbf{E}_0 + w_{e,0}\tilde{\mathbf{E}} + \tilde{w}_e\mathbf{E}_0 + \tilde{w}_e\tilde{\mathbf{E}}). \end{aligned} \quad (6.10)$$

Taking the time average of this, we find,

$$\overline{\Gamma_{w_e}} = -\frac{5}{3}\mu_e(w_{e,0}\mathbf{E}_0 + \overline{\tilde{w}_e\tilde{\mathbf{E}}}), \quad (6.11)$$

Our computations show that the final term is much smaller than the second term in most of the discharge, except in the sheaths¹. Therefore, it can be neglected here.

Using this to write out the left-hand side of equation 6.8, we find (with $w_e = n_e \epsilon$)

$$\nabla \cdot \Gamma_{w_e} = -\frac{5}{3}\mu_e \nabla \cdot (n_e \epsilon \mathbf{E}) = -\frac{5}{3}\mu_e \epsilon \mathbf{E} \cdot \nabla n_e - \frac{5}{3}n_e \mathbf{E} \cdot \nabla \epsilon. \quad (6.12)$$

We have dropped the bars and subscripts, since all quantities are time-averaged. In the above equation we have assumed that quasi-neutrality holds, $\nabla \cdot \mathbf{E} = 0$. The time averaged electric field points from the center to the walls. The gradient of the time averaged electron density points in the opposite direction. This means that the first term on the right-hand side of equation 6.12 is always positive. Therefore, the negative sign of the divergence of the heat flux from the dust clouds to the void is due to the gradient in the electron temperature acting together with the time averaged electric field.

¹Assuming a sinusoidal time dependence $\tilde{w}_e, \tilde{\mathbf{E}} \propto \sin(\omega t)$, we have $|\overline{\tilde{w}_e\tilde{\mathbf{E}}}| = \frac{1}{2}|\tilde{w}_e||\tilde{\mathbf{E}}|$ which is typically much smaller than $|w_{e,0}||\mathbf{E}_0|$.

6.5 Comparison with Particle-In-Cell/Monte Carlo calculations

We use our 1D PIC/MC model, with the same discharge dimensions and discharge settings as in the fluid model, to see whether the conclusions from our global hold, and to further investigate the role of the electron heating. We modelled three cases, one dust free discharge (corresponding to the discharge before dust particles are added), a discharge where the dimension of the void, as found with the fluid model, is homogeneously filled with dust particles, and finally the discharge after void formation.

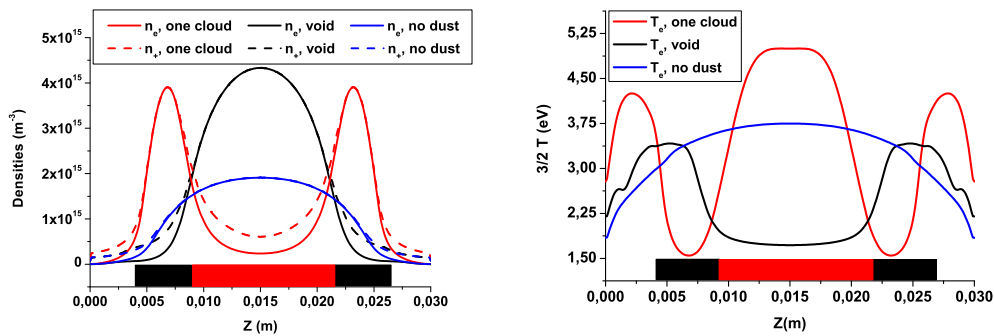


Figure 6.9: **Left:** The plasma densities for the three different cases. The red box indicates the dimension of the void filled with dust particles ('one cloud', red lines), or empty, but surrounded by dust clouds, indicated by the black boxes, to model a real void ('void', thick black lines). The blue lines correspond to a dust free discharge.

Right: The same as in the left figure, but here the electron temperature is plotted for the three cases.

Figure 6.9 shows the ion and electron densities for the three cases on the left, and the temperatures on the right. We see that the general conclusions of the global model are indeed confirmed, namely that the temperature inside a volume where there is electron depletion indeed rises. The average electron energy inside the dust free void is lower than in the case without void. Apparently, there is a large population of colder electrons inside the dust free void. The density inside the dust free void increases, compared to the dust free discharge, whereas it decreases for a homogeneous dust cloud, which is completely as expected from the global model.

It is interesting to see that the maximum in density for a homogeneous dust cloud occurs outside of the cloud, in between the cloud boundary and the elec-

trodes, and that the maximum in density corresponds to the minimum in temperature. Also, the temperature inside the dust free void is much lower than the temperature in the center of the dust free discharge.

Here we note that in the two-term Boltzmann solver used in the fluid code, it is assumed that the shape of the electron energy distribution function is always the same. This way, for one average electron energy (i.e. electron temperature $3k_B T_e = m_e \langle v_e^2 \rangle$), there is one value of the ionization rate. In the Monte Carlo approach, the electron energy distribution function can have many different shapes for one average electron energy, so that the ionization in the discharge, which is mainly determined by the high energy tail of the electron energy distribution function, can be different for the same value of the electron temperature. In this sense, there is not a direct correspondence between the electron temperature and the time averaged ionization profile calculated in the PIC/MC approach.

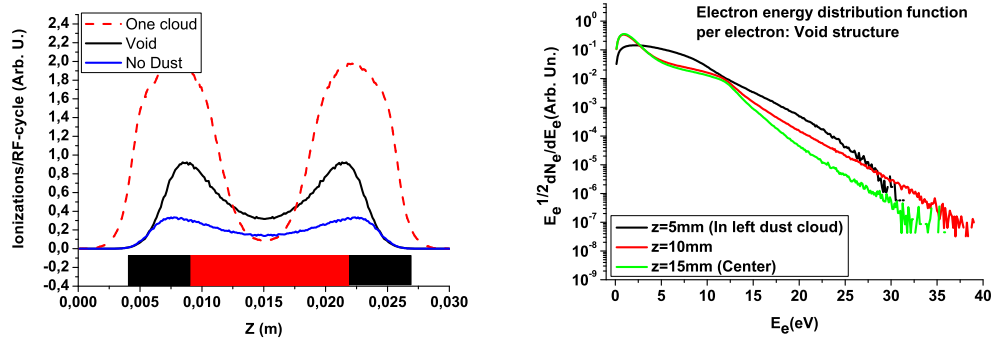


Figure 6.10: **Left:** The RF averaged electron impact ionizations for the three cases discussed.

Right: The EEDF for the dust free void calculation clearly shows the high energy tail in the cloud and the low energy population inside the void, indicating the non-local heating-ionization mechanism behind the void formation.

The latter is shown in figure 6.10 on the left. We can clearly see that inside the void, the ionization rate is lowest for the homogeneous dust cloud, despite the fact that the electron temperature is the highest in this case. In fact, for the dust free void simulation, the temperature is lowest, but the ionization rate the highest.

In order to understand the ionization profile, we show the electron energy distribution function (normalized to the total number of super electrons) for the dust free void calculation. The solid line shows the distribution inside the left dust cloud and the dotted line in the center of the discharge, in the center of the dust free void.

We see how in the dust cloud a high-energy tail exists, which is lost inside

the void. Inside the void there is a large population of cold electrons, which completely determines the average electron energy, and thus the electron temperature (the plots are logarithmic!), which is indeed lower inside the void. This low energy population consists of electrons after (several) ionization(s), which can no longer be heated due to the Ramsauer minimum. This cold population might be heated by Coulomb interactions between charged particles in the discharge, which are not included in our PIC/MC code.

6.6 Conclusions

A global model predicts an increase of the electron temperature when dust is added to a plasma. When the dust is homogeneous and no void forms, for instance during early stages of dust formation in chemically active plasmas, a decrease of the electron density is predicted. When more dust of larger size is added and a void forms, the dust starts acting as a wall and a rise of the electron density is predicted. These predictions are confirmed by a self-consistent two-dimensional fluid model, but an important effect is caused by the separation of the electron heating in the dust cloud and the ionization inside the void. Therefore, the electron density is not only influenced by a transition from volume recombination on the dust to a surface-like recombination on the dust, but also by a strong divergence of the heat flux, which grows for an increasing amount of dust in the discharge.

Our fluid model shows how in the dust-free discharge the electrons primarily pick up energy in the pre-sheaths. The ionization is highest in the center of the discharge, which is confirmed by the observations in [13]. When dust is added, the electrons are heated inside the dust clouds, due to the depletion there, but the ionization has a maximum inside the void. We have shown that the heat produced inside the dust clouds is transported to the void and results in plasma production there. The heat is transported by a growing gradient in the electron temperature, acting together with the electric field, and not by the gradient in the electron density in this field, since this acts in the opposite direction.

The PIC/MC calculations confirm the conclusions of the global model, namely that in regions of electron depletion, the average electron energy increases, whereas in a homogeneous dust cloud the density drops, and inside a dust free void the density rises. From these calculations it is also clear that the ionization inside the void is clearly a non-local phenomenon, which depends on the heating of electrons inside the dust cloud and the release of energy by ionizations inside the void. The high electron density inside the void mainly consists of low energy electrons, which are hardly heated due to the Ramsauer minimum, and which therefore do not contribute to the ionization.

Comparing our results with the observations mentioned in the motivation, we

conclude that indeed the electron temperature inside the void is lower than in the surrounding dusty area, but it is still higher than in the dust-free case. This elevated temperature is due to the transport of heat from the electron depleted regions, into the void. This, together with the increased electron density, causes the enhanced ionization, which is also observed in terms of enhanced optical emission during and after void formation.

References

- [1] J. -L. Drier, Ch. Hollenstein, and A. A. Howling, *J. Vac. Sci. Technol. A* **13** (3), 918 (1995)
- [2] G. E. Morfill *et al.*, *Phys. Rev. Lett.* **73**, 1598 (1999)
- [3] G. Praburam, and J. Goree, *Phys. Plasmas* **3** (4), 1212 (1996)
- [4] D. Samsonov, and J. Goree, *Phys. Rev. E* **59** (1), 1047 (1999)
- [5] J. Berndt, E. Kovačević, V. Selenin, I. Stefanović, and J. Winter, *Plasma Sources Sci. Technol.* **15**, 18-22 (2006)
- [6] M. Schulze, A. von Keudell, and P. Awakowicz, *Plasma Sources Sci. Technol.* **15**, 556-563 (2006)
- [7] Ph. Belenguer, J. Ph. Blondeau, L. Boufendi, M. Toogood, A. Plain, A. Bouchoule, C. Laure, and J. P. Boeuf, *Phys. Rev. A* **46** (12), 7923 (1992)
- [8] J. P. Boeuf, *Phys. Rev. A* **46** (12), 7910 (1992)
- [9] M. R. Akdim, and W. J. Goedheer, *Phys. Rev. E* **67**, 066407 (2003)
- [10] D. Samsonov, and J. Goree, *IEEE Trans. Plasma Sci.* **27** (1), 76 (1999)
- [11] J. Goree, G. E. Morfill, V. N. Tsytovich, and S. V. Vladimirov, *Phys. Rev. E* **59** (6), 7055 (1999)
- [12] I. Denysenko, K. Ostrikov, M. Y. Yu, and N. A. Azarenkov, *Phys. Rev. E* **74**, 036402 (2006)
- [13] M. Klindworth, O. Arp, and A. Piel, *J. Phys. D: Appl. Phys.* **39**, 1095 (2006)
- [14] C. Charles, R. W. Boswell, and M. A. Lieberman, *Phys. Plasmas* **10** (3), 891 (2003)
- [15] P. C. Boyle, A. R. Ellingboe, and M. M. Turner, *Plasma Sources Sci. Technol.* **13**, 493 (2004)
- [16] K. De Bleecker, A. Bogaerts, and W. Goedheer, *Phys. Rev. E* **70**, 056407 (2004)

7. Manipulating dust charge using UV light in a complex plasma

Abstract. *The coagulation of dust particles and their transport through a plasma depend mostly on their electric charge. In typical laboratory or industrial dusty plasmas, dust charging is dominated by the collection of electrons and ions from the plasma. Due to the high electron mobility, this charge normally is very negative. This confines the dust inside the discharge volume.*

In some processes, the presence of dust can have devastating effects, for instance in the plasma assisted fabrication of microchips. In the production process of solar cells, the inclusion of small crystalline clusters into the deposited layer during the process of plasma enhanced vapor deposition can have positive effects. It can for instance lead to an increased endurance against the harmful UV rays of the Sun. In order to control the presence of dust in the discharge, control over the charge on the dust is necessary, but without changing the optimal discharge settings.

In this chapter we study if a source of ultraviolet (UV) light can help to control the dust charge through the process of photo-detachment, without changing the plasma properties too much. We show that this is indeed the case for relevant dust particle sizes and densities, with only a moderate UV intensity of a few tens of Watts per square meter. For very high densities however, with corresponding high values of the Havnes parameter, the UV light can have the opposite effect. We end the chapter with an investigation to the dynamic response of a dusty plasma to a short pulse of ultraviolet radiation.

Based on :

IEEE Trans. Plasma Sci., **35**, 2, 280-285 (2007).

Authors :

V. Land, W. J. Goedheer

7.1 Motivation

Dust is important in many plasmas. Small particles are the nucleation cores around which noctilucent clouds (NLC) form. Radar observations show anomalous echoes, which are related to the charge on the small particles [1]. In star- and planet forming regions, dust grains are believed to coagulate to form the seeds of planets [2]. Small particles in a plasma usually obtain a negative charge, due to the high electron mobility and it is not clear how they coagulate at all. In fusion devices particles enter the plasma after energetic plasma-wall interactions, especially in the divertor region. These dust particles not only pose a safety hazard, but they can also have a strong negative impact on the performance of a fusion device [3, 4, 5, 6].

By contrast, in industrial plasmas, dust plays many different roles. In microchip production, chemical reactions in the plasma lead to the formation of dust, which can then hit the chip and damage the tiny structures built on the surface [7]. Then again, small particles included in the layers of polymorphous solar cells lead to higher efficiencies of the solar cells when exposed to sunlight, compared to solar cells without these inclusions [8].

Both the formation of dust through coagulation of smaller particles and the effect dust has on the plasma strongly depend on the dust charge. Controlling this charge will result in control over dust growth rates as well as influencing dusty plasma parameters. One could change the discharge settings to control the dust charge, such as the background pressure or the input power, but in industry these are set by economic demands.

Ultraviolet light might be a mechanism to control the particle charge in a dusty plasma. Ultraviolet light is present in the middle atmosphere, in space and in fusion reactors [9, 10, 11]. Through photo-detachment, electrons can be removed from dust particles. It is interesting to investigate whether introducing UV light to low-pressure discharges can lead to a significant change in the dust charge, without strongly changing the plasma parameters. Some work on the interaction of UV light with dusty plasmas has been done in the past, e.g. [12, 13], but we specifically study the effect of the UV on the dust charge, together with the effect on the discharge parameters. This chapter is based on calculations with a Particle-In-Cell/Monte Carlo code, which is described in chapter 2. The next section explains how the effect of photo-detachment was included in this model.

7.2 Photo-detachment in the model

An UV source with an intensity of \mathcal{I} (W m^{-2}), emitting photons of energy E_{UV} (J) through the powered electrode on the left side of the plasma chamber, with

a surface \mathcal{O} (m²), gives a number of UV photons entering the discharge in a RF cycle of length τ_{RF} (s) given by,

$$N_{UV} = \frac{\mathcal{I} \times \mathcal{O} \times \tau_{RF}}{E_{UV}}. \quad (7.1)$$

These photons will be absorbed and scattered by the dust particles in the clouds, leading to the total extinction of the light. When the dust particles are bigger than the wavelength of the incident light (which is the case here, for UV light of several hundred nanometers wavelength and particles of several micrometers in radius), Babinet's theorem says that the extinction cross section approaches two times the geometrical surface:

$$\lim_{R \gg \lambda} : \sigma_{ext} = \sigma_{sca} + \sigma_{abs} \rightarrow 2\pi R^2. \quad (7.2)$$

Furthermore, for strong absorbers (materials with large value of the imaginary part of the optical constant, $k > 0.5$) of this size, the scattering will be almost completely *forward scattering*, so that none of the light is lost from an incoming beam by scattering. Therefore we take $\sigma_{ext} \approx \sigma_{abs} \approx \pi R^2$ [14], since both amorphous silicon as well as amorphous carbon have such high values of k at these wavelengths ($k_C \approx 0.8$, $k_{Si} \approx 3.5$ at 4 eV incident photon energy [15, 16]).

The number of photo-detachment events in a dust cloud of width Δ , consisting of dust particles with radius R at a density n_D , is given by the Lambert-Beer law,

$$N_{pd} = N_{UV} \times (1 - \exp(-n_D \sigma_{ext} \Delta)). \quad (7.3)$$

We thus ignore any dependence of the efficiency of photo-electron detachment on both the UV photon energy, as well as the angle between the incoming photon and the normal at the dust particle surface.

These photo-detachment events are then randomly distributed over the dust cloud. The number of UV photons incident on a dust cloud behind the first one is somewhat reduced, since a small fraction of the total UV light is absorbed in this first dust cloud. For high density clouds the number of events can therefore be different for both clouds.

We assume that the electrons on the dust form a loosely bound electron gas, similar to electrons in the valence band in metals. They are therefore distributed according to a Fermi-Dirac distribution, $n(E_e) \propto (1 + \exp((E_e - E_F)/kT_e))^{-1}$, where E_F is the energy level of the electron with the highest energy in the gas, called the Fermi energy. The energy distribution of photo-detached electrons when they leave the dust particles is then a convolution of this distribution with the *boundary transmission coefficient*, $D(E_e)$ of the dust particles [17]. We ignore this latter function and put it equal to unity, since the dust particles are bound close to the particle surface, and are likely to escape the surface collisionless.

Since the Fermi distribution is computationally difficult to invert, we approximate the energy distribution, E_i , of the bound electrons by a triangular distribution, which is shown in figure 7.1. It can be compared to the experimentally measured energy distributions in [18].

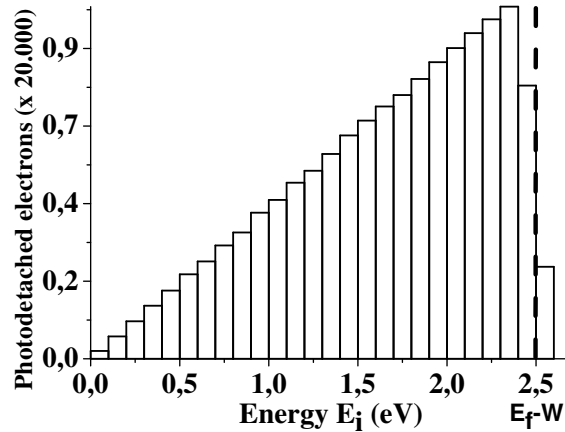


Figure 7.1: A histogram of the energy distribution, E_i , of the photo-detached super electrons after several hundreds of calculated RF cycles. The photon energy $E_f = h\nu$ is 4 eV and the workfunction W is 1.5 eV.

The electrons ejected are repelled by the dust and gain the floating potential of the dust particles with respect to the surrounding plasma, calculated from the charge on the dust particles. So the final energy of the photo-detached electrons, far away from the dust particles is given by, $E(eV) = E_i + |\phi_D|$ [19].

Typically, the simulations were run for several thousands of RF cycles (or hundreds of microseconds). Typical charging times for isolated dust particles with a radius of $R \sim 5\mu\text{m}$, at plasma densities considered here, and for ions at room temperature are a few microseconds [20, 21]. This means that our simulations were run much longer than the dust charging time and the results shown are representative for the equilibrium situation.

7.3 Results

We present results for two different dust densities. The first discharge includes dust clouds with a density of $6 \cdot 10^{10} \text{ m}^{-3}$, a typical value for dust clouds in front of the electrodes in RF experiments. The second discharge is rather extreme, with a ten times higher dust density. For both, the particle radius is $5 \mu\text{m}$ and work function, $W = 1.5 \text{ eV}$. The neutral pressure is 100 mTorr (13 Pa). The

driving potential is 70 V at 13.56 MHz. The radius of the electrodes is 9.4 cm, the (vertical) distance between the electrodes is 5 cm, so that $L = 0.05$ m.

7.3.1 Low dust density results

We distinguish three cases (**1**, **2**, **3**). **1** is with the dust clouds present, but without incident UV light. It is represented by a dashed line in all the graphs. **2** has incident UV light added, at an UV energy of 4 eV and an intensity of 25 W m^{-2} , and is represented by a dotted line. **3** is the case for high energy photons, with $E_{UV} = 16 \text{ eV}$ at an intensity of 100 W m^{-2} , which is represented by the thick solid line.

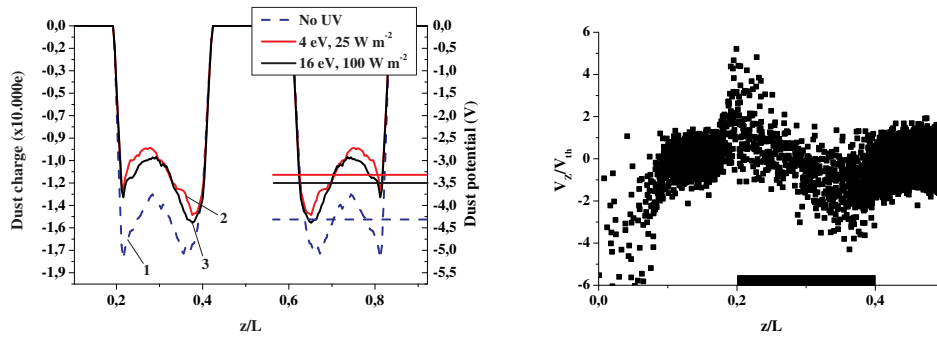


Figure 7.2: **Left:** The dust charge in elementary charges, for the case without UV (**1**) and the cases with low energy UV (**2**) and with high energy UV (**3**). We see that the number of electrons residing on the dust is strongly reduced by the photo-detachment. The right axis shows the dust particle potential, and the horizontal lines indicate the average values found.

Right: Phase-space plot of the superions near the left dust cloud, with the axial velocity normalized to the thermal velocity of $V_{th} \sim 400 \text{ m s}^{-1}$. The ions are accelerated from the void and the space in front of the electrodes into the dust cloud. Typical thermal Mach numbers are 2 to 6. This acceleration of the ions results in the charge gradients throughout the dust clouds. The black square shows the position of the left dust cloud.

Figure 7.2 shows the dust charge for the three cases **1**, **2**, and **3** in the left panel. We see that the UV photons strongly reduce the amount of electrons residing on the dust particles. In both cases **2** and **3** the reduction in the dust charge is approximately 25 %, which corresponds to a reduction in the dust potential of about 1 Volt. We see that the low energy UV case has a slightly stronger effect.

The gradients in the dust charge are not due to computational noise, which is much smaller. They arise due to acceleration of ions from the void into the dust

cloud and a similar acceleration from the region in front of the electrodes into the opposite side of the dust cloud. This is shown in the right panel of figure 7.2. Since the OML ion current is proportional to $(1 - e\phi_D/E_+)$ the dust charge is more negative on the outside of the dust clouds, where the ions are streaming fastest (and hence the mean ion energy E_s the largest). This acceleration is consistent with results obtained with the fluid models in chapter 5. The average dust charge of approximately $15.000e$ in the case without UV corresponds very well with the experimental result of 3 electron charges per nanometer radius [22].

A population of photo-detached electrons clearly escapes the dust cloud in case **3**, accelerated by the same electric field that pulls the ions in. This can be seen from the bumps in the electron energy distribution function inside the left cloud (figure 7.3, left panel) and at the center of the discharge (figure 7.3, right panel). Their energy is roughly 18 eV, which corresponds to $E = E_i + e|\phi_D| \approx 16 - 1.5 + 3.5 = 18$ eV. This energy is much higher than the repelling dust potential, which means that a fraction of the photo-detached electrons will be recaptured by nearby dust particles. The variation of the dust charge together with diffusion in energy space causes a broadening of the bumps.

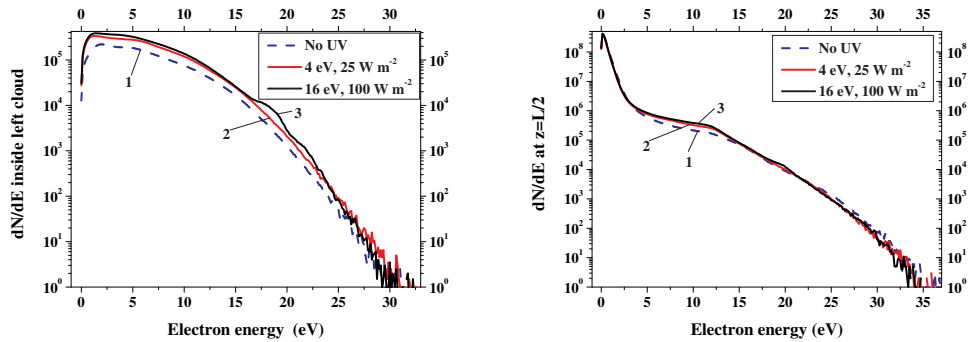


Figure 7.3: **Left:** The electron energy distribution function in the left cloud. Case **3** shows a broad bump of photo-emitted electrons. In case **2** the photo-emitted electrons cause an increase around 6 eV, which is hard to see.

Right: The electron energy distribution function in the center of the discharge. Case **3** shows a small bump of photo-emitted electrons which escaped the cloud. Electrons involved in exciting and ionizing background neutrals cause an increase in the low energy population too. Case **2** is almost similar to case **1**, mainly showing more low energy electrons.

In case **2** the photo-detached electrons obtain an energy of 6 eV. The amount of electrons around that energy is much higher, so that the contribution of the photo-detached electrons to the electron population at that energy is small.

When the photo-detached electrons escape the dust cloud, they add to the conductivity of the plasma, which reduces the Ohmic heating and thus the ionization. The plasma density in the center of the discharge decreases from $2 \cdot 10^{16} \text{ m}^{-3}$ without UV to $1.2 \cdot 10^{16} \text{ m}^{-3}$ for both case **2** and **3** with UV. In case **3** the detached electrons have enough energy to excite and ionize the background gas. This is also reflected in the total ionization in the discharge, as shown in figure 7.4, which is somewhat higher in this case.

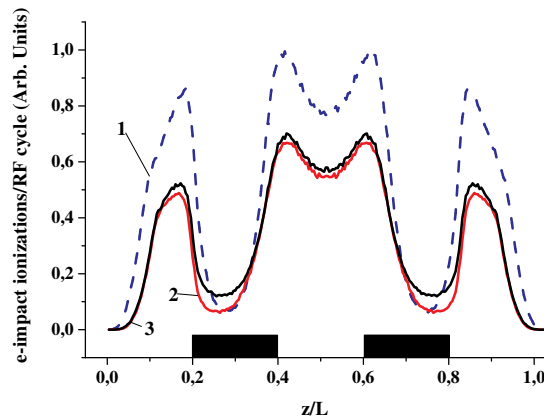


Figure 7.4: The time averaged number of ionizations. The reduction in Ohmic heating causes an overall reduction of the ionization level in case **2** and **3**. However, the photo-detached electrons in case **3** do contribute to the ionization, which can be best seen inside the dust clouds, indicated by the black squares on the horizontal axis.

The ionization is highest inside the void and between the electrodes and the dust. This corresponds to the observed change in optical emission from the plasma after void formation [23]. The change in dust charge also causes a small change in the acceleration of the ions into the dust clouds. This causes a slight change in the dust charge between case **2** and **3**, together with the fact that a higher fraction of the photo-detached electrons is recaptured by nearby dust particles in case **3**.

7.3.2 High dust density results

Finally, we show the results for a rather extreme case. The dust density in this section is ten times higher than the density in the section above. This high density results in a very strong depletion of electrons from the plasma, which corresponds to a very high value of the Havnes parameter, $\mathcal{P} = n_D Z_D / n_e$, which is bigger

than 40 throughout the cloud. This leads to a strong reduction in the dust charge, which is discussed in [24, 25], and is also seen in figure 7.5 on the left side.

The acceleration of the ions is even larger, which results in larger charge gradients. It should be noted that in this run, we had to decrease the width of the dust clouds, otherwise the run without UV light died out, due to the strong depletion.

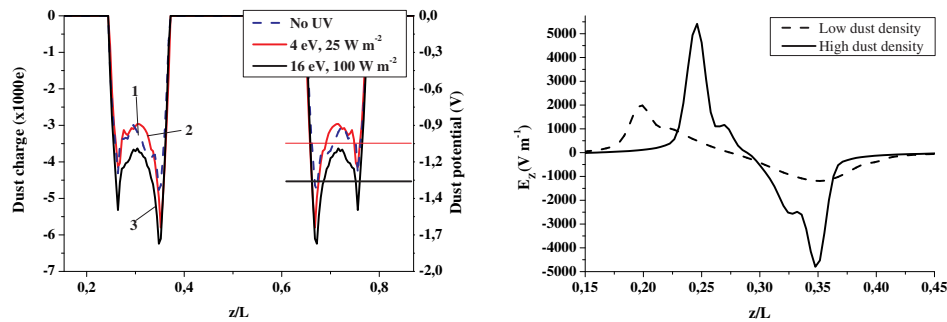


Figure 7.5: **Left:** The dust charge similar to the cases in figure 7.2. We see that the effect of photodetachment is limited. In fact, the high energy UV case results in *more* electrons attached to the dust. Note the difference in scale of the left axis with respect to the scale in figure 7.2.

Right: The electric field in the left dust cloud (between $z/L=0.2$ and $z/L=0.4$ for the low density cloud and between $z/L=0.25$ and $z/L=0.35$ for the high density cloud). The strong electric field in the high density cloud accelerates the photo-detached electrons.

The two dust clouds really act like walls, with strong electric fields close to and inside the dust cloud, similar to the sheaths in front of the electrodes. On the righthand side of figure 7.5, the axial electric field in the left cloud is shown. Due to the high density and the strong depletion the electric field is three times higher in the high density cloud than in the low density cloud.

These strong electric fields accelerate the photo-detached electrons to the outside of the clouds. Due to the high Havnes parameter, and the low dust charge, most electrons are directly recaptured, but the ones that do exit the cloud become very energetic and excite and ionize the background gas. The electrons in the plasma volume also heat up due to the strong electric field at the cloud edge. These hot electron populations are also seen in figure 7.6, on the left, and 7.6 on the right. The increase in ionization outside of the cloud is clear in figure 7.7.

The photo-detached electrons in the high energy UV case also cause an increase of ionization *inside* the cloud, in fact the ionization in the cloud increases by a factor of four. The electrons are accelerated in the high electric field and

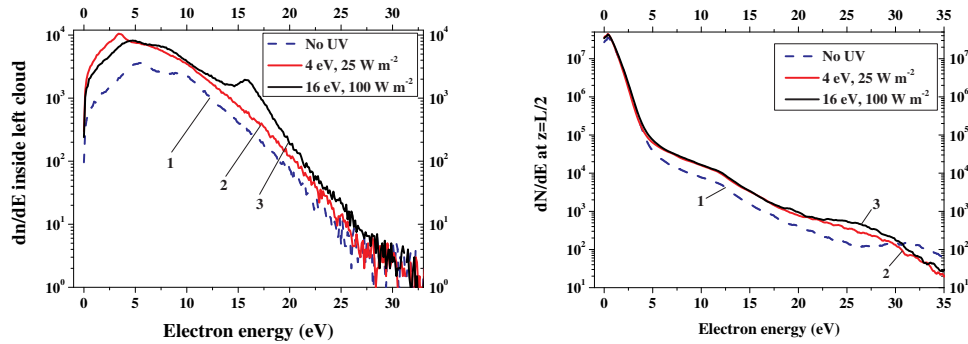


Figure 7.6: **Left:** The electron energy distribution function in the left high density cloud.

We can see a big contribution of photo-detached electrons at higher energies in the high UV energy case, **3**.

Right: The electron energy distribution function halfway the discharge. The number of high energy electrons increases when UV light is added, resulting in more electron impact ionizations.

are recaptured by the dust cloud with high probability at such high values of the Havnes parameter. The chance for the ions to be collected is reduced in this high density cloud. The final result is an *increase* in the amount of electrons carried by the dust for the high energy UV source. The additional ionization outside of the cloud increases the plasma density from $3 \cdot 10^{16} \text{ m}^{-3}$ without UV to $3.5 \cdot 10^{16} \text{ m}^{-3}$ with high energy UV.

7.4 Response to a short pulse of UV light

The previous sections dealt with the effect of ultraviolet light on the equilibrium properties of a dusty plasma. In this section we will see how a dusty plasma responds to a short pulse of ultraviolet light. We will focus on the time it takes for the system to go from one equilibrium to the next and will especially focus on the response of the dust charge, the plasma densities and the electron temperature.

7.4.1 Dust charge response

The dust potential response to the pulse of UV light is shown in figure 7.8. In the graph, $T=0$ corresponds to the switch-on of the UV pulse. Switch-off is at 0.37 milliseconds. Another 0.37 milliseconds later the simulation was ended. We see that the jump from the initial equilibrium without UV, with a dust charge fluctuating around roughly -4.7 V , to the equilibrium with UV, which fluctuates

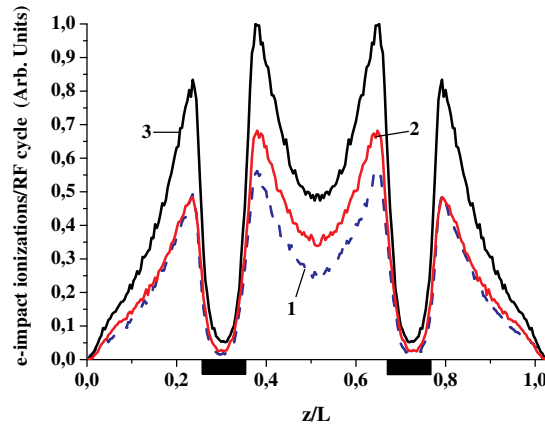


Figure 7.7: The averaged amount of (super-)ionizations per RF cycle. The profile shape remains the same, but the level of ionization increases when UV light is added, due to the acceleration of the photodetached electrons in the strong electric fields near and in the high density clouds.

around a dust potential of roughly -3.8 V, is very rapid and happens within 50 microseconds. The jump after UV switch-off is also rapid.

A closer look at the beginning and the end of the pulse is shown in figure 7.9. We fitted the response of the dust potential with a typical exponential RC response. We see that the $1/e$ time at UV switch-on is a little under 3 microseconds, whereas the $1/e$ time at UV switch-off is almost 20 microseconds.

7.4.2 Plasma response

When the UV is switched on, we see a decrease in the number of free electrons in the discharge, as shown in figure 7.10. The decrease can be very well fitted by an exponential decay, with a typical $1/e$ time of $30 \mu\text{s}$. It is clear that the plasma takes a much longer time, about 15 times longer, to settle to the presence of the UV light than the dust charge.

When the UV is then switched off, the number of plasma particles returns to the initial value. This can also be very well approximated by an exponential response with an even longer time scale of $40 \mu\text{s}$, but this time is only 2 times longer than the time scale of the dust potential. It is clear that the changes in plasma parameters can not really play an important role in the response of the dust charge to the switch-on of the UV source. This is totally dominated by the quick change in charging currents, according to OML theory, which will be derived below.

Since there is a change in electron population, there will be a change in the

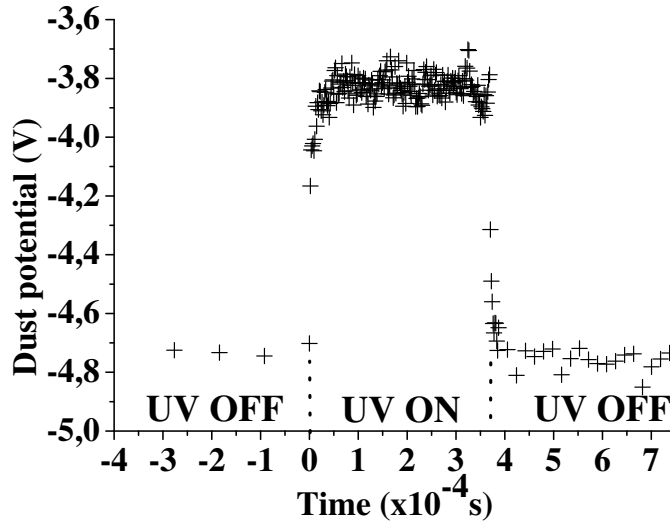


Figure 7.8: The response of the dust potential to a 0.4 millisecond long pulse of UV light.

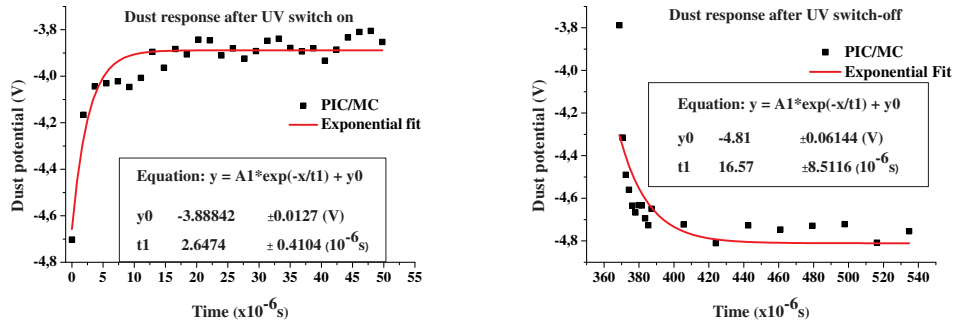


Figure 7.9: **Left:** The dust response directly after the UV switch-on, which shows that the response of the average dust potential is really fast, with a 1/e time of under 3 microseconds.

Right: The same response after UV switch-off, which shows that the relaxation to the initial equilibrium without UV takes much longer, almost 20 microseconds.

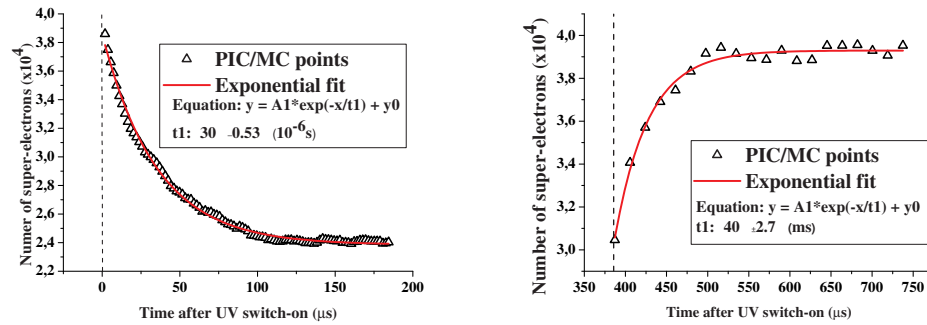


Figure 7.10: **Left:** The number of super-electrons in the discharge after switch-on of the UV pulse, and an exponential fit to calculated points. **Right:** A similar graph, but now for the response after UV switch-off.

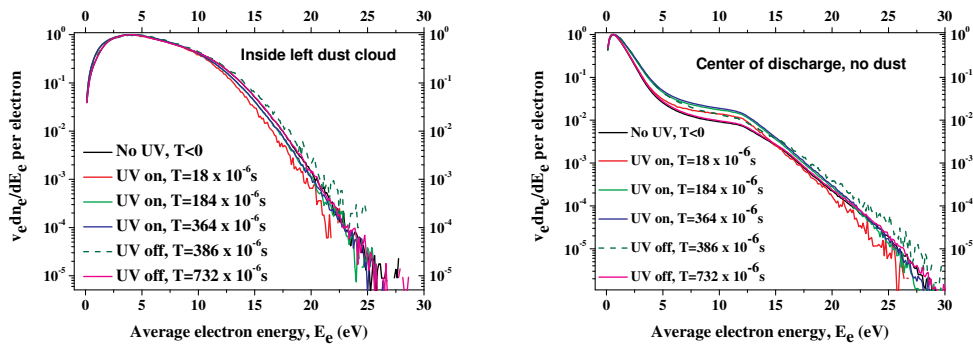


Figure 7.11: **Left:** The electron energy distribution function in the left cloud for different times during the UV pulse. **Right:** The same as on the left, but now for the center of the discharge, inside the dust free void.

electron energy distribution functions as well. Similar to the previous sections, we show the EEDF's inside the left cloud and in the center of the discharge (the void) in figure 7.11, but we have normalized them to see the average response of one electron to the changes.

It is clear that on UV switch-on, the plasma cools down, resulting in a lower population of the high-energy tail, both in the dust clouds as well as in the dust free region in the center. We see there is a strong increase of the low energy population inside the dust free region. On UV switch-off, there is a sudden heating of the plasma, after which the plasma returns to its initial electron energy distribution. Apparently, the temporary mismatch between the dust charge and the surrounding space charge at UV switch-on and switch-off, causes electric fields which heat the electrons, until equilibrium is reached.

When we look at the ionization profile, we see that on UV switch-off there is a drop in the level of ionization in the discharge, which then slowly rises to an equilibrium level, which is below the ionization level without UV, see figure 7.12. When the UV is switched off, there is a sudden rise in the ionization, even above the level without UV, which then decreases back to that level. This is due to the cooling and heating of the plasma, as discussed before.

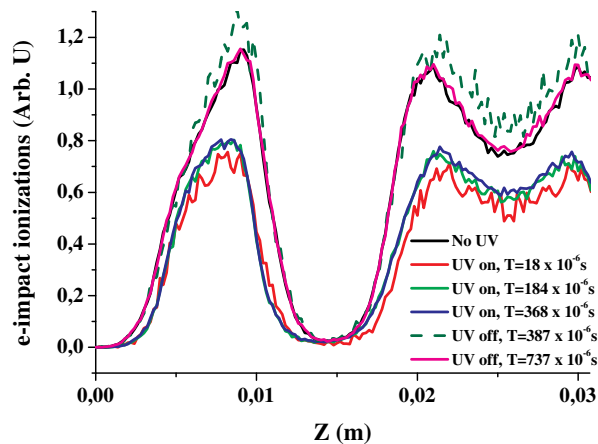


Figure 7.12: The ionization level at different times during the UV pulse. For clarity, only half the discharge is shown. The complete solution is symmetric.

We can conclude that the response of the dusty plasma to the UV pulse is very quick and that the final equilibrium is again obtained. Still, during very short time scales after switch-on and switch-off there is a small overshoot in ionization. This comes from the fact that the plasma needs more time, several tens of microsec-

onds, to adapt to the change in dust charge, determined by the losses of plasma, whereas the charging currents to the dust adapt on timescales of a microsecond, according to OML theory. This difference in time-scales causes a mismatch between the dust charge and the plasma, which is the source of electric fields which heat the plasma.

7.4.3 Time scales and plasma shut-down

Three time scales are important for the de-charging of the dust [26], namely the charging time derived from OML theory τ_z (see chapter 2), the plasma loss timescale τ_L , which consists of losses on the dust through recombination, with a corresponding timescale τ_A , and the (ambipolar) diffusion timescale τ_D ($\tau_L = (1/\tau_A + 1/\tau_D)^{-1}$), and finally the electron temperature relaxation timescale, τ_T .

The initial charging timescale is found from OML theory as

$$\tau_z^0 = \frac{\sqrt{2\pi}\lambda_{+,0}^2}{v_{T,+}r_D(1+z_{eq}^0)}, \quad (7.4)$$

with $z_{eq}^0 = e^2Z_0/r_DT_{e,0} \sim 1.5$, $\lambda_{+,0}$ the ion Debye length, $\sim 4 \cdot 10^{-5}$ m and $v_{T,+}$ the ion thermal speed $\sim 10^2$ m s $^{-1}$. We thus find $\tau_z^0 \sim 3$ μ s. For the initial diffusion timescale, we have

$$\tau_D^0 = \frac{3\sqrt{\pi}\Lambda_D^2}{(2\sqrt{2}(n_N\sigma_{+N})^{-1}v_{T,+})(1+\frac{T_{e,0}}{T_N})}, \quad (7.5)$$

with $(n_N\sigma_{+N})^{-1}$ the ion mean free path $\sim 10^{-4}$ m, Λ_D typical diffusion length scale $\sim 5 \cdot 10^{-3}$ m. This leads to a diffusion time scale $\tau_D^0 \sim 46$ μ s. The initial dust recombination timescale equals

$$\tau_A^0 = \frac{1}{2\sqrt{2\pi}r_D^2N_Dv_{T,+}\left(1+z_{eq}^0\frac{T_{e,0}}{T_N}\right)}. \quad (7.6)$$

Our dust density $N_D = 5 \cdot 10^{10}$ m $^{-3}$ and dust particle radius $r_D = 5 \cdot 10^{-6}$ m, which gives $\tau_A^0 = 11$ μ s. Therefore, the loss time scale $\tau_L \approx \tau_A \sim 9$ μ s. In a low pressure argon discharge, electrons mainly lose energy in inelastic electron-neutral collisions. The time scale for energy relaxation is given by

$$\tau_T^0 = \frac{1}{2}\sqrt{\frac{m_+}{m_e}}\frac{l_{eN}}{v_{T,+}}\sqrt{\frac{T_N}{T_e}}, \quad (7.7)$$

with $l_{eN} = (n_N\sigma_{eN})^{-1} \sim 3 \cdot 10^{-2}$ m, which is comparable to the size of the discharge. Of course the energy of electrons able to undergo inelastic collisions

has to be at least 11.2 eV. We find $\tau_T^0 \sim 500 \mu\text{s}$. For the initial dusty plasma in equilibrium, we thus have $\tau_z^0 \lesssim \tau_L^0 \sim \tau_A^0 < \tau_D^0 < \tau_T^0$.

We see that in equilibrium, the fastest time is the charging time. The response of the dust potential to the switch-on of the UV pulse is on this timescale. In the new equilibrium, with UV, the main change in parameters is a slight rise in electron temperature and density, and a change in z_{eq} . This results in a change in the charging time, $\tau_z^1 \sim 1.8\tau_z^0 \approx 4 \mu\text{s}$. The other time scales remain almost the same.

For comparison, the response of the dust charge to a complete shut-down of the discharge is shown in figure 7.13. This response is due to changes in plasma parameters by the diffusion of the plasma towards the outsides of the discharge, which is a slower, ambipolar process.

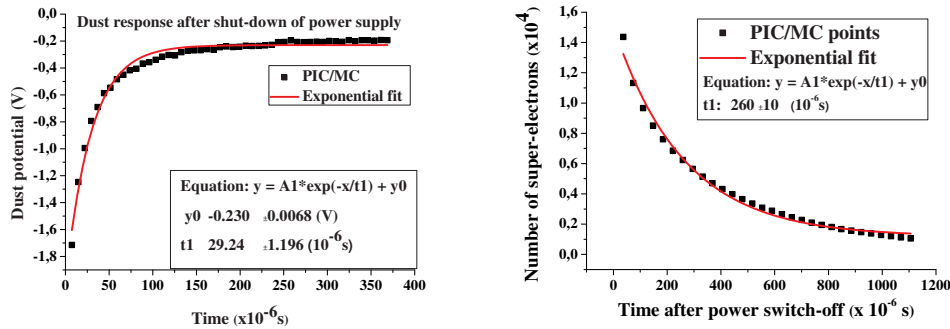


Figure 7.13: The dust charge after shut down of the discharge. The slow response is due to the slow change in plasma parameters, which comes from the electron energy relaxation and the ambipolar diffusion of plasma to the outer walls. The decay of the plasma is shown on the right.

In [26], it was found that the typical time scale of dust particle charging was on the order of $1 \mu\text{s}$, whereas the timescales for electron temperature relaxation and plasma losses (due to ambipolar diffusion) both were in the range of $30\text{-}60 \mu\text{s}$. Our findings correspond well with the findings of Ivlev *et al.*, except for the time scale of recombination on the dust, which we find to be an order of magnitude smaller than the diffusion time scale, which also makes the loss time much shorter.

Also interesting here is the fact that the exponential fit to the (de-)charging curve does not give a neutral dust distribution at infinite time. In [26] similar experiments were described on the de-charging of a dusty plasma after power shut down, and indeed a rest charge was found, which was according to calculations $1.6 \times 10^{-2} \times Z_{D,0}$. According to their calculations, the dust charge hardly changes up to $t \sim 10\tau_T^0$, whereas the rest charge should be reached after $t \sim 100\tau_T^0$. These numbers correspond to $500 \mu\text{s}$ and 5 milliseconds respectively. The latter might be

true, since we have not reached their value of the rest charge yet, but the first does not seem to be true in our case. We see a significant decrease of the dust potential within the first few hundred microseconds after shut down of the plasma.

7.5 Conclusions

Photo-detachment by UV photons strongly reduces the dust charge in a low-pressure complex plasma for dust densities relevant for experiments and applications, already at source intensities of a few tens of Watts per square meter and an UV energy of a few electronvolts above the workfunction. For these values of the dust density ($\sim 10^{10} - 10^{11} \text{ m}^{-3}$) most photo-detached electrons simply escape the cloud with low kinetic energy, resulting in a reduced Ohmic heating. The ionization degree is lower when UV is added. A small fraction of the electrons detached by high energy photons can excite and ionize the background gas, however. This is seen as a slightly higher ionization level in the discharge.

When the dust cloud is very dense ($10^{11} - 10^{12} \text{ m}^{-3}$), and hence the depletion of electrons on the dust very large, which corresponds to a high value of the Havnes parameter, the average dust charge is lower. Strong electric fields arise inside the cloud. Electrons detached from the dust are accelerated in these electric fields. Therefore, more detached electrons have enough energy to be recaptured by the dust particles, which is enhanced by the high density. Also, more electrons are able to excite and ionize the background gas, which results in a higher level of ionization in the discharge. The added electrons can be recaptured by the dust, whereas the ions hardly can, which even results in an increase of the number of electrons attached to the dust in case of high energy UV photons.

In conclusion, low energy (a few eV) UV sources at intensities of a few tens of W m^{-2} , provides an interesting tool to control the dust charge, without changing the plasma parameters strongly, at dust densities which are relevant for many dusty plasma experiments and applications. This might ultimately lead to a tool to actively control and manipulate dusty plasmas or dust formation rates, both in experimental as well as industrial low-pressure discharges. The mentioned intensities and UV energies are well within the reach of modern commercial UV-sterilization or curing devices. These devices could very well be used in dusty plasma experiments to study the effect of photo-detachment on low pressure discharges. In dusty plasmas with very high values of the Havnes parameter, the added UV light does not decrease the dust charge and can even lead to an increase in the number of electrons attached to the dust particles.

Dusty plasma respond very quickly to a short pulse of UV light. The switch-on changes the charging currents first, on a time scale of 1 microsecond. The plasma needs much longer to adapt towards the new equilibrium, on a diffusion

timescale. The mismatch causes heating of the electrons. Switch-off involves the change in plasma parameters and not just the change in charging currents. It has a slower response of 15 microseconds. The plasma does return to the initial equilibrium. If the discharge is turned off completely, the response is due to the change in plasma parameters only, dictated by the electron energy relaxation and the ambipolar losses of plasma, on a timescale of roughly 30 microseconds for the dust potential.

On average, the dust keeps a negative charge of roughly $4 \times 10^{-2} \times Z_{D,0}$. This charge will remain until the screening length in the plasma equals the diffusion length, so that quasi-neutrality no longer holds, and the ions and electrons start diffusing independently. This happens when the plasma density has dropped to $n_* : n \rightarrow n_0 \lambda_{+,0}^2 / \Lambda_D^2 \sim 10^{-5} n_0$, which happens for $t > 100 \tau_L^0 \ln n_*^{-1} \sim 10^3 \tau_L^0 \sim 4$ milliseconds [26]. Our calculations do indeed indicate that the final dust charge is less negative than the value of the exponential fit, but at the end of our calculation, the plasma was still in the ambipolar stage.

References

- [1] O. Havnes, T. Aslaksen, and A. Brattli, *Phys. Scr.* **T89**, 133-137 (2001)
- [2] J. Blum *et al.*, *Phys. Rev. Lett.* **85**, 2426 (2000)
- [3] J. Winter, *Plasma Phys. Control. Fusion* **40**, 1201-1220 (1998)
- [4] J. Winter, G. Gebauer, *J. Nucl. Mater.* **266-269**, 228-233 (1999)
- [5] J. Winter, *Phys. Plasmas* **7**, 3862-3866 (2000)
- [6] J. Winter, *Plasma Phys. Control. Fusion* **46**, B583-B592 (2004)
- [7] G. S. Selwyn, J. Singh, and R. S. Bennet, *J. Vac. Sci. Technol. A* **7**, 2758 (1989)
- [8] P. Roca i Cabarrocas, *J. Non-Cryst. Solids* **266-269**, 31 (2000)
- [9] K. L. Coulson, *Solar and terrestrial radiation*, (Academic Press, New York 1975)
- [10] J. Bally, R. S. Sutherland, D. Devine, and D. Johnstone, *Astrophys. J.* **116**:293-321 (1998)
- [11] R. C. Ister, R. W. Wood, C. C. Klepper, N. H. Brooks, M. E. Fenstermacher, and A. W. Leonard, *Phys. Plasmas* **4**, 355 (1996)
- [12] M. Rosenberg, D. A. Mendis, and D. P. Sheehan, *IEEE Trans. Plasma Sci.* **24**, 1422 (1996)
- [13] A. A. Samarian, O. S. Vaulina, A. P. Nefedov, V. E. Fortov, B.W. James, and O. F. Petrov, *Phys. Rev. E* **64**, 056407 (2001)
- [14] E. Krügel, *The physics of interstellar dust*, (Institute of Physics Publishing, Series in Astronomy and Astrophysics, Bristol, 2003)
- [15] G. Compagnini, *Applied Optics* **33**, 7377 (1994)
- [16] G. E. Jellison, Jr. and F. A. Modine, *J. Appl. Phys.* **5**, 3745 (1982)
- [17] R. H. Fowler, *Phys. Rev.* **38**, 45 (1931)
- [18] D. T. Pierce, and W. E. Spicer, *Phys. Rev. Lett.* **27**, 1217 (1971)

- [19] A. Simon (Ed.) and W. B. Thompson (Ed.), *Advances in Plasma Physics, Volume 4* (Interscience Publishers, New York 1971)
- [20] E. C. Whipple, Rep. Prog. Phys. **44**, 1197 (1981)
- [21] A. Bouchoule (ed.), *Dusty Plasmas: Physics, Chemistry, and Technological Impact in Plasma Processing* (John Wiley & Sons, Chichester, 1999)
- [22] W. W. Stoffels, E. Stoffels, G. H. P. M. Swinkels, M. Boufnichel, and G. M. W. Kroesen, Phys. Rev. E **59**, 2302 (1999)
- [23] D. Samsonov, and J. Goree, Phys. Rev. E **59**, 1047 (1999)
- [24] O. Havnes, C. K. Goertz, G. E. Morfill, E. Grün, W. Ip, J. Geophys. Res. **92**, 2281 (1987)
- [25] S. Ratynskaia *et al.*, Phys. Rev. Lett. **93**, 085001 (2004)
- [26] A. V. Ivlev *et al.*, Phys. Rev. Lett. **90**, 055003 (2003)

Summary

Most parts of the visible universe consist of plasma. It is quite extraordinary that we are not confronted with plasma very much in our every day life. Plasma is found in interstellar space, in large molecular clouds, in stars and in the solar system, in planetary atmospheres, in the polar lights and in lightning. Plasmas are used for instance in the fabrication of microchips and solar cells. They are also of use in many coating processes, e.g. to make plastics more scratch-resistant, or to improve the wettability of medical or dental implants. Surfaces are cleaned with plasmas, for instance during the cleaning of medical equipment, but plasma is also used in fluorescent lighting, neon lighting and in plasma screen techniques. Finally, plasma is used in the concept of tokamak fusion devices, in which the plasma is confined by magnetic fields in a toroidal chamber and heated until hydrogen isotopes fuse to generate energy.

Sometimes, dust forms in plasma, either through chemical processes in the volume or at plasma-wall interfaces, or through direct physical sputtering of particles from the wall, for instance in the divertor regions of a tokamak fusion device¹.

This dust can have many effects on the plasma processes involved. For instance, the inclusion of nano-crystalline particles in polymorphous silicon solar cells improves the efficiency of the cells when exposed to sunlight by reducing the Staebler-Wronski effect. In microchip industry, dust particles are usually referred to as “killer particles”. They can hit the chip surface and destroy the nanometer sized components on these surfaces. In fusion devices, the role of dust particles is not completely clear, but they might play an important role in the retention of tritium. Finally, dust plays an important role in the formation of stars and planets, often in environments with both magnetic fields and ultraviolet radiation.

In this thesis, research about the behavior of and control over dusty plasma is presented, especially in the presence of magnetic fields or ultraviolet light. The results were obtained with the use of numerical models, and partly by experimental measurements. We used a two-dimensional dusty fluid model and applied it to

¹The divertor is, so to say, the ashtray of a fusion device, where all the rest products are guided to by the magnetic fields.

radio frequency (RF) discharges under micro-gravity conditions in which micrometer sized dust particles are added in order to understand the properties of dusty plasmas.

In this model, the plasma parameters are solved, with sub-RF time steps, using a drift-diffusion approximation for the particle fluxes in the electron and ion density balance, and for the electron energy density flux in the electron energy density balance. The solution of these equations requires the electric field, which is found by solving the Poisson equation. The transport of the dust is computed by solving the radial and axial component of the sum of all the forces, including the electrostatic force, ion drag, and the thermophoretic force. Subsequently, a drift-diffusion type of equation is found by balancing these forces with the neutral drag force and by including the compressibility of the dust.

The computation of these forces requires the charge on the dust, which is solved by computing the balance between the electron and ion currents, calculated according to Orbital Motion Limited theory, with the plasma parameters as input. The corresponding recombination rate is used as a sink for particles and energy in the plasma equations. This, and the contribution to the Poisson equation by the dust charge density, couples the dust to the plasma parameters. The coupling between the sub-RF time steps used for the plasma and the much larger time steps used for the dust transport is solved in the code, making it completely self-consistent.

We extended the model with a homogeneous axial magnetic field and studied the effect of this magnetic field on the transport of dust in a micro-gravity discharge and on the formation of a dust free void in such a discharge in chapter 3. We showed that the change in ion transport through ambipolar diffusion, even with magnetic fields too low to magnetize the ions directly, causes a strong change in the dust transport. The time it takes to form a dust free void is much shorter when a magnetic field is applied.

At Auburn University, in the United States of America, we made a setup and performed measurements on the response of a dusty plasma to an applied magnetic field in a DC discharge. We show in chapter 4 that both the plasma and the dust components show a drift in the $\mathbf{E} \times \mathbf{B}$ direction and that the response of the dust component consists of two parts, an initial fast part and a later slow part.

A central role in the transport of dust is played by the ion drag force, which depends on the screening of the dust particles by the surrounding plasma, on collisions between the ions and the neutrals and on the ion drift speed. We extended the model by including recent theories on the ion drag force and showed in chapter 5 that in typical micro-gravity experiments, the non-linear scattering of the ions is the most important effect, and that the ion drift speed and ion-neutral collisions play a minor role in the calculation of the ion drag force. These collisions can be important for the charging of the dust particles in these discharges, however.

An important effect of dust in a plasma is that it acts as a sink for electrons and ions. This has an important effect on the heating of the electrons. The dust free void observed in micro-gravity experiments requires ionization inside the void, although the heating of the electrons is highest in the dust clouds surrounding the void. Chapter 6 shows that the dust causes a large gradient in the electron temperature, which results in a time averaged electron energy density flux in the electric field. This transports the heat from the clouds into the void, where it causes the ionization required for the formation of the void.

In chapter 7 we use an one-dimensional Particle In Cell plus Monte Carlo model for similar discharges as modelled with the fluid code. This model solves the equation of motion for many super particles representing real plasma particles and solves the elastic and inelastic collisions of these super particles with both the background gas and the dust clouds in the discharge. We included the effect of a flux of ultraviolet radiation on the dust charge, by adding the effect of photo-detachment. With this model we showed that UV light can be effectively used as an external tool to manipulate the dust charge, and through this the dust coagulation and transport. We also investigated the response of the dusty plasma on a short pulse of UV light and concluded that the response of the dust charge is much faster than the response of the surrounding plasma. The latter involves the plasma loss timescale, whereas the former involves the OML charging time, which is much shorter.

In the near future, many new plasma enhanced processes will emerge, for instance the formation of nanodots, or the manufacturing of carbon-nanotubes. Modelling effort will be required to optimize these processes, including the complex chemistry of these discharges. An one-dimensional version of our fluid model was coupled to an aerosol model to simulate the formation of small particles through chemical pathways. An extension to the current two-dimensional model would provide a powerful and accurate predictive tool regarding the mentioned plasma enhanced processes, especially if the charge dependency of particle formation could be studied.

The effective and safe operation of future tokamak devices will depend on an understanding of the role of dust in these devices. Modelling of dust near surfaces in strong magnetic fields and at high fluxes will be required. An extension of the aerosol-dust fluid models to include surface chemistry as pathways for dust formation would be interesting. Experimental data on the formation and the effect of dust particles in plasmas similar to the plasmas found in the divertor of, for instance, ITER would be essential. A device such as PILOT-PSI for the studies of plasma-wall interaction, operated at the FOM-Institute for Plasma Physics Rijnhuizen, which has shown to reach ITER relevant conditions, or the continuation of this device, called MAGNUM-PSI, which will have a large plasma bundle, seems to be the obvious choice.

Samenvatting

Het grootste deel van het zichtbare heelal bestaat uit plasma. Het is dan ook bijzonder dat we in ons dagelijks leven zo weinig met plasma in aanraking komen. Plasma bevindt zich in de ruimte tussen de sterren in grote wolken van gas en stof. De sterren bestaan zelf ook uit plasma en in de atmosfeer van planeten bevindt zich ook plasma, bijvoorbeeld in het poollicht en in bliksem. Maar plasma's worden ook door ons gebruikt, bijvoorbeeld tijdens de fabricage van computerchips en zonnecellen. Ook gebruiken we plasma's in het aanbrengen van beschermende lagen, bijvoorbeeld om plastics beter bestand te maken tegen krassen en voor het schoonmaken van oppervlakken, bijvoorbeeld van medische apparatuur. Maar ook spaarlampen en neonverlichting zijn voorbeelden van plasma-applicaties. En als laatste wordt plasma gebruikt in het concept van de tokamak fusiereactor, waarin plasma wordt opgesloten in een torusvormige kamer met behulp van magneten en wordt verhit totdat waterstof-isotopen samensmelten, waarbij heel veel energie vrijkomt.

Soms vormt zich stof in plasma, ofwel door chemische reacties in het plasma of op de plaatsen waar wanden met plasma in contact komen, ofwel door de fysieke ablatie van deeltjes van de muur, bijvoorbeeld in de divertor van een tokamak fusiereactor².

Het insluiten van nanokristallijne deeltjes in de lagen van polymorfe zonnecellen verhoogt de efficiëntie bij blootstelling aan zonlicht, door het vertragen van het Staebler-Wronski effect. Bij het maken van computerchips worden stofdeeltjes echter vaak aangeduid als 'killer-particles', omdat ze op de chips de structuren met afmetingen van enkele nanometers stuk maken. In fusiereactoren is hun rol niet helemaal duidelijk, maar ze zouden belangrijk kunnen zijn voor het vasthouden van tritium. En in de ruimte, vaak in aanwezigheid van magneetvelden en ultraviolet licht, spelen stofdeeltjes een grote rol bij de vorming van planeten en sterren.

In dit proefschrift presenteren we de resultaten van onderzoek naar het gedrag van en controle over stoffig plasma, vooral in de aanwezigheid van magnetische

²De divertor is als het ware de asla van een fusiereactor, waar het afval van de fusiereacties naar toe wordt geleid door de magneetvelden.

velden en ultraviolet licht. Deze resultaten werden voornamelijk behaald door het toepassen van complexe computermodellen, maar gedeeltelijk ook door experimenteel onderzoek. We gebruikten daarbij o.a. een tweedimensionaal vloeistofmodel en pasten dit toe op radiofrequente (RF) ontladingen in micro-zwaartekracht, waaraan micrometer grote stofdeeltjes zijn toegevoegd om experimenten aan stoffige plasma's te doen.

In dit model vinden we de waarden voor de plasmagrootheden gedurende tijdschalen kleiner dan de RF-tijd, door een drift-diffusie benadering voor de deeltjesfluxen en elektronenergiedichtheidsflux te gebruiken in de vergelijkingen voor de deeltjes- en elektronenergiebalans. Om deze vergelijkingen op te lossen, gebruiken we de Poissonvergelijking om het elektrisch veld te vinden. Het stoftransport lossen we op door alle krachten te vinden die werken op het stof, waaronder de elektrostatische kracht, de ionenwrijving en thermoforetische kracht. Door aan te nemen dat deze in balans zijn met de neutrale wrijving vinden we een drift-diffusie vergelijking voor het stof, waarbij de incompressibiliteit van het stof ook is meegenomen.

Om deze krachten te berekenen wordt de stoflading bepaald door de impulsmoment gelimiteerde (Eng:OML) elektronen- en ionenstroom te berekenen met de plasmagrootheden als invoergegevens. De daarbij behorende recombinatie van plasma op stof wordt als verliesterm voor deeltjes en energie in de plasmavergelijking gebruikt. Dit, en de bijdrage van de stoflading aan de Poissonvergelijking, verbindt het stof aan de plasmaberekeningen, waardoor de code consistent is. Het verschil in tijdstappen voor de plasma- en stofberekeningen wordt efficiënt opgelost.

In hoofdstuk 3 hebben we het effect van een axiaal magneetveld op het stoftransport onder microzwaartekracht bestudeerd, waarbij we ons vooral richtten op de vorming van de stofvrije 'void'. We hebben laten zien dat het ionentransport verandert door de verandering in de ambipolaire diffusie, ook als het magnetisch veld te zwak is om de ionen direct te magnetiseren. Dit veroorzaakt een verandering in de ionenwrijving, waardoor het minder tijd kost om een stofvrije void te vormen.

Aan de Universiteit van Auburn in de Verenigde Staten hebben we een experiment gerealiseerd om de reactie van een stoffig plasma op een aangebracht magnetisch veld te onderzoeken. In hoofdstuk 4 laten we zien dat zowel het plasma als het stof reageren in de $\mathbf{E} \times \mathbf{B}$ richting. De reactie van het stof bestaat uit twee delen, een eerste, snel deel en een tweede, langzaam deel.

Een hoofdrol in het stoftransport is weggelegd voor de ionenwrijving, die afhangt van de afscherming van stofdeeltjes door plasma, van ion-atoombotsingen en van de ionendriftsnelheid. We hebben de code uitgebreid met alle actuele theoriën die de ionenwrijving beschrijven. In hoofdstuk 5 laten we zien dat in microzwaartekrachtexperimenten niet-lineaire afbuiging van ionen het belangrijkste

is voor stoftransport, terwijl ion-atoombotsingen en de ionendriftsnelheid minder van belang zijn. Ion-atoombotsingen zijn echter wel belangrijk voor de stoflading.

Een belangrijk effect van het stof op plasma is dat plasma recombineert op het stof. Dit heeft bijvoorbeeld een groot effect op de verhitte elektronen in het plasma. Binnen in de void moet ionisatie zijn, terwijl de verhitte elektronen door het stof juist in de omliggende stofwolken optreedt. In hoofdstuk 6 laten we zien dat een groeiende elektrontemperatuursgradiënt ontstaat als er stof wordt toegevoegd. Deze gradiënt werkt samen met het gemiddelde elektrische veld en transporteert de warmte naar de void, waar het wordt gebruikt voor ionisatie.

In hoofdstuk 7 simuleren we vergelijkbare ontladingen met een eendimensionaal PIC/MC code, dat de bewegingsvergelijkingen oplost voor superdeeltjes. Die vertegenwoordigen vele echte plasmadeeltjes die botsen met het achtergrondgas en het stof. We hebben het effect van een flux van ultraviolet licht op de stoflading via foto-afscheiding van elektronen toegevoegd. Met dit model hebben we laten zien dat UV licht effectief gebruikt kan worden als een extern werktuig om stoflading in een plasmaontlading te manipuleren. We hebben ook gekeken naar de reactie van een stoffig plasma op een korte puls van UV-licht en lieten zien dat de reactie van de stoflading veel sneller is dan de reactie van het plasma, die afhangt van de verliestijd van plasma, vooral door diffusie.

In de nabije toekomst zullen er nieuwe plasmatechnieken verschijnen, bijvoorbeeld voor het produceren van nanodots of voor de ontwikkeling van koolstof nanobuizen. Er zullen modellen nodig zijn om deze technieken te optimaliseren, waarbij ook de complexe chemie meegenomen moet worden. Een eendimensionale versie van ons vloeistofmodel is al eens gekoppeld aan een aerosol-model voor de vorming van stofdeeltjes. Een uitbreiding naar twee dimensies zal een krachtig model vormen voor bovenstaande ontwikkelingen, vooral ook als het aerosolmodel uitgebreid zou worden om de ladingsafhankelijke coagulatie van grotere deeltjes mee te nemen in de berekeningen.

Het effectief en veilig gebruik van toekomstige tokamak fusiereactoren zal o.a. afhangen van een begrip van de rol van stof. Het modelleren van stof nabij oppervlakken in sterke magneetvelden bij hoge plasmafluxen zal daarbij nodig zijn. Een uitbreiding van het aerosol-vloeistofmodel met oppervlaktechemie lijkt een interessante optie. Experimenteel zal er ook data nodig zijn om de vorming van stof en het effect daarvan op het plasma in een divertor te bestuderen. Experimenten voor de bestudering van plasma-wand interactie lijken daarbij een voor de hand liggende keuze. Op het FOM-Instituut voor plasmafysica Rijnhuizen heeft PILOT-PSI aangetoond ITER-relevante regimes te bereiken. Zijn opvolger MAGNUM-PSI zal een bredere plasmabundel vormen. Deze experimenten zijn uitstekende kandidaten.

Curriculum Vitæ

Victor Land

I was born in Petten near the North Sea coast, on the 25th of December, 1979. At the age of five, we moved to Wijdewormer, a place close to Zaandam. In Zaandam, I went to Gymnasium 'Het Zaanlands Lyceum', where I received my Gymnasium diploma in 1998. I then studied general astrophysics at Utrecht University and obtained my Master of Science degree in general astrophysics, in 2003. My final research project was titled 'MHD Waves and Instabilities in Accretion Disks', which I performed at the FOM-Institute for Plasma Physics Rijnhuizen, in Nieuwegein, under the supervision of Professor Rony Keppens and Professor Hans Goedbloed. From 2003 to 2007, I conducted my PhD research on the topic of dusty plasmas, under the supervision of Professor Wim Goedheer, and Professor Niek Lopes Cardozo, at the same institute. This thesis is part of the completion of that research.